Aus dem Institut für medizinische Genetik und Humangenetik
der Medizinischen Fakultät Charité – Universitätsmedizin Berlin und dem Max-
Planck-Institut für molekulare Genetik

# DISSERTATION

The *Pigv*$^{341E}$ mouse model for GPI anchor deficiency displays behavioral
alterations and shows reduced synaptic transmission in the hippocampus

Zur Erlangung des akademischen Grades
Doctor of Philosophy (PhD)

vorgelegt der Medizinischen Fakultät
Charité – Universitätsmedizin Berlin

von

Enrique Miguel Rodriguez de los Santos, M.Sc.

aus Stuttgart

Datum der Promotion: 3.12.2021

# Inhaltsverzeichnis

# 1.) Abstract

Biallelic mutations in genes involved in glycosylphosphatidylinositol (GPI) anchor synthesis and maturation lead to the pathway disease GPI biosynthesis deficiency (GPIBD) causing intellectual disability and a psychomotor delay. Besides these common manifestations, human patients have a broad spectrum of features, that ranges from brachytelephalangy, autism, sleep disturbances, to micro/-and macrocephaly. The pathophysiology underlying the disease remains unclear and currently there is no mouse model available reflecting the overall condition of human patients. Consequently, studying the disease in a profound manner, in order to understand physiological, cellular, and molecular pathomechanisms, is very limited. For this purpose, we generated the first mouse model with a hypomorphic and patient-specific mutation (*Pigv* c.1022C>A; Pigv p.Ala341Glu; *Pigv*$^{341E}$) using CRISPR-Cas9, that mirrors the human phenotype in multiple ways. We performed extensive behavioral testing and observed in homozygous mutant (*Pigv*$^{341E}$) mice a clear and elaborated motor deficit, enhanced sociability, and cognitive deficits in spatial long-term memory and sleep disturbances. Furthermore, immunohistochemistry revealed reduced synaptophysin immunoreactivity in CA1 of *Pigv*$^{341E}$ mice and electrophysiological recordings showed decreased hippocampal synaptic transmission, that may impair memory formation. In single-cell RNA sequencing, *Pigv*$^{341E}$-hippocampal cells exhibited changes in gene expression, most prominently in a subtype of microglia and subicular neurons. A significant reduction in *Abl1* transcript levels in several cell clusters suggested a link to the signaling pathway of GPI-anchored ephrins. We also observed elevated levels of *Hdc* transcripts, which might affect histamine metabolism with consequences for circadian rhythm. This new mouse model will not only open the doors to further investigation into the pathophysiology of GPIBD, but will also deepen our understanding of the role of signaling pathways in brain development, that depend on GPI-anchored substrates.

## 2.) Zusammenfassung

Biallelische Mutationen in Genen, die an der Synthese und Reifung von GPI-Ankern beteiligt sind, führen zu der Erkrankung Glycosylphosphatidylinositol-Biosynthese-Defizienz (GPIBD), welche eine mentale Retardierung und psychomotorische Verzögerung verursacht. Neben diesen allgemeinen Phänotypen haben menschliche Patienten ein breites Spektrum an Merkmalen, das von Brachytelephalangie, Autismus, Schlafstörungen bis hin zu Mikro- und Makrozephalie reicht. Der Krankheit zugrunde liegende Pathomechanismus ist nach wie vor unklar und es gibt derzeit kein Mausmodell, welches den Gesamtzustand der Patienten widerspiegelt. Folglich ist es nur sehr eingeschränkt möglich, die Krankheit eingehend zu untersuchen, um physiologische, zelluläre und molekulare Pathomechanismen zu verstehen. Zu diesem Zweck haben wir mittels CRISPR-Cas9 das erste Mausmodell mit einer homozygoten hypomorphen und patientenspezifischen Mutation (*Pigv* c.1022C>A; Pigv p.Ala341Glu; *Pigv*$^{341E}$) generiert, welches die Symptome, die in Patienten beobachtet werden, adäquat widerspiegelt. Wir führten umfangreiche Verhaltenstests im Mausmodell durch und beobachteten bei den homozygoten mutierten *Pigv*$^{341E}$-Mäusen ein deutliches und ausgeprägtes motorisches Defizit, erhöhte Soziabilität und kognitive Defizite im räumlichen Langzeitgedächtnis sowie Schlafstörungen. Darüber hinaus zeigten immunhistochemische Analysen eine reduzierte Synaptophysin-Immunreaktivität in CA1 der mutierten *Pigv*$^{341E}$-Mäuse. Elektrophysiologische Experimente zeigten zudem eine verringerte synaptische Reizweiterleitung im Hippocampus, die einer beeinträchtigten Gedächtnisbildung zugrunde liegen könnte. Bei der Einzelzell-RNA-Sequenzierung beobachteten wir, dass *Pigv*$^{341E}$-Hippocampuszellen Veränderungen in der Genexpression aufweisen, und zwar am deutlichsten in einem Subtyp von Mikroglia-Zellen und subikulären Neuronen. Eine signifikante Reduktion der *Abl1*-Transkripte in mehreren Zellclustern deutete auf einen Zusammenhang mit dem Signalweg der GPI-verankerten Ephrine hin. Wir beobachteten auch eine erhöhte Transkription von *Hdc*, die den Histamin-Stoffwechsel mit Konsequenzen für den zirkadianen Rhythmus beeinflussen könnte. Dieses neue Mausmodell wird nicht nur die Türen für weitere Untersuchungen zur Pathophysiologie von GPIBDs öffnen, sondern auch unser Verständnis für GPI-Anker-assoziierte Signalwege in der Gehirnentwicklung vertiefen.

# 3.) State of the art - research

The GPI-anchor is a complex glycolipid, that is crucial for the tethering of GPI linked proteins and consists of multiple biochemical units, that build up the core structure of GPI linked proteins: Protein-EtNP-Man-3-Man2-Man-1-GlcN-PI (Fig. 1B) (Homans *et al*. 1988). So far, 27 genes have been identified that are involved in the synthesis and maturation of the GPI-anchor. The GPI-anchor pathway is structured in several steps [2]: 1.) Early GPI-anchor synthesis; 2.) Late GPI-anchor synthesis; 3.) GPI transamidase, that catalyzes the attachment of the GPI-anchor substrate to its respective GPI-anchor; 4.) GPI-anchor maturation, in which fatty acids of the GPI-anchor is remodeled for proper association with lipid rafts (Fig. 1A, C).
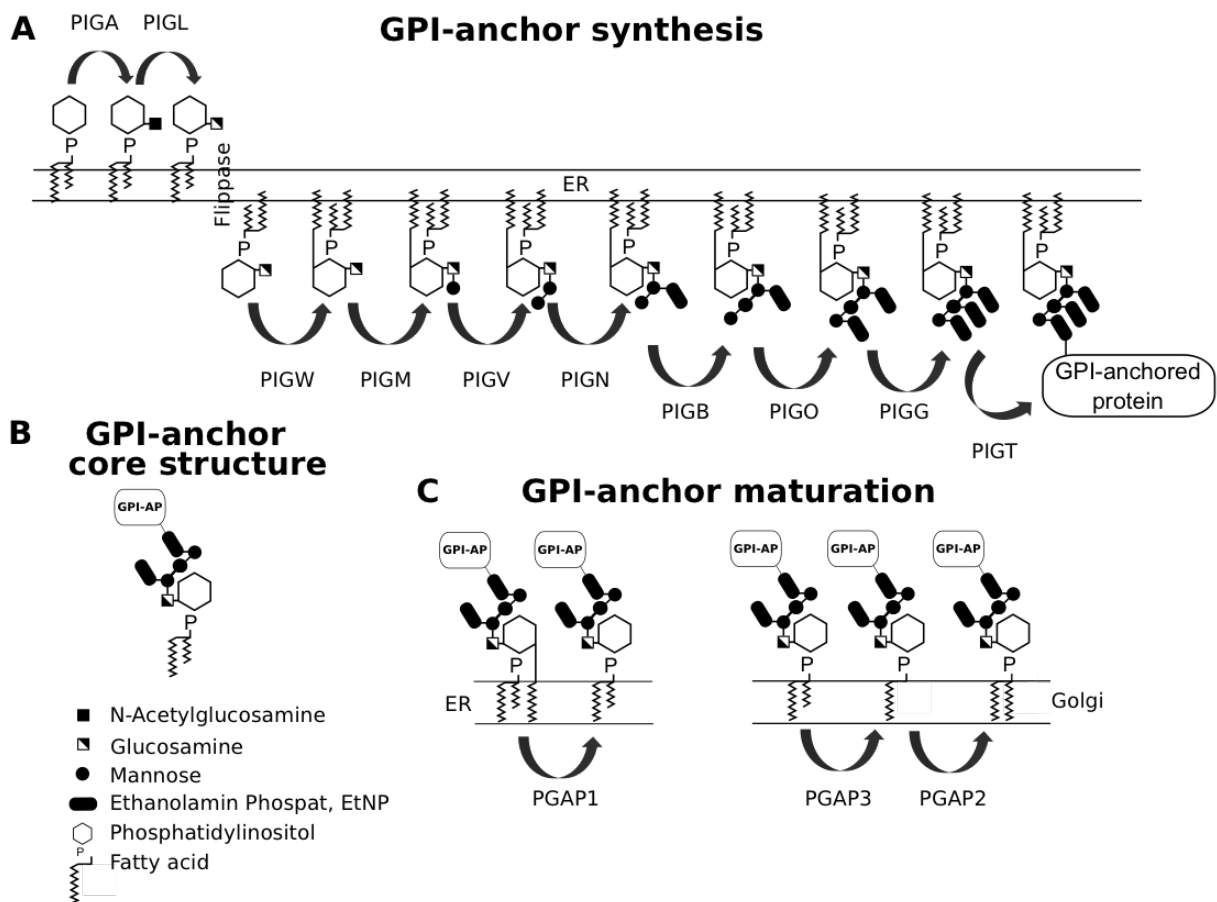


**Figure 1. GPI-anchor synthesis and maturation (own representation).** (A) Overview about the biochemical steps for the synthesis of the GPI-anchor taking place in the endoplasmic reticulum (ER). The GPI-anchor synthesis of the GPI-anchor is subdivided in early GPI-anchor synthesis (PIGA-PIGW), late GPI-anchor synthesis (PIGM-PIGG) and GPI transamidase (PIGT) catalyzes the transfer of the GPI-anchor to the protein. (B) Overview about the biochemical subunits, which build up the core structure of GPI-anchored proteins (GPI-AP) (top graph). Nomenclature about the biochemical subunits (bottom graph). (C) Overview about the GPI-anchor maturation that takes place in the ER and in the Golgi. Genes are depicted that have been linked to pathogenic mutations leading to IGD. PIGA, N-acetylglucosaminyltransferase subunit. PIGW, inositol acyltransferase. PIGM, mannosyltransferase 1. PIGV, mannosyltransferase 2. PIGN, ethanolamine phosphate transferase 1. PIGB, mannosyltransferase 3. PIGO, ethanolamine phosphate transferase 3. PIGG, ethanolamine phosphate transferase 2. PIGT, GPI transamidase. PGAP1, Post-GPI attachment to proteins inositol deacylase 1. PGAP3, post-GPI attachment to proteins phospholipase 3. PGAP2, post-GPI attachment to proteins 2.
.

GPI-anchor synthesis including step 1-3 takes place in the endoplasmic reticulum, whereas GPI-anchor maturation (step 4) occurs in the Golgi. Murakami *et al.* defined early and late GPI-anchor synthesis by showing *in-vitro* that genes involved in the early step showed normal GPI linked Alkaline Phosphatase (AP) activity [3]. In contrast, genes involved in late GPI-anchor synthesis (after attachment of the first mannose) exhibited high AP activity. The reason for this observation is that if the synthesis is impaired at an early step, GPI transamidase is not activated and subsequently the hydrophobic signal peptide of GPI-anchor substrates is not cleaved. As a consequence, GPI-anchor substrates (for instance, AP) are not attached to the GPI-anchor and are further internalized in the ER for degradation. In contrast, a defect at a later stage results in attachment of the GPI-anchor substrate by GPI-anchor transamidase, however, due to a not fully synthesized GPI-anchor the GPI-anchor substrate is released in the extracellular matrix. Therefore, a defective GPI-anchor synthesis at a later stage, including also step 4 (remodeling of the fatty acids), results in hyperphosphatasia [4–7].

GPI-linked proteins play a crucial role in cell-cell adhesion, signal transduction and specifically synapse formation and plasticity, and regulation of the complement system comprising approximately 0.5% of all eukaryotic cell surface proteins [8–10]. Therefore, it is not surprising that an inherited GPIBD (IGD) results in a broad spectrum of different features. Therefore, physicians categorize patients in two subgroups based on alkaline phosphatase (AP) levels in the blood: First, Hyperphosphatasia and mental retardation syndrome (HPMRS) including patients affected in *PGAP2*, *PGAP3*, *PIGV*, *PIGO*, *PIGW*, which have high AP level [5,6,11–13]; second, multiple congenital anomalies hypotonia seizures (MCAHS) patients with mutations in *PIGA*, *PIGN*, and *PIGT,* in which hyperphosphatasia is not described as a key clinical feature [14–16]. However, previous studies suggested that diagnosing patients should be rather based on a gene-centered approach, since there is a rising evidence of exception for AP levels in HPMRS and MCAHS [17]. Despite the high variability of symptoms in IGD, human patients have common manifestations that are displayed by intellectual disability, psychomotor delay and epilepsia. A further type of GPIBD is paroxysmal nocturnal hemoglobinuria (PNH), that was the first GPIBD to be found in human patients and that is characterized by blood anemia [18]. In contrast to IGD, PNH is acquired due to somatic mutations in *PIGA, PIGT* and *PIGB,* respectively*,* in hematopoietic stem cells and the prevalence is 10-fold lower [19,20].

Most of the mutations in IGD are found in *PIGV* and the most frequent mutation in European patients is the *PIGV* c.1022C>A mutation. *PIGV* encodes for a mannosyltransferase II that is essential for the attachment of the second mannose to the GPI-anchor (Fig.1A). *PGAP3*, which encodes for the post-GPI attachment to proteins phospholipase 3 and involved in GPI-

anchor maturation (Fig. 1C), is the second most affected gene with the mutation c.320 C>T in patients that we diagnosed with IGD. Fibroblasts of different patients with either the homozygous mutation c.1022 C>A in *PIGV* or c.320 C>T in a compound heterozygous state in *PGAP3* showed in flow cytometry a decreased expression of GPI linked proteins [11,21].

The neurological pathophysiology of IGD is largely unknown and also difficult to investigate in humans. Considering that rodents have been rigorously used to model a broad spectrum of neurodevelopmental diseases, mice represent an interesting organism to study the pathophysiology of IGD. Indeed, GPI-anchor deficiency have been studied mainly in chimeric and conditional knockout mouse models [22–26]. However, a complete loss of GPI-anchor biosynthesis is embryonically lethal in most of the cases [27]. Furthermore, mouse models that survived embryonic stages, died at an early stage after birth underpinning the importance of GPI-linked proteins for survival [24,28]. A Nestin-Cre x Piga$^{flox}$ mouse model, where *Piga* is disrupted mainly in astrocytes, oligodendrocytes and neurons, showed an ataxia-like behavior, cerebellar hypoplasia, defective myelination causing a delay in white matter development, and impaired dendritic arborization in Purkinje cells [24]. Furthermore, in the same mouse model bulk RNA sequencing showed a miss-regulation of circadian clock genes. Intriguingly, also human patients with *PGAP3*-deficiency, have been described to suffer from ataxia and sleep disturbances [21].

In addition, further mouse models for GPI-anchor deficiency have been investigated, that were identified in mutation screens. These animals were viable, since the mutations were hypomorphic or the mutant isoforms were expressed in a tissue-specific manner [29,30]. The CIpex mutant, carrying a missense mutation in *Pgap2* (c.A1G, p.M1V), was mainly affected in neural crest cells and the cranial neuroepithilium leading to the craniofacial phenotype [29]. In agreement with these findings, McKean *et al.* observed a craniofacial phenotype (holoprosencephaly-like phenotype) in two mouse models with a frame-shift mutation in *Pign* and an in-frame deletion in *Pgap1* underlining the crucial role of GPI-linked proteins in craniofacial development [30]. Interestingly, also human patients display facial abnormalities, however, much milder than shown in mice, probably due to a different amino acid substitution or the isoforms p.(M52R) and p.(M58R) do not exist in mice. In particular, patients with IGD have a characteristic facial gestalt including a broad nasal bridge, wide set eyes and a tented upper lip. The characteristic facial gestalt has been used previously to infer the affected GPI-anchor gene by gestalt matching [17].

So far, suitable mouse models reflecting the overall condition in human patients including cognitive, motor and social alterations are missing. Mostly because the above-described mouse

models had a too severe phenotype and were not able to survive until adulthood. For this purpose, we generated via CRISPR-Cas9 the first mouse model with the hypomorphic mutation c.1022C>A in *PIGV* that is the most frequent mutation in European patients and that is also conserved in mice (Pigv p.Ala341Glu, *Pigv*[341E]) [31]. Due to the hypomorphic mutation in *Pigv*, that is leading to a reduced function of the enzyme and not to a complete knockout, the *Pigv*[341E] mouse model had a normal life span that made it possible to study profoundly the behavioral phenotype. Furthermore, we were able to accomplish cellular and molecular assays in order to study the pathomechanism in GPI-anchor deficiency.

# 4.) Methodology

In the following chapter, the principles of the methods are described. Further details about materials and applied protocols are also listed in the respective section of the attached publication "A CRISPR-Cas9–engineered mouse model for GPI-anchor deficiency mirrors human phenotypes and exhibits hippocampal synaptic dysfunctions" [31]. All animals were handled according to government regulations and approved by local authorities under the licence G0365/17, G0346/13, G0176/19, G0247/13 and G0243/18.

## 4.1.) CRISPR-Cas9 gene editing in mouse embryonic stem

CRISPR-Cas9, that consists of the nuclease Cas9 and a single guide RNA (sgRNA), is a powerful tool for gene editing that has proven its application in a broad range of different fields [32]. The technique induces double strand breaks (DSB) via its nuclease Cas9 at a side that is complementary to the sgRNA [33]. Little specificity to off-targets and high efficiency to on-targets of sgRNAs were determined by the platform http://crispor.tefor.net/. DSBs are either repaired via the homology-directed repair (HDR) or via the non-homologous end joining (NHEJ) pathway [34]. The HDR uses a DNA template (targeting vector, oligonucleotides) in order to correct the DSB in a precise manner, whereas the NHEJ sticks the DNA ends together by inserting or deleting nucleotides, thereby causing insertion and deletion (indel) mutations. It has been shown, that NHEJ occurs more often than HDR at CRISPR-Cas9-induced DSBs [35], which is inconvenient for precise gene-editing. Since we were interested in knock-ins of pathogenic mutations at a specific site, we used a strategy, that was already proven to increase HDR events at CRISPR-Cas9-induced DSBs [36,37]: We designed single strand oligo-deoxynucleotides (ssODN) including the pathogenic mutation (*Pigv*[341E] or *Pgap3*[107L]) with

asymmetrical homology arms and modified phosphorothioate bonds according to Richardson and Renaud, *et al.*. PX459 vector from Addgene, encoding the sgRNA PIGV#1 and PGAP3#1, respectively, and Cas9 were co-transfected with ssODNs in mES cells via lipofection as previously described [38]. Positive mES cell clones with the mutation *Pigv* c.1022C>A (Pigv p.Ala341Glu, *Pigv*[341E]) were selected by the genotyping approach described in de los Santos *et al.* (Fig. S1A, SI *Appendix*) and used for tetraploid aggregation in order generate and establish the mouse line *Pigv*[341E] [31].

## 4.2.) Tetraploid aggregation

Through tetraploid aggregation we were able to generate transgenic chimeras with a chimerism of more than 95%. Prior to morula-aggregation, mES cells in embryos (two-cell stage), that were isolated from pregnant donors, were fused to tetraploid cells by electroporation. Subsequently, diploid CRISPR-Cas9-modified mES cells were then aggregated with wild-type tetraploid cells in the morula, that formed exclusively the extra-embryonic tissue. In contrast, diploid transgenic mES cells gave rise to the embryo.

## 4.3.) Flow cytometry of CRISPR-Cas9-modified mES cells and mouse embryonic fibroblasts (MEFs)

We studied GPI-linked protein expression of CRISPR-Cas9-modified mES cell lines *Pigv*[341E] and *Pgap3*[107L] and MEFs from E13,5 *Pigv*[341E]-embryos in flow cytometry analysis. For this purpose, mES and MEF cell lines were stained with fluor-proaerolysin (FLAER) fused to the Alexa488 and with Anti-CD90 fused to pycoerythrin (only in mES cells). FLAER is a prototoxin, deriving from bacteria, that is able to recognize the GPI-anchor in the plasma membrane [39]. Moreover, Anti-CD90 antibody has been used in previous studies to analyze GPI-linked CD90 surface expression in GPI-anchor-defective mES cells [40]. Fluorescence-labeled GPI-linked proteins on the cell surface were then detected in the flow cytometer and quantified by the software.

## 4.4.) Behavioral testing

In order to study the behavioral phenotype underlying GPI-anchor deficiency in mice, we applied several behavioral tests to assess motor-, social-, cognitive-, and species-specific abilities in the $Pigv^{341E}$ mouse model.

We evaluated hindlimb clasping in $Pigv^{341E}$ mice that is a characteristic phenotype for neurological deficits in rodents [24,41,42]. Spontaneous behaviors of $Pigv^{341E}$ mice while living undisturbed in their home cage (singly housed or group housed) were analyzed in the home cage scan (HCS) (occurrences, duration of 19 different behaviors) and social activity monitor (SAM) (distance travelled per phase, day, hour, total distance travelled in the home cage).

We carried out the rotarod performance, beam walking and rope grip test to assess motor coordination and balancing abilities in $Pigv^{341E}$ mice. Furthermore, we evaluated the walking pattern in the footprint test and measured the grip strength in $Pigv^{341E}$ mice through the grip strength meter. We analyzed social behavior in $Pigv^{341E}$ mice by the three-chamber test (sociability, social recognition) and in the social proximity test we studied social interaction of $Pigv^{341E}$ mice in more detail. We evaluated spatial learning and memory (short- and long-term) in $Pigv^{341E}$ mice by the Barnes maze test and working short-term memory by the y-maze test. Furthermore, we characterized species-specific behaviors in $Pigv^{341E}$ mice by the nest construction and marble burying test. The open field, dark-light box and the elevated-plus maze test assessed affective-related behavior in $Pigv^{341E}$ mice.

## 4.5.) Histology and immunohistochemistry

The animals were deeply anesthetized and subsequently transcardially perfused with DPBS and paraformaldehyde (PFA). Brains were removed and prepared for paraffin infiltration by immerse fixation in PFA, and dehydration in ethanol. Afterwards, paraffin-infiltrated brains were embedded in paraffin and coronal sections were made with a microtome. Subsequently, sections were deparaffinized and rehydrated for Nissl staining and for synaptophysin immunofluorescence-staining.

For Nissl staining, sections were incubated in cresyl violet buffered in acetate buffer, that stains all neurons in a blue color. For morphological analysis of the hippocampus, Nissl-stained sections were evaluated under the microscope. For synaptophysin immunofluorescence-staining, a specific antibody was used, that recognizes synaptophysin and that is conjugated to Alexa488. Furthermore, 4,6-diamidino-2- phenylindole (DAPI) was utilized for visualization of nuclei.

Images were taken from the *Cornu Ammonis* 1 – *Stratum Radiatum* (CA1–SR), *Cornu Ammonis* 3 – *Stratum Radiatum* (CA3–SR) and *Cornu Ammonis* 1 – molecular layer of *dentate gyrus* (CA1–ML) using a confocal microscope. Synaptophysin immunoreactivity was measured with the software.

## 4.6.) Electrophysiology recordings

Acute slice preparations were performed as previously described [43]. Electrodes were placed in CA3-SR for stimulation of Schaffer collaterals and recording electrodes were placed in CA1-SR. To analyze the input–output relationship, stimulation intensities were adjusted to different fiber volley amplitudes and correlated with the corresponding field excitatory post-synaptic potential (fEPSP) amplitudes. Paired pulse ratios (PPRs) were determined by dividing the amplitude of the second fEPSP by the amplitude of the first. Four high-frequency trains were applied every 10 sec, and the amplitude of the following fEPSP was normalized to the baseline defining the post-tetanic potentiation (PTP).

## 4.7.) Pentylenetetrazol (PTZ) kindling model

Since most of the patients with IGD develop epileptic seizures and we did not observe any spontaneous seizure behavior in the mouse model, we analyzed differences in seizure threshold between mutant mice and wild-type littermates in the PTZ kindling model. Convulsive seizures were induced by repetitive intraperitoneal injections of PTZ every 10 min as described before [44].

## 4.8.) Single-cell RNA sequencing, preprocessing, and analysis

The isolation of hippocampal cells was performed at 4°C with an optimized protocol described in [45]. Afterwards, single-cell suspension was further processed for single-cell RNA sequencing-library preparation following the manufacturer's instructions. Afterwards, libraries were sequenced, and data analysis including alignment to the reference genome (GRCm38.96) and quantification of single-cell gene expression was carried out. Further data processing comprised filtering, normalization and principal component analysis. The first 11 principal components were selected for dimensionality reduction based on the amount of captured variance. These components were used as input for clustering of cells, as well as for two-

dimensional visualization with uniform manifold approximation and projection (UMAP). We defined cellular subgroups based on differentially expressed genes between the clusters. Candidate genes were confirmed using the adult mouse brain atlas (http://dropviz.org/) and *in-situ* hybridization data from the Allen brain atlas (https://mouse.brain-map.org/search/index). We analyzed differentially expressed genes between genotypes and between cellular subgroups per genotype. Differentially expressed genes were then further evaluated by gene ontology (GO) analysis.

## 5.) Essential results

To date, mouse models demonstrating motor, social and cognitive alterations at the same time and thereby mirroring the human pathology, have not been available. We present here the first mouse model with a comparable phenotype to human patients: We were able to show a clear and elaborated motor phenotype including deficits in motor coordination, alteration in walking pattern and a reduced grip strength; in the Barnes maze test, $Pigv^{341E}$ mice displayed cognitive deficits in spatial long-term memory; we observed in $Pigv^{341E}$ mice an enhanced social approach behavior that was displayed in the three-chamber test by spending more time with a stranger mice than in the vicinity of an empty cage. The social approach behavior was confirmed in the social proximity test, where we observed an elevated number of nose-to-anogenital contact and reduced "rear up" behavior in $Pigv^{341E}$ mice. In contrast to the normal sleeping periods in rodents, $Pigv^{341E}$ mice displayed higher activity levels during the light cycle in the SAM and had a reduced duration of sleeping behavior in the HCS. These results suggested a disturbed sleep in $Pigv^{341E}$ mice that was also supported by the fact, that some patients with *PGAP3* deficiency suffer from sleep disturbances [21]. We also observed alterations in species-specific behaviors in $Pigv^{341E}$ mice comprising reduced marble burying and nest construction behavior. Alterations in marble burying and nest construction has been observed in rodents with malfunctions in the hippocampus [46]. Hippocampal impairments could also be responsible for deficits in spatial long-term memory in $Pigv^{341E}$ mice. Therefore, we had a closer look into hippocampal synaptic properties and performed electrophysiology recordings.

$Pigv^{341E}$ mice showed a reduced synaptic transmission in CA1 that was displayed by a lower input-output curve. Furthermore, post-tetanic potentiation (PTP) and pre-pulse ratio (PPR) was elevated in $Pigv^{341E}$ mice indicating a lower synaptic release probability. Likewise, we observed a reduced synaptophysin immunoreactivity, a pre-synaptic vesicular marker, in CA1 of $Pigv^{341E}$ mice. We hypothesized a reduced pool of readily releasable vesicles leading to elevated

PTP and PPR in the pre-synapse and a lower input-output curve in the post-synapse. These critical results proved that GPI-anchor deficiency is a synaptopathy.

Considering the synaptic defect observed in CA1 in $Pigv^{341E}$ mice and that 70% of patients with IGD develop epileptic seizures, we examined the susceptibility of $Pigv^{341E}$ mice for pentylenetetrazole (PTZ)-induced seizures. $Pigv^{341E}$ mice exhibited a lower seizure threshold that was displayed by a reduced latency to first seizure than wild-type mice. Moreover, four wild-type animals did not develop any seizures after 10 injections of PTZ confirming the higher susceptibility for PTZ-induced seizures in $Pigv^{341E}$ mice. Furthermore, $Pigv^{341E}$ mice exhibited more severe seizures than wild-type mice.

Due to deficits in memory formation and alterations in species-specific and hippocampus-dependent behaviors, we investigated the pathophysiological role of the hippocampus in more detail by single-cell RNA sequencing. In total, we identified 17 different cellular subgroups in the hippocampus of both genotypes. However, the distribution of cells within the cellular subgroups differed between genotypes. While the fractions of granule cells, oligodendrocytes, and a microglia subpopulation (microglia 3) were reduced in pooled samples from $Pigv^{341E}$ mice, the proportions of subicular neurons (neurons subiculum 1), GABAergic (inhibitory) interneurons, and fibroblast-like cells were higher than in the pooled wild-type samples. Moreover, in terms of differentially expressed genes, microglia 3, subicular neurons 1 and pyramidal neurons CA3 were the most affected cellular subgroups in hippocampus of $Pigv^{341E}$ mice. Remarkably, Microglia 3 cells displayed a high proportion of down-regulated genes in comparison to up-regulated genes (306 versus 20 genes). In gene ontology (GO) analysis, we observed down-regulated genes that were associated with the GO terms "protein localization to cell periphery", "small GTPase mediated signal", "regulation of microtubule polymerization or de-polymerization". Single-cell RNA sequencing suggested also an important role for subicular neurons in GPI-anchor deficiency. Since up-regulated genes were associated with the GO term "synapse organization", we hypothesized a synaptic defect as proven in CA1 of $Pigv^{341E}$ mice. Furthermore, single-cell RNA sequencing showed a robust down-regulation of *Abl1* transcript levels in $Pigv^{341E}$ mice, not only within each cellular subgroup, but also across all cellular subgroups. Abl1 is a non-receptor tyrosin kinase that interacts with several GPI-anchored EphrinA receptors and is therefore involved in transduction of the Ephrin signaling pathway [47]. Besides *Abl1*, also *Hdc* was strongly misregulated both in all cellular subgroups and within each cellular subgroup in $Pigv^{341E}$ mice, however, with an increased expression. Hdc is an enzyme (histidine carboxylase) that is involved in the synthesis of the neurotransmitter histamine.

In conclusion, we here present the first viable mouse model for GPI-anchor deficiency that not only mirrors the human phenotype, but also shows novel neurological insights important for the further understanding of the pathomechanism in GPI-anchor deficiency. Mirroring the human phenotype, the $Pigv^{341E}$ mouse model could also serve in the future for the investigation of therapeutic approaches.

# 6.) Further scientific question

We observed in $Pigv^{341E}$ mice an enhanced social approach behavior, which has not been studied in human patients in detail. However, physicians and parents of the patients already stated the observation that patients with $PIGV$ deficiency are keen to interact socially. The positive social abilities in patients with $PIGV$ deficiency is particularly remarkable, since patients also display severe speech impairment [48]. Therefore, considering the results in $Pigv^{341E}$ mice, we suggest including sociability as a feature for the diagnosis of patients with $PIGV$ deficiency. Whether also other IGDs exhibit positive social abilities, should be analyzed in future studies.

Sleep disturbances have been reported in IGD patients with $PGAP3$ deficiency [21]. Interestingly, we observed in $Pigv^{341E}$ mice shorter sleeping periods and higher activity during the light cycle that supposed a disturbed sleep, too. However, sleep disturbances have not been described in patients with $PIGV$ deficiency. Therefore, a careful analysis of their sleep pattern seems to be indicative.

In electrophysiology recording, $Pigv^{341E}$ mice displayed a reduced synaptic transmission in CA1. Increased PPR, PTP and reduced synaptophysin immunoreactivity in $Pigv^{341E}$ mice suggested a reduced pool of readily releasable vesicles in the pre-synapse. In order to confirm this hypothesis, we want to quantify the number of vesicles in the pre-synapse of CA1 by electron microscopy,

$Pigv^{341E}$ Microglia 3 showed the highest number of differentially expressed genes in single-cell RNA sequencing. GO analysis revealed an enrichment of down-regulated genes that were associated to the GO terms "protein localization to cell periphery", "small GTPase mediated signal", "regulation of microtubule polymerization or de-polymerization". Hence, we hypothesized that a GPI-anchor defect leads to down-regulation of small GTPase-mediated pathways, which has further consequences for cytoskeleton organization in this microglia subtype. In this regard, GPI-anchored EphrinA proteins could play an important role, as EphrinA1 regulates small GTPase (Rho)-dependent cytoskeleton rearrangement through Src/focal adhesion kinases [49]. Intriguingly, down-regulated genes in microglia 3 cells were

also associated with the GO term "regulation of focal adhesion assembly". Cytoskeleton rearrangement plays a crucial role in migration and phagocytosis. However, a functional assay evaluating migratory and phagocytic capacities of $Pigv^{341E}$ microglia has not been performed in this study and is advisable for future research.

In terms of differentially expressed genes, subicular neurons showed also a strong defect in $Pigv^{341E}$ mice. The subiculum is important for memory retrieval and is linked through microcircuits with the CA1 [50]. Therefore, a synaptic defect in the subiculum could also be responsible for the defect in spatial long-term memory that is observed in $Pigv^{341E}$ mice. Lederberger, *et al.* described two distinct circuits for memory acquisition and retrieval: memory acquisition involves the CA1 and medial-entorhinal-cortex, whereas memory retrieval involves the CA1, the medial-entorhinal-cortex, and the subiculum. Since it is unknown which stage of memory is affected in $Pigv^{341E}$ mice, future studies should seek to determine whether memory acquisition, memory retrieval, or both conditions are affected in $Pigv^{341E}$ mice.

GPI-anchored EphrinA ligands bind EphrinA receptors leading to clustering and phosphorylation of EphA receptors [51]. Phosphorylated EphrinA receptors activate then transducers as for instance the non-receptor tyrosin kinase Abl1 [47]. *Abl1*, which is known to interact on protein level with several EphrinA receptors, was observed to be strongly down regulated in $Pigv^{341E}$ mice. Thus, we suggested a pivotal role of the Ephrin signaling pathway in GPI-anchor deficiency: Defective GPI-anchoring of EphrinA reduces hippocampal EphrinA receptor and Abl1 activity, which has further on consequences in cellular transduction of the ephrin signaling pathway. Likewise EphrinA receptors, also Abl1 is activated or inactivated depending on its phosphorylation state [52]. Therefore, it is crucial to investigate whether the down regulation of *Abl1* in $Pigv^{341E}$ mice, as observed in single-cell RNA sequencing, implicates alterations on the phosphorylation state of Abl1 in GPI-anchor deficiency.

Also *Hdc* was shown to be robustly down-regulated in $Pigv^{341E}$ mice. It encodes for the histidine decarboxylase catalyzing the biochemical reaction that transform histidine to the important neurotransmitter histamine. The involvement of histamine in the circadian rhythm has been shown previously [53,54]: In rodents, histamine levels are elevated during the dark phase to induce wakefulness and are reduced during the light phase to induce sleep. Interestingly, $Pigv^{341E}$ mice showed higher activity levels and shorter durations in sleep during the light cycle during home-cage activity monitoring (group-housed) and the HCS (individually housed). We therefore hypothesize that higher *Hdc* expression leading to elevated histamine levels could be responsible for the imbalance in the sleep and wake rhythm in $Pigv^{341E}$ mice. However, whether histamine

levels are higher in $Pigv^{341E}$ mice remained unknown and should be investigated in further studies.

# 7.) References

1. Homans , S. W. , M. A. Ferguson , R. A. Dwek , T. W. Rademacher , R. Anand and AFW. Complete structure of the gly-cosyl phosphatidylinositol membrane anchor of rat brain Thy-1 glycoprotein. Nature. 1988;333:269 – 272.

2. Kinoshita T, Fujita M, Maeda Y. Biosynthesis, remodelling and functions of mammalian GPI-anchored proteins: Recent progress. J Biochem. 2008;144(3):287–94.

3. Murakami Y, Kanzawa N, Saito K, Krawitz PM, Mundlos S, Robinson PN, Karadimitris A, Maeda Y, Kinoshita T. Mechanism for release of alkaline phosphatase caused by glycosylphosphatidylinositol deficiency in patients with hyperphosphatasia mental retardation syndrome. J Biol Chem. 2012 Feb;287(9):6318–25.

4. Krawitz PM, Schweiger MR, Rödelsperger C, Marcelis C, Kölsch U, Meisel C, Stephani F, Kinoshita T, Murakami Y, Bauer S, Isau M, Fischer A, Dahl A, Kerick M, Hecht J, Köhler S, Jäger M, Grünhagen J, De Condor BJ, Doelken S, Brunner HG, Meinecke P, Passarge E, Thompson MD, Cole DE, Horn D, Roscioli T, Mundlos S, Robinson PN. Identity-by-descent filtering of exome sequence data identifies PIGV mutations in hyperphosphatasia mental retardation syndrome. Nat Genet. 2010;42(10):827–9.

5. Krawitz PM, Murakami Y, Hecht J, Krüger U, Holder SE, Mortier GR, Delle Chiaie B, De Baere E, Thompson MD, Roscioli T, Kielbasa S, Kinoshita T, Mundlos S, Robinson PN, Horn D. Mutations in PIGO, a member of the GPI-anchor-synthesis pathway, cause hyperphosphatasia with mental retardation. Am J Hum Genet. 2012;91(1):146–51.

6. Howard MF, Murakami Y, Pagnamenta AT, Daumer-Haas C, Fischer B, Hecht J, Keays DA, Knight SJL, Kölsch U, Krüger U, Leiz S, Maeda Y, Mitchell D, Mundlos S, Phillips JA, Robinson PN, Kini U, Taylor JC, Horn D, Kinoshita T, Krawitz PM. Mutations in PGAP3 impair GPI-anchor maturation, causing a subtype of hyperphosphatasia with mental retardation. Am J Hum Genet. 2014;94(2):278–87.

7. Hansen L, Tawamie H, Murakami Y, Mang Y, Ur Rehman S, Buchert R, Schaffer S, Muhammad S, Bak M, Nöthen MM, Bennett EP, Maeda Y, Aigner M, Reis A, Kinoshita T, Tommerup N, Baig SM, Abou Jamra R. Hypomorphic mutations in PGAP2, encoding a GPI-anchor-remodeling protein, cause autosomal-recessive intellectual disability. Am J Hum Genet. 2013;92(4):575–83.

8.  Um JW, Ko J. Neural Glycosylphosphatidylinositol-Anchored Proteins in Synaptic Specification. Trends Cell Biol [Internet]. 2017;27(12):931–45. Available from: http://dx.doi.org/10.1016/j.tcb.2017.06.007

9.  Paulick MG, Bertozzi CR. The glycosylphosphatidylinositol anchor: A complex membrane-anchoring structure for proteins. Biochemistry. 2008;47(27):6991–7000.

10. Eisenhaber B, Bork P, Eisenhaber F. Post-translational GPI lipid anchor modification of proteins in kingdoms of life: Analysis of protein sequence data from complete genomes. Protein Eng. 2001;14(1):17–25.

11. Krawitz PM, Schweiger MR, Rödelsperger C, Marcelis C, Kölsch U, Meisel C, Stephani F, Kinoshita T, Murakami Y, Bauer S, Isau M, Fischer A, Dahl A, Kerick M, Hecht J, Köhler S, Jäger M, Grünhagen J, de Condor BJ, Doelken S, Brunner HG, Meinecke P, Passarge E, Thompson MD, Cole DE, Horn D, Roscioli T, Mundlos S, Robinson PN. Identity-by-descent filtering of exome sequence data identifies PIGV mutations in hyperphosphatasia mental retardation syndrome. Nat Genet [Internet]. 2010 Oct;42(10):827–9. Available from: http://dx.doi.org/10.1038/ng.653

12. Chiyonobu T, Inoue N, Morimoto M, Kinoshita T, Murakami Y. Glycosylphosphatidylinositol (GPI) anchor deficiency caused by mutations in PIGW is associated with West syndrome and hyperphosphatasia with mental retardation syndrome. J Med Genet. 2014;51(3):203–7.

13. Ilkovski B, Pagnamenta AT, O'Grady GL, Kinoshita T, Howard MF, Lek M, Thomas B, Turner A, Christodoulou J, Sillence D, Knight SJL, Popitsch N, Keays DA, Anzilotti C, Goriely A, Waddel LB, Brilot F, North KN, Kanzawa N, Macarthur DG, Taylor JC, Kini U, Murakami Y, Clarke NF. Mutations in PIGY: Expanding the phenotype of inherited glycosylphosphatidylinositol deficiencies. Hum Mol Genet. 2015;24(21):6146–59.

14. Johnston JJ, Gropman AL, Sapp JC, Teer JK, Martin JM, Liu CF, Yuan X, Ye Z, Cheng L, Brodsky RA, Biesecker LG. The phenotype of a germline mutation in PIGA: The gene somatically mutated in paroxysmal nocturnal hemoglobinuria. Am J Hum Genet [Internet]. 2012;90(2):295–300. Available from: http://dx.doi.org/10.1016/j.ajhg.2011.11.031

15. Khayat M, Tilghman JM, Chervinsky I, Zalman L, Chakravarti A, Shalev SA. A PIGN mutation responsible for multiple congenital anomalies-hypotonia-seizures syndrome 1 (MCAHS1) in an Israeli-Arab family. Am J Med Genet Part A. 2016;170(1):176–82.

16. Yang L, Peng J, Yin XM, Pang N, Chen C, Wu TH, Zou XM, Yin F. Homozygous PIGT mutation lead to multiple congenital anomalies-hypotonia seizures syndrome 3. Front Genet. 2018;9(MAY).

17. Knaus A, Pantel JT, Pendziwiat M, Hajjir N, Zhao M, Hsieh TC, Schubach M, Gurovich Y, Fleischer N, Jäger M, Köhler S, Muhle H, Korff C, Møller RS, Bayat A, Calvas P, Chassaing N, Warren H, Skinner S, Louie R, Evers C, Bohn M, Christen HJ, van den Born M, Oberssztyn E, Charzewska A, Endziniene M, Kortüm F, Brown N, Robinson PN, Schelhaas HJ, Weber Y, Helbig I, Mundlos S, Horn D, Krawitz PM. Characterization of glycosylphosphatidylinositol biosynthesis defects by clinical features, flow cytometry, and automated image analysis. Genome Med. 2018;10(1):1–13.

18. Takeda J, Miyata T, Kawagoe K, Iida Y, Endo Y, Fujita T, Takahashi M, Kitani T, Kinoshita T. Deficiency of the GPI anchor caused by a somatic mutation of the PIG-A gene in paroxysmal nocturnal hemoglobinuria. Cell. 1993;73(4):703–11.

19. Krawitz PM, Höchsmann B, Murakami Y, Teubner B, Krüger U, Klopocki E, Neitzel H, Hoellein A, Schneider C, Parkhomchuk D, Hecht J, Robinson PN, Mundlos S, Kinoshita T, Schrezenmeier H. A case of paroxysmal nocturnal hemoglobinuria caused by a germline mutation and a somatic mutation in PIGT. Blood. 2013;122(7):1312–5.

20. Langemeijer S, Schaap C, Preijers F, Jansen JH, Blijlevens N, Inoue N, Muus P, Kinoshita T, Murakami Y. Paroxysmal nocturnal hemoglobinuria caused by CN-LOH of constitutional PIGB mutation and 70-kbp microdeletion on 15q. Blood Adv. 2020;4(22):5755–61.

21. Knaus A, Awaya T, Helbig I, Afawi Z, Pendziwiat M, Abu-Rachma J, Thompson MD, Cole DE, Skinner S, Annese F, Canham N, Schweiger MR, Robinson PN, Mundlos S, Kinoshita T, Munnich A, Murakami Y, Horn D, Krawitz PM. Rare Noncoding Mutations Extend the Mutational Spectrum in the PGAP3 Subtype of Hyperphosphatasia with Mental Retardation Syndrome. Hum Mutat. 2016;37(8):737–44.

22. Tarutani M, Itami S, Okabe M, Ikawa M, Tezuka T, Yoshikawa K, Kinoshita T, Takeda J. Tissue-specific knockout of the mouse Pig-a gene reveals important roles for GPI-anchored proteins in skin development. Proc Natl Acad Sci U S A. 1997;94(14):7400–5.

23. Kawagoe K, Kitamura D, Okabe M, Taniuchi I, Ikawa M, Watanabe T, Kinoshita T, Takeda J. Glycosylphosphatidylinositol-anchor-deficient mice: implications for clonal dominance of mutant cells in paroxysmal nocturnal hemoglobinuria. Blood. 1996 May;87(9):3600–6.

24. Lukacs M, Blizzard LE, Stottmann RW. CNS glycosylphosphatidylinositol deficiency results in delayed white matter development, ataxia and premature death in a novel mouse model. Hum Mol Genet. 2020;29(7):1205–17.

25. Ahrens MJ, Li Y, Jiang H, Dudley AT. Convergent extension movements in growth plate chondrocytes require gpi-anchored cell surface proteins. Development. 2009;136(20):3463–74.

26. Visconte V, Raghavachari N, Liu D, Keyvanfar K, Desierto MJ, Chen J, Young NS. Phenotypic and functional characterization of a mouse model of targeted Pig-a deletion in hematopoietic cells. Haematologica. 2010;95(2):214–23.

27. Kawagoe K, Kitamura D, Okabe M, Taniuchi I, Ikawa M, Watanabe T, Kinoshita T, Takeda J. Glycosylphosphatidylinositol-anchor-deficient mice: Implications for clonal dominance of mutant cells in paroxysmal nocturnal hemoglobinuria. Blood. 1996;87(9):3600–6.

28. Tarutani M, Itami S, Okabe M, Ikawa M, Tezuka T, Yoshikawa K, Kinoshita T, Takeda J. Tissue-specific knockout of the mouse Pig-a gene reveals important roles for GPI-anchored proteins in skin development. Proc Natl Acad Sci U S A. 1997;94(14):7400–5.

29. Lukacs M, Roberts T, Chatuverdi P, Stottmann RW. Glycosylphosphatidylinositol biosynthesis and remodeling are required for neural tube closure, heart development, and cranial neural crest cell survival. Elife. 2019;8:1–30.

30. McKean DM, Niswander L. Defects in GPI biosynthesis perturb Cripto signaling during forebrain development in two new mouse models of holoprosencephaly. Biol Open. 2012;1(9):874–83.

31. de los Santos MR, Rivalan M, David FS, Stumpf A, Pitsch J, Tsortouktzidis D, Moreno Velasquez L, Voigt A, Schilling K, Mattei D, Long M, Vogt G, Knaus A, Fischer-Zirnsak B, Wittler L, Timmermann B, Robinson PN, Horn D, Mundlos S, Kornak U, Becker AJ, Schmitz D, Winter Y, Krawitz PM. A CRISPR-Cas9 – engineered mouse model for GPI-anchor deficiency mirrors human phenotypes and exhibits hippocampal synaptic dysfunctions. Proc Natl Acad Sci U S A. 2021;118(2).

32. Hsu PD, Lander ES, Zhang F. Development and applications of CRISPR-Cas9 for genome engineering. Cell [Internet]. 2014;157(6):1262–78. Available from: http://dx.doi.org/10.1016/j.cell.2014.05.010

33. Jinek M, Chylinski K, Fonfara I, Hauer M, Doudna JA, Charpentier E. A programmable dual-RNA-guided DNA endonuclease in adaptive bacterial immunity. Science. 2012 Aug;337(6096):816–21.

34. Rouet P, Smih F, Jasin M. Introduction of double-strand breaks into the genome of mouse cells by expression of a rare-cutting endonuclease. Mol Cell Biol. 1994;14(12):8096–106.

35. Takashima Y, Sakuraba M, Koizumi T, Sakamoto H, Hayashi M, Honma M. Dependence of DNA double strand break repair pathways on cell cycle phase in human lymphoblastoid cells. Environ Mol Mutagen. 2009 Dec;50(9):815–22.

36. Renaud J-B, Boix C, Charpentier M, De Cian A, Cochennec J, Duvernois-Berthet E, Perrouault L, Tesson L, Edouard J, Thinard R, Cherifi Y, Menoret S, Fontaniere S, de Croze N, Fraichard A, Sohm F, Anegon I, Concordet J-P, Giovannangeli C. Improved Genome Editing Efficiency and Flexibility Using Modified Oligonucleotides with TALEN and CRISPR-Cas9 Nucleases. Cell Rep. 2016 Mar;14(9):2263–72.

37. Richardson CD, Ray GJ, DeWitt MA, Curie GL, Corn JE. Enhancing homology-directed genome editing by catalytically active and inactive CRISPR-Cas9 using asymmetric donor DNA. Nat Biotechnol. 2016 Mar;34(3):339–44.

38. Kraft K, Geuer S, Will AJ, Chan WL, Paliou C, Borschiwer M, Harabula I, Wittler L, Franke M, Ibrahim DM, Kragesteen BK, Spielmann M, Mundlos S, Lupiáñez DG, Andrey G. Deletions, inversions, duplications: Engineering of structural variants using CRISPR/Cas in mice. Cell Rep. 2015;10(5):833–9.

39. Brodsky RA, Mukhina GL, Li S, Nelson KL, Chiurazzi PL, Buckley JT, Borowitz MJ. Improved detection and characterization of paroxysmal nocturnal hemoglobinuria using fluorescent aerolysin. Am J Clin Pathol. 2000;114(3):459–66.

40. Yusa K, Horie K, Kondoh G, Kouno M, Maeda Y, Kinoshita T, Takeda J. Genome-wide phenotype analysis in ES cells by regulated disruption of Bloom's syndrome gene. Nature. 2004;429(6994):896–9.

41. Kojic M, Gaik M, Kiska B, Salerno-Kochan A, Hunt S, Tedoldi A, Mureev S, Jones A, Whittle B, Genovesi LA, Adolphe C, Brown DL, Stow JL, Alexandrov K, Sah P, Glatt S, Wainwright BJ. Elongator mutation in mice induces neurodegeneration and ataxia-like behavior. Nat Commun [Internet]. 2018;9(1). Available from: http://dx.doi.org/10.1038/s41467-018-05765-6

42. Sou Y, Kakuta S, Kamikubo Y, Niisato K, Sakurai T, Parajuli LK, Tanida I, Saito H, Suzuki N, Sakimura K, Maeda Y, Kinoshita T, Uchiyama Y, Koike M. Cerebellar Neurodegeneration and Neuronal Circuit Remodeling in Golgi pH Regulator-Deficient Mice. Eneuro. 2019;6(3):ENEURO.0427-18.2019.

43.     Stempel AV, Stumpf A, Zhang HY, Özdoğan T, Pannasch U, Theis AK, Otte DM, Wojtalla A, Rácz I, Ponomarenko A, Xi ZX, Zimmer A, Schmitz D. Cannabinoid Type 2 Receptors Mediate a Cell Type-Specific Plasticity in the Hippocampus. Neuron. 2016;90(4):795–809.

44.     Van Loo KMJ, Rummel CK, Pitsch J, Müller JA, Bikbaev AF, Martinez-Chavez E, Blaess S, Dietrich D, Heine M, Becker AJ, Schoch S. Calcium channel subunit α2σ4 is regulated by early growth response 1 and facilitates epileptogenesis. J Neurosci. 2019;39(17):3175–87.

45.     Mattei D, Ivanov A, van Oostrum M, Pantelyushin S, Richetto J, Mueller F, Beffinger MM, Schellhammer L, vom Berg J, Wollscheid B, Beule D, Paolicelli RC, Meyer U. Enzymatic dissociation induces transcriptional and proteotype bias in brain cell populations. 2020;(Md):1–20.

46.     Jirkof P. Burrowing and nest building behavior as indicators of well-being in mice. J Neurosci Methods [Internet]. 2014;234:139–46. Available from: http://dx.doi.org/10.1016/j.jneumeth.2014.02.001

47.     Vargas LM, Leal N, Estrada LD, González A, Serrano F, Araya K, Gysling K, Inestrosa NC, Pasquale EB, Alvarez AR. EphA4 activation of c-Abl mediates synaptic loss and LTP blockade caused by amyloid-β oligomers. PLoS One. 2014;9(3).

48.     Horn D, Wieczorek D, Metcalfe K, Barić I, Paležac L, Cuk M, Petković Ramadža D, Krüger U, Demuth S, Heinritz W, Linden T, Koenig J, Robinson PN, Krawitz P. Delineation of PIGV mutation spectrum and associated phenotypes in hyperphosphatasia with mental retardation syndrome. Eur J Hum Genet [Internet]. 2014;22(6):762–7. Available from: http://eutils.ncbi.nlm.nih.gov/entrez/eutils/elink.fcgi?dbfrom=pubmed&id=24129430&retmode=ref&cmd=prlinks%5Cnpapers2://publication/doi/10.1038/ejhg.2013.241

49.     Parri M, Buricchi F, Giannoni E, Grimaldi G, Mello T, Raugei G, Ramponi G, Chiarugi P. EphrinA1 activates a Src/focal adhesion kinase-mediated motility response leading to rho-dependent actino/myosin contractility. J Biol Chem. 2007;282(27):19619–28.

50.     Ledergerber D, Moser EI. Memory Retrieval: Taking the Route via Subiculum. Curr Biol. 2017;27(22):R1225–7.

51.     Janes PW, Griesshaber B, Atapattu L, Nievergall E, Hii LL, Mensinga A, Chheang C, Day BW, Boyd AW, Bastiaens PI, Jørgensen C, Pawson T, Lackmann M. Eph receptor function is modulated by heterooligomerization of A and B type Eph receptors. J Cell Biol. 2011;195(6):1033–45.

52. Dorey K, Engen JR, Kretzschmar J, Wilm M, Neubauer G, Schindler T, Superti-Furga G. Phosphorylation and structure-based functional studies reveal a positive and a negative role for the activation loop of the c-Abl tyrosine kinase. Oncogene. 2001;20(56):8075–84.

53. Tuomisto L, Lozeva V, Valjakka A, Lecklin A. Modifying effects of histamine on circadian rhythms and neuronal excitability. Behav Brain Res. 2001;124(2):129–35.

54. Thakkar MM. Histamine in the regulation of wakefulness. Sleep Med Rev [Internet]. 2011;15(1):65–74. Available from: http://dx.doi.org/10.1016/j.smrv.2010.06.004

55. Holtgrewe M, Knaus A, Hildebrand G, Pantel JT, de los Santos MR, Neveling K, Goldmann J, Schubach M, Jäger M, Coutelier M, Mundlos S, Beule D, Sperling K, Krawitz PM. Multisite de novo mutations in human offspring after paternal exposure to ionizing radiation. Sci Rep. 2018;8(1):1–5.

# 8.) Statuary Declaration

"I, Enrique Miguel Rodriguez de los Santos, by personally signing this document in lieu of an oath, hereby affirm that I prepared the submitted dissertation on the topic "The $Pigv^{341E}$ mouse model for GPI anchor deficiency displays behavioral alterations and shows reduced synaptic transmission in the hippocampus ", independently and without the support of third parties, and that I used no other sources and aids than those stated.

All parts which are based on the publications or presentations of other authors, either in letter or in spirit, are specified as such in accordance with the citing guidelines. The sections on methodology (in particular regarding practical work, laboratory regulations, statistical processing) and results (in particular regarding figures, charts and tables) are exclusively my responsibility.

Furthermore, I declare that I have correctly marked all of the data, the analyses, and the conclusions generated from data obtained in collaboration with other persons, and that I have correctly marked my own contribution and the contributions of other persons (cf. declaration of contribution). I have correctly marked all texts or parts of texts that were generated in collaboration with other persons.

My contributions to any publications to this dissertation correspond to those stated in the below joint declaration made together with the supervisor. All publications created within the scope of the dissertation comply with the guidelines of the ICMJE (International Committee of Medical Journal Editors; www.icmje.org) on authorship. In addition, I declare that I shall comply with the regulations of Charité – Universitätsmedizin Berlin on ensuring good scientific practice.

I declare that I have not yet submitted this dissertation in identical or similar form to another Faculty.

The significance of this statutory declaration and the consequences of a false statutory declaration under criminal law (Sections 156, 161 of the German Criminal Code) are known to me."


Date                                                        Signature

# 9.) Author Contribution

**Title:** "A CRISPR-Cas9–engineered mouse model for GPI-anchor deficiency mirrors human phenotypes and exhibits hippocampal synaptic dysfunctions"

**Authors:** Miguel Rodríguez de los Santos, Marion Rivalan, Friederike S. David, Alexander Stumpf, Julika Pitsch, Despina Tsortouktzidis, Laura Moreno Velasquez, Anne Voigt, Karl Schilling, Daniele Mattei, Melissa Long, Guido Vogt, Alexej Knaus, Björn Fischer-Zirnsak, Lars Wittler, Bernd Timmermann, Peter N. Robinson, Denise Horn, Stefan Mundlos, Uwe Kornak, Albert J. Becker, Dietmar Schmitz, York Winter, and Peter M. Krawitz

**Journal:** Proceedings of the National Academy of Sciences
**Publication Date:** 5.1.2021

**Author contribution in details:**

Peter M. Krawitz and **Miguel Rodriguez de los Santos** conceptualized and designed the study.

**Miguel Rodriguez de los Santos** performed and analyzed the flow cytometry experiments (Fig. 1A, Fig. S1E), hindlimb clasping test (Fig. 1D), histology experiments (sample processing, synaptophysin-immunofluorescence staining, Nissl staining) (Fig.5A, Fig.S10A-C) with the scientific support of Björn Fischer-Zirnsak, Uwe Kornak, and Peter M. Krawitz and the technical support of Guido Vogt and Alexej Knaus. Furthermore, **Miguel Rodriguez de los Santos** performed CRISPR-Cas9 experiments in mES cells with the scientific support of Stefan Mundlos and the technical support of Björn Fischer-Zirnsak and Alexej Knaus (Fig. S1A-D). Tetraploid aggregation of mES cells was performed by the transgenic core facility lead by Lars Wittler (Fig. S1A). Karl Schilling performed and analyzed histology experiments of the

cerebellum (Fig. S11A-F). **Miguel Rodriguez de los Santos** performed behavioral experiments (Fig. 2A-F, Fig. 3A-H, Fig. 4A-D, Fig. S2A-D, Fig. S4G-H, Fig. S5A-D, Fig. S6A-F, Fig. S7A-D, Fig. S8A-D, Fig. S9A-E) with the scientific support of Marion Rivalan and York Winter and the technical support of Melissa Long. **Miguel Rodriguez de los Santos** analyzed the data from the motor, social, cognitive, species-specific and affective-behavior tests (Fig. 3A-H, Fig. 4A-D, Fig. S6A-E, Fig. S7A-D, Fig. S8A-D, Fig. S9A-E) and Marion Rivalan analyzed the HCS and SAM data with the input of **Miguel Rodriguez de los Santos** (Fig. 2A-F, Fig. S2A-D, Fig. S3A-L, Fig. S4A-H, Fig. S5A-D). Electrophysiology recordings on acute slices and sample preparation was performed by Alexander Stumpf, Laura Moreno Velasquez and Anne Voigt under the supervision of Dietmar Schmitz (Fig. 5B-D). Data from electrophysiology recordings were analyzed by Alexander Stumpf (Fig.5B-D). Experiments in the PTZ kindling model were performed by Julika Pitsch and Despina Tsortouktzidis under the supervision of Albert J. Becker (Fig. 5E). Julika Pitsch analyzed the data from the PTZ experiments. For single-cell RNA sequencing (Fig. 6A-G, Fig. S12-18) of hippocampal cells, **Miguel Rodriguez de los Santos** carried out the isolation of hippocampal cells with the technical support from Daniele Mattei. Furthermore, library preparation was carried by the sequencing core facility lead by Bernd Timmermann. Bioinformatic analysis of single-cell RNA sequencing data was performed by Friederike S. David with the input of **Miguel Rodriguez de los Santos** (Fig. 6A-G).

**Miguel Rodriguez de los Santos** designed the figures. Figure 2 and Figure S2-5 was designed by **Miguel Rodriguez de los Santos** with the input of Marion Rivalan. Figure 6 and Figure S12-S18 was designed by **Miguel Rodriguez de los Santos** with the input of Friederike S. David. Figure S11 was designed by **Miguel Rodriguez de los Santos** with the input of Karl Schilling.

**Miguel Rodriguez de los Santos**, Marion Rivalan, Friederike S. David, Alexander Stumpf, Karl Schilling, Björn Fischer-Zirnsak, Uwe Kornak, Albert J. Becker, Dietmar Schmitz and Peter M. Krawitz discussed the data.

**Miguel Rodriguez de los Santos** and Peter M. Krawitz wrote the manuscript with the input of Marion Rivalan, Friederike S. David, Julika Pitsch, Peter N. Robinson and Denise Horn.


Berlin,


_____

Signature of the Student

# 10.) Excerpt of Journal Summary List "Multidisciplinary Sciences"

Journal Data Filtered By:  **Selected JCR Year: 2018** Selected Editions: SCIE,SSCI
Selected Categories: **"MULTIDISCIPLINARY SCIENCES"** Selected Category
Scheme: WoS
**Gesamtanzahl: 69 Journale**

| Rank | Full Journal Title | Total Cites | Journal Impact Factor | Eigenfactor Score |
|------|--------------------|-------------|-----------------------|-------------------|
| 1 | NATURE | 745,692 | 43.070 | 1.285010 |
| 2 | SCIENCE | 680,994 | 41.037 | 1.070190 |
| 3 | National Science Review | 1,842 | 13.222 | 0.006500 |
| 4 | Science Advances | 21,901 | 12.804 | 0.110010 |
| 5 | Nature Communications | 243,793 | 11.878 | 1.103290 |
| 6 | Nature Human Behaviour | 1,230 | 10.575 | 0.006550 |
| 7 | PROCEEDINGS OF THE NATIONAL ACADEMY OF SCIENCES OF THE UNITED STATES OF AMERICA | 661,118 | 9.580 | 1.022190 |
| 8 | Science Bulletin | 3,569 | 6.277 | 0.009840 |
| 9 | Scientific Data | 3,240 | 5.929 | 0.015610 |
| 10 | Frontiers in Bioengineering and Biotechnology | 1,994 | 5.122 | 0.006540 |
| 11 | Journal of Advanced Research | 2,691 | 5.045 | 0.004780 |
| 12 | Research Synthesis Methods | 1,932 | 5.043 | 0.005420 |
| 13 | GigaScience | 2,674 | 4.688 | 0.012510 |
| 14 | Annals of the New York Academy of Sciences | 46,385 | 4.295 | 0.025840 |
| 15 | Scientific Reports | 302,086 | 4.011 | 1.061540 |
| 16 | Journal of the Royal Society Interface | 12,933 | 3.224 | 0.029190 |
| 17 | NPJ Microgravity | 203 | 3.111 | 0.000670 |
| 18 | PHILOSOPHICAL TRANSACTIONS OF THE ROYAL SOCIETY A-MATHEMATICAL PHYSICAL AND ENGINEERING SCIENCES | 19,227 | 3.093 | 0.028200 |

1

Selected JCR Year: 2018; Selected Categories: "MULTIDISCIPLINARY SCIENCES"

# A CRISPR-Cas9–engineered mouse model for GPI-anchor deficiency mirrors human phenotypes and exhibits hippocampal synaptic dysfunctions

Miguel Rodríguez de los Santos[a,b,c,d], Marion Rivalan[e,f], Friederike S. David[d,g], Alexander Stumpf[h], Julika Pitsch[i,j], Despina Tsortouktzidis[i], Laura Moreno Velasquez[h], Anne Voigt[h], Karl Schilling[k], Daniele Mattei[l], Melissa Long[e,f], Guido Vogt[a,c], Alexej Knaus[d], Björn Fischer-Zirnsak[a,c], Lars Wittler[m], Bernd Timmermann[n], Peter N. Robinson[o,p], Denise Horn[a], Stefan Mundlos[a,c], Uwe Kornak[a,c,q], Albert J. Becker[i], Dietmar Schmitz[h], York Winter[e,f], and Peter M. Krawitz[d,1]

[a]Institute for Medical Genetics and Human Genetics, Charité–Universitätsmedizin Berlin, 13353 Berlin, Germany; [b]Berlin-Brandenburg School for Regenerative Therapies, Charité-Universitätsmedizin Berlin, 13353 Berlin, Germany; [c]Research Group Development and Disease, Max Planck Institute for Molecular Genetics, 14195 Berlin, Germany; [d]Institute for Genomic Statistics and Bioinformatics, University of Bonn, 53127 Bonn, Germany; [e]Animal Outcome Core Facility of the NeuroCure Center, Charité–Universitätsmedizin Berlin, 10117 Berlin, Germany; [f]Institute of Cognitive Neurobiology, Humboldt University, 10117 Berlin, Germany; [g]Institute of Human Genetics, Faculty of Medicine, University Hospital Bonn, 53127 Bonn, Germany; [h]Neuroscience Research Center, Charité–Universitätsmedizin Berlin, 10117 Berlin, Germany; [i]Section for Translational Epilepsy Research, Department of Neuropathology, University Hospital Bonn, 53127 Bonn, Germany; [j]Department of Epileptology, University Hospital Bonn, 53127 Bonn, Germany; [k]Anatomisches Institut, Anatomie und Zellbiologie, Faculty of Medicine, University of Bonn, 53115 Bonn, Germany; [l]Institute of Veterinary Pharmacology and Toxicology, University of Zürich (UZH), 8057 Zürich, Switzerland; [m]Department Developmental Genetics, Max Planck Institute for Molecular Genetics, 14195 Berlin, Germany; [n]Sequencing Core Facility, Max Planck Institute for Molecular Genetics, 14195 Berlin, Germany; [o]The Jackson Laboratory for Genomic Medicine, Farmington, CT 06032; [p]Institute for Systems Genomics, University of Connecticut, Farmington, CT 06032; and [q]Institute of Human Genetics, University Medical Center Göttingen, 37073 Göttingen, Germany

Pathogenic germline mutations in *PIGV* lead to glycosylphosphatidylinositol biosynthesis deficiency (GPIBD). Individuals with pathogenic biallelic mutations in genes of the glycosylphosphatidylinositol (GPI)-anchor pathway exhibit cognitive impairments, motor delay, and often epilepsy. Thus far, the pathophysiology underlying the disease remains unclear, and suitable rodent models that mirror all symptoms observed in human patients have not been available. Therefore, we used CRISPR-Cas9 to introduce the most prevalent hypomorphic missense mutation in European patients, *Pigv*:c.1022C > A (p.A341E), at a site that is conserved in mice. Mirroring the human pathology, mutant *Pigv*[341E] mice exhibited deficits in motor coordination, cognitive impairments, and alterations in sociability and sleep patterns, as well as increased seizure susceptibility. Furthermore, immunohistochemistry revealed reduced synaptophysin immunoreactivity in *Pigv*[341E] mice, and electrophysiology recordings showed decreased hippocampal synaptic transmission that could underlie impaired memory formation. In single-cell RNA sequencing, *Pigv*[341E]-hippocampal cells exhibited changes in gene expression, most prominently in a subtype of microglia and subicular neurons. A significant reduction in *Abl1* transcript levels in several cell clusters suggested a link to the signaling pathway of GPI-anchored ephrins. We also observed elevated levels of *Hdc* transcripts, which might affect histamine metabolism with consequences for circadian rhythm. This mouse model will not only open the doors to further investigation into the pathophysiology of GPIBD, but will also deepen our understanding of the role of GPI-anchor–related pathways in brain development.

GPI-anchor deficiency | disease modeling | hippocampal synaptic defect

The glycosylphosphatidylinositol (GPI) anchor is essential for connecting a remarkable number of proteins (GPI-linked proteins) to the cell membrane. GPI-linked proteins are essential for signal transduction, cell–cell adhesion, axonal outgrowth, synapse formation, and plasticity, as well as for regulation of the complement system (1, 2). Paroxysmal nocturnal hemoglobinuria (PNH) was the first disorder to be characterized as a GPI-anchor biosynthesis deficiency (GPIBD) (3). However, PNH is exceptional in two regards: First, it is the only GPIBD that is acquired and it is due to somatic mutations that cause complete loss of

function. In inherited GPIBDs, also referred to as inherited GPI-anchor biosynthesis deficiencies (IGDs), residual GPI-anchor synthesis and maturation activities persist. Second, the prevalence of inherited GPIBDs is at least 10-fold higher than that of PNH. To date, recessive phenotypes have been reported for 21 genes of the GPI-anchor pathway. Bellai-Dussault et al. discussed the clinical variability in detail for the first 19 GPIBDs (4). However, most patients, including recently described cases due to GPIBD20 and GPIBD21, exhibit intellectual disability, psychomotor delay, and epilepsy (5, 6). Furthermore, due to the residual GPI-anchor synthesis and maturation, patient-derived fibroblasts have a reduced number of GPI-linked proteins on the cell surface (7).

## Significance

Inherited GPI-anchor biosynthesis deficiencies (IGDs) explain many cases of syndromic intellectual disability. Although diagnostic methods are improving, the pathophysiology underlying the disease remains unclear. Furthermore, we lack rodent models suitable for characterizing cognitive and social disabilities. To address this issue, we generated a viable mouse model for an IGD that mirrors the condition in human patients with a behavioral phenotype and susceptibility to epilepsy. Using this model, we obtained neurological insights such as deficits in synaptic transmission that will facilitate understanding of the pathophysiology of IGDs.

NEUROSCIENCE

Prior to the discovery of IGD, mouse models of GPI-anchor deficiency (8–12), which mainly employed chimeric and conditional knockouts in which GPI-anchor biosynthesis was abolished in specific tissues, demonstrated that a complete loss of GPI anchors is embryonic lethal (9). Interestingly, the resultant phenotypes were often still so severe that the mutant mice died early, suggesting essential functions of GPI-anchor proteins in the skin, development of white matter, and dendritic arborization of Purkinje cells in the cerebellum (8, 10). In recent years, mice with constitutional GPIBDs were identified in mutation screens; these animals were viable probably because the mutations were only hypomorphic or affected isoforms that are limited to certain tissues, and therefore only explain some aspects of most inherited GPIBDs (13, 14). Lukacs et al. (13) showed that a missense mutation in *Pgap2*, p.(M1V), compromised transcription of this gene particularly in neural crest cells, resulting in a craniofacial phenotype in mutant mice. In contrast to most other genes involved in GPI-anchor biosynthesis and maturation, *Pgap2* has a tissue-specific expression pattern that changes over embryonic development, and the existence of multiple isoforms in humans further complicates phenotypic comparisons between humans and mice. It is likely that the facial abnormalities described in human patients with a similar mutation, p.(M1R), are due to a similar mechanism; however, the other phenotypic features seem to be milder in humans, either because the substituted amino acid is different or because the isoforms resulting in p.(M52R) and p.(M58R) do not exist in mice. In addition, McKean and Niswander observed a holoprosencephaly-like phenotype in two mouse models with a frame-shift mutation in *Pign* and an in-frame deletion in *Pgap1* (14).

Because most of the existing mouse models die at an early stage due to the severe phenotype, it has not been possible to use these models to characterize cognitive deficits, which represent the main challenge in individuals with IGDs. For this purpose, we used CRISPR-Cas9 to engineer a mouse model with the missense mutation c.1022C > A, p.A341E in *Pigv*, one of the most frequently encountered pathogenic alleles in humans (15). *PIGV* encodes mannosyl transferase II, which is essential for the attachment of the second mannose to the GPI anchor (16). Due to the residual function of *Pigv*[341E], mutant mice are viable with a normal life span, making it possible to complete behavioral experiments that test motor, social, and cognitive abilities, and study the brain tissue, as well as cells of these mice.

## Results

Patients with IGDs exhibit a heterogeneous spectrum of symptoms, including neurologic findings, movement disorders, and intellectual disability (7, 17–19). In general, IGDs caused by pathogenic mutations in genes that catalyze the early steps of GPI-anchor synthesis, such as *PIGA*, tend to have more severe clinical features such as status epilepticus. In patients with mutations in later steps of synthesis, such as *PIGV*, epilepsies also occur in a substantial proportion of cases; however, they often disappear later in life, and intellectual disability becomes the key clinical feature. In contrast to acquired GPIBDs, such as PNH, all patients with IGDs have some residual function of GPI-anchor synthesis, implying that null mutants are not viable and that at least one hypomorphic allele must be present. When a novel mutation is encountered in a suspected IGD, flow cytometry with two or more different markers serves to confirm a GPIBD. To analyze the effect of *Pigv*[341E] on a cellular level, we used fluoroproaerolysin (FLAER), which can recognize all GPI-anchored proteins, and CD90, a GPI-linked protein that is highly expressed in human fibroblasts. The mean fluorescence intensity (MFI) of FLAER was reduced in hom-*Pigv*[341E] mouse embryonic fibroblasts (MEFs) (Fig. 1*A*). Likewise, CRISPR-Cas9–engineered mouse embryonic stem (mES) cell clones (hom-*Pigv*[341E], hom-*Pgap3*[107L]) exhibited partial reductions in FLAER and GPI-

anchored CD90 (*SI Appendix*, Fig. S1*E*). Unlike clones with homozygous hypomorphic mutations, the null mES clone [*Pigv* $(^{-/-})$] exhibited almost no cell-surface expression of FLAER and CD90 (*SI Appendix*, Fig. S1*E*). Therefore, we concluded that *Pigv*[341E] is hypomorphic in mice, as it is in humans.

The results section is structured as follows: We will start with a description of the findings from behavioral experiments. Some of the dysfunctional behavior that we encountered, motivated further histopathological and electrophysiological analysis of the hippocampus that pointed to a synaptopathy. In the end, we present the results of a single cell transcriptome screen that we conducted to identify differentially expressed genes that might be involved in the observed pathophysiology.

**Characteristic Features and Alterations of Sleep Patterns in *Pigv*[341E] Mice.** The most prominent differences that we observed first between *Pigv*[341E] and wild-type (WT) mice were reduced weight (Fig. 1*B* and *SI Appendix*, Fig. S1*F*) and hindlimb clasping behavior (Fig. 1 *C* and *D*). Due to the intellectual disability and psychomotor delay that are the key clinical features of IGD, patients are impaired in their everyday lives. Therefore, we sought to determine which spontaneous behaviors our mouse model exhibited while living undisturbed in their home cage (singly or group housed). Using HomeCageScan (HCS), we monitored singly housed *Pigv*[341E] mice for 23 h at two different time points (8 and 16 wk). Among the 19 behaviors accurately detected by analysis of the HCS data, three behaviors were consistently altered in *Pigv*[341E] mice at both time points. *Pigv*[341E] mice hung less often to the top of the cage (total occurrences) and for shorter durations (total duration and duration per hour) than wild-type mice; groomed more often (total occurrences) and for longer durations (total duration and duration per hour); and slept less (total duration and duration per hour) (Fig. 2 *A* and *B* and *SI Appendix*, Fig. S2*A*). At the earlier time point, *Pigv*[341E] mice spent more time walking (duration per hour) during the dark phase of the day than wild-type mice (Fig. 2*B*, *Top* graph). Furthermore, at both time points, hanging behavior was an important variable for differentiating genotypes along the dimensions of a principal component analysis (PCA) (*SI Appendix*, Figs. S3 *A–F* and S4 *A–F*).

We also used the social activity monitor (SAM) to assess spontaneous home-cage activity in *Pigv*[341E] mice while living in a group setting. For this test, we implanted a radio-frequency identification (RFID) transponder into the mice and put the home cage with mixed genotypes on a grid box that could locate individual animals and their position in the cage at all times (continuous 24 h/day recording). Because the animals were undisturbed in their home cage, SAM analysis could be performed several times without the animals noticing. For the first two time points (9 and 17 wk), SAM analysis revealed no difference between genotypes in total distance traveled over 14 d (*SI Appendix*, Fig. S4*G*), but an unexpected switch in diurnal/nocturnal activity for both genotypes was observed. The mice were more active during the light (normal sleeping time) than the dark phases of their days (*SI Appendix*, Fig. S5 *A and C*; confirmed by Markov chain Monte Carlo generalized linear mixed-effects models [MCMCglmm], pMCMC = 0.001). This observation supported the HCS data that *Pigv*[341E] mice slept less, which is a feature of some patients with IGDs who suffer from sleep disturbances (7, 20). We performed a second experiment in which we evaluated the spontaneous activity of the *Pigv*[341E] and wild-type mice separately (nonmixed vs. mixed-genotype cages). When *Pigv*[341E] and wild-type mice lived together in the same cage (mixed genotype), we reproduced our previous results: Mice of different genotypes exhibited no difference in total distance traveled over 4 d (Fig. 2*C*, *Left* graph), per phase (Fig. 2*D*, *Left* graph), per day (*SI Appendix*, Fig. S2*C*), and per hour (*SI Appendix*, Fig. S2*D*), but they still exhibited higher
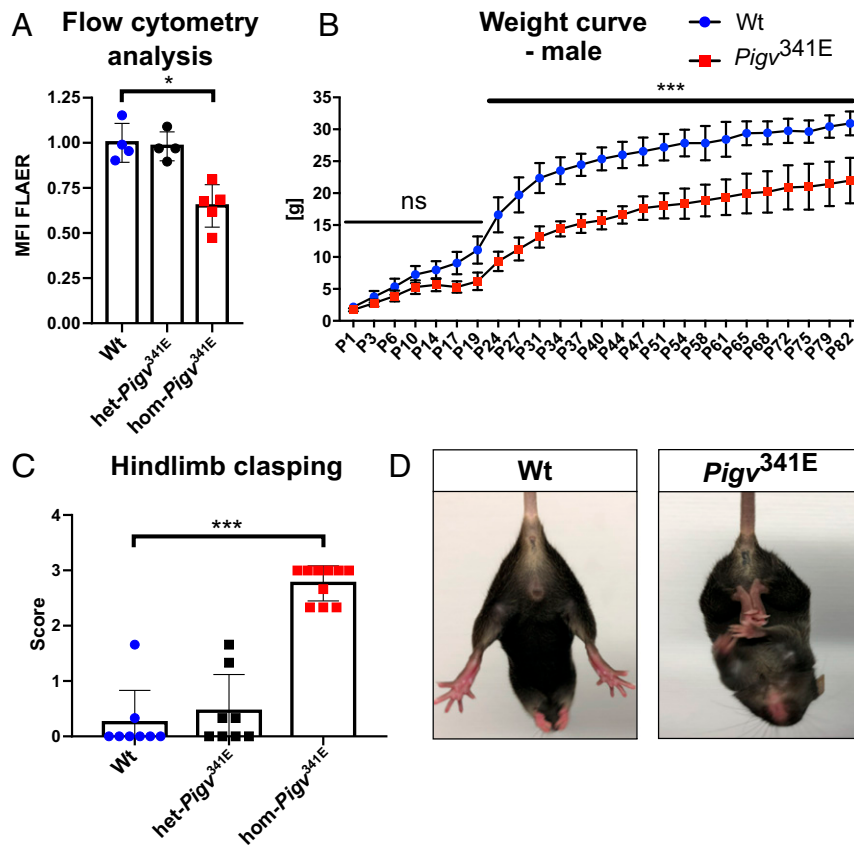
28

**Fig. 1.** Features of *Pigv*[341E] mice. (*A*) Flow cytometry analysis of hom-*Pigv*[341E] MEFs isolated from embryos (E13.5) revealed a reduced MFI of FLAER. MFI was normalized against the wild type. (*B*) Male *Pigv*[341E] mice had a reduced weight on postnatal days (P) 1 to 82. (*C*) Hom-*Pigv*[341E] mice exhibited hindlimb clasping behavior. (*D*) Representative posture of hindlimb clasping behavior in hom-*Pigv*[341E] mice. By contrast, wild-type mice spread their hindlimbs when picked up by their tail. Hom-*Pigv*[341E] = homozygous for Pigv p.Ala341Glu; het-*Pigv*[341E] = heterozygous for Pigv p.Ala341Glu. Animals used for the weight curve: WT(male = 3), hom(male = 4). Animals used for the hindlimb clasping test were 6 wk old: WT(female $n = 3$, male $n = 5$), het-*Pigv*[341E](female $n = 4$, male $n = 4$), hom-*Pigv*[341E](female $n = 4$, male= $n = 6$). Data from the weight curve were analyzed by two-way ANOVA followed by Bonferroni's multiple comparisons test. The data from flow cytometry and the hindlimb clasping test were analyzed by nonparametric *t* test (Mann–Whitney). \*$P < 0.05$, \*\*\*$P < 0.001$. ns, not significant.

activity levels (larger variability) during the light vs. dark phase (*SI Appendix*, Fig. S2D, confirmed by MCMCglmm, pMCMC = 0.001). However, in nonmixed housing conditions *Pigv*[341E] mice walked greater distances over 4 d (Fig. 2*C*, *Right* graph), per phase (Fig. 2*D*, *Right* graph), per day, and per hour (Fig. 2 *E* and *F*) than wild-type mice, and again, *Pigv*[341E] mice were more active during the light than the dark cycle on days 1 and 2 (Fig. 2*E*).

***Pigv*[341E] Mice Exhibit Motor Dysfunction and Alterations in Sociability.** Extensive testing of various motor functions in *Pigv*[341E] mice revealed a clear and elaborated dysfunctional motor phenotype. *Pigv*[341E] mice had reduced balance and motor coordination, reflected by a reduced latency of falling off the rotarod (Fig. 3*A*). This was confirmed by an elevated latency of traversing an elevated beam (Fig. 3*B*). In the rope grip test, *Pigv*[341E] mice exhibited an elevated latency of climbing on the rope, and had a lower hanging score than wild-type mice (Fig. 3*C* and *SI Appendix*, Fig. S6A, *Right* graph). Furthermore, *Pigv*[341E] mice had reduced grip strength (Fig. 3*D*). Next, we evaluated the walking pattern of *Pigv*[341E] mice using the footprint test (Fig. 3*E*). *Pigv*[341E] mice had a larger distance between forepaw and hindpaw (S) in paw placement of the stride (Fig. 3*F*); this is remarkable because walking mice usually place their hind paws in the same positions as their forepaws (Fig. 3*E*, see WT).

We evaluated social behavior in *Pigv*[341E] mice in the social proximity and three-chamber tests. In the social proximity test,

*Pigv*[341E] mice exhibited a reduced number of "rear up" behaviors and an elevated number of nose-to-anogenital contacts with the stranger mouse (Fig. 3*G*). However, no differences in the number of nose-tip-to-nose-tip, nose-to-head-contact, "crawl over," or "crawl under" behaviors were observed between genotypes (*SI Appendix*, Fig. S7A). In the three-chamber test, *Pigv*[341E] mice spent more time with the stranger mouse than in the vicinity of the empty cage (Fig. 3*H*). Furthermore, the discrimination ratio (stranger vs. empty cage) was higher in *Pigv*[341E] than in wild-type mice (*SI Appendix*, Fig. S7D, *Right* graph).

***Pigv*[341E] Mice Exhibit Cognitive Deficits in Spatial Long-Term Memory and Species-Specific Hippocampus-Dependent Functions.** To characterize the cognitive and affective profile of *Pigv*[341E] mice, we performed a battery of tests to assess aspects of spatial learning and memory, species-specific functions (Barnes maze, y-maze, marble burying, and nest building behavior), and spontaneous response to novel, open, and elevated or bright environments (open field, elevated plus maze, and dark/light box). In the Barnes maze test, *Pigv*[341E] mice were delayed in spatial learning, as indicated by an elevated latency to escape during days 1 to 3 (Fig. 4*A*). Despite this delay in spatial learning during days 1 to 3, *Pigv*[341E] mice had learned the location of the escape box by day 4 and exhibited normal short-term spatial memory at day 5. However, *Pigv*[341E] mice had impaired long-term spatial memory at day 12, reflected by an elevated latency to escape (Fig. 4*A*).
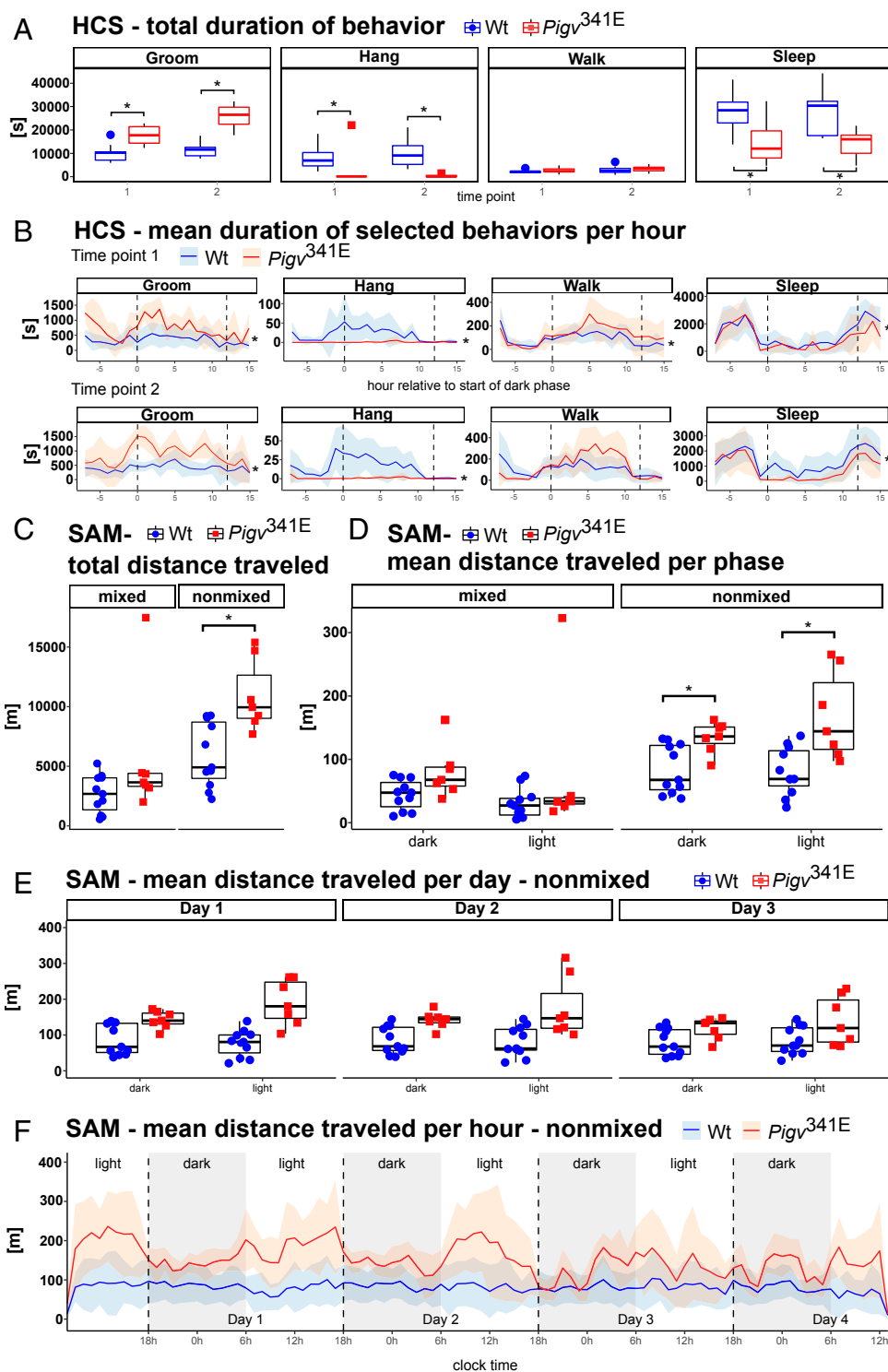
Rodríguez de los Santos et al.
A CRISPR-Cas9–engineered mouse model for GPI-anchor deficiency mirrors human phenotypes and exhibits hippocampal synaptic dysfunctions

**Fig. 2.** *Pigv*[341E] mice exhibit a behavioral phenotype in HCS and an elevated activity level in the SAM (second approach). (*A*) Duration of selected behaviors from the HCS. *Pigv*[341E] mice revealed elevated grooming and reduced hanging and sleeping behavior at both time points. (*B*) Duration of selected behaviors per hour, as determined by HCS. The dark phase took place between the two dashed vertical lines. *Pigv*[341E] mice exhibited elevated grooming and hanging and reduced sleeping at both time points. *Pigv*[341E] mice exhibited elevated walking at time point 1. (*C*) The SAM revealed an elevation in total distance traveled by *Pigv*[341E] mice when animals were separated by genotype (nonmixed). When housed in mixed genotypes (mixed), total distance traveled did not significantly differ between genotypes. (*D*) *Pigv*[341E] mice exhibited an increase in distance traveled per phase when separated by genotype (nonmixed). When housed in mixed genotype (mixed), total distance traveled per phase did not significantly differ between genotypes. (*E* and *F*) *Pigv*[341E] mice traveled longer distances per day and per hour when separated by genotype (nonmixed). *Pigv*[341E] = homozygous for Pigv p.Ala341Glu. Animals used for the HCS (WT: female *n* = 8, male *n* = 4; *Pigv*[341E]: female *n* = 4, male *n* = 2) were phenotyped at two different consecutive time points: tp1 at the age of 8 wk, and tp2 at the age of 16 wk. Animals used for the SAM: WT(female *n* = 4, male *n* = 6) *Pigv*[341E](female *n* = 2, male *n* = 5). Data from the HCS (total duration) and SAM (total distance, mean distance traveled per phase and per day) were analyzed by Wilcoxon rank-sum test (nonparametric). Data from the HCS (duration per hour) and SAM (distance traveled per hour) were analyzed with a glmm using a MCMC. *P* < 0.05.
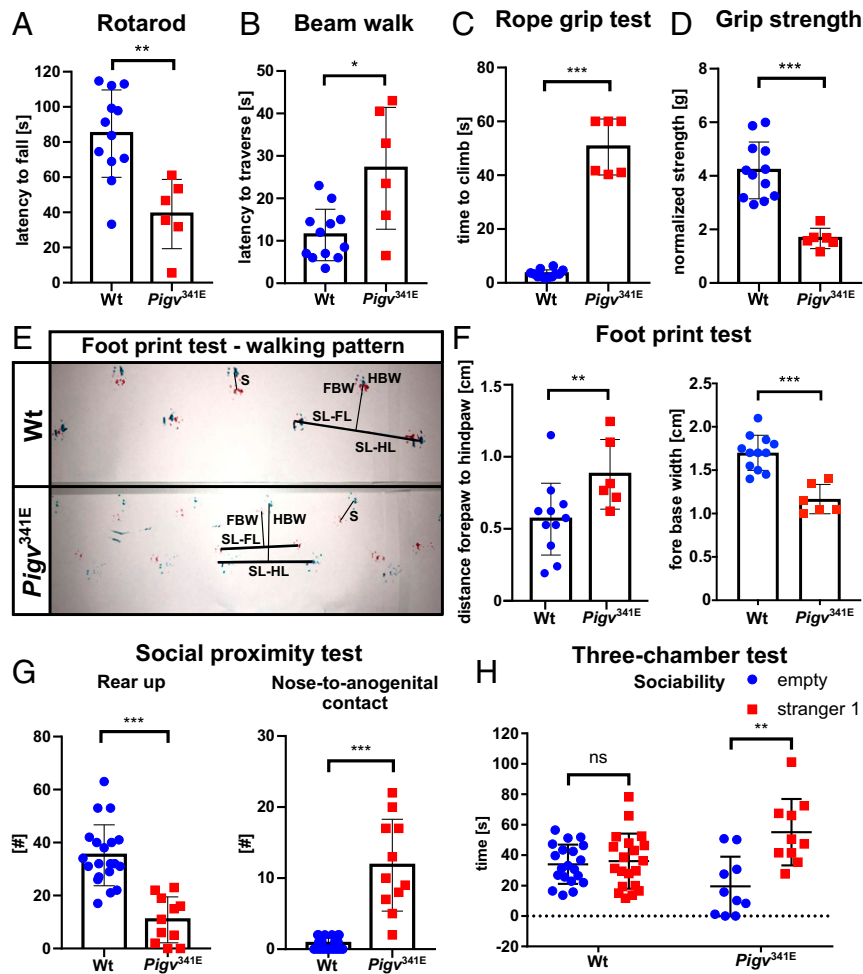
30

**Fig. 3.** $Pigv^{341E}$ mice exhibit motor dysfunctions. (*A* and *B*) $Pigv^{341E}$ mice exhibited a reduction in motor coordination, reflected by a reduced latency of falling off the rotarod and elevated latency of traversal of the beam (diameter, 15 mm). (*C*) $Pigv^{341E}$ mice exhibited a reduction in climbing performance, reflected by a decrease in the time spent climbing the rope. (*D*) $Pigv^{341E}$ mice exhibited a reduced grip strength, as determined by grip strength meter. [g] was normalized to the weight of the animal. (*E*) Representative image of walking pattern between genotypes. SL–FL = stride length–forelimb, SL–HL = stride length–hindlimb, FBW = fore–base width, HBW = hind–base width, S = distance between forepaw and hindpaw. (*F*) $Pigv^{341E}$ mice had an altered walking pattern, reflected by an increase in the distance between forepaw to hindpaw and a decrease in fore–base width. (*G*) $Pigv^{341E}$ mice exhibited enhanced social approach behavior, reflected by a decrease in "rear up" behavior and an increase in the number of nose-to-anogenital contacts in the social proximity test. (*H*) The three-chamber test (first 5 min) indicated that $Pigv^{341E}$ mice exhibited an enhanced social approach behavior relative to wild-type mice, reflected by spending more time with the stranger mouse than with the empty. $Pigv^{341E}$ = homozygous for Pigv p.Ala341Glu. Animals used in the motor tests were 7 wk old: WT(female $n$ = 8, male $n$ = 4) $Pigv^{341E}$(female $n$ = 4, male $n$ = 2). Animals used in the social proximity test: WT(female $n$ = 9, male $n$ = 11), $Pigv^{341E}$(female $n$ = 4, male $n$ = 2). Animals used in the three-chamber test: WT(female $n$ = 9, male $n$ = 11), $Pigv^{341E}$(female $n$ = 4, male $n$ = 6). The data from the motor tests and the social proximity test were analyzed by nonparametric $t$ test (Mann–Whitney). The data from the three-chamber test were analyzed by two-way ANOVA followed by Bonferroni's multiple comparisons test. *$P < 0.05$, **$P < 0.01$, ***$P < 0.001$. ns, not significant.

Similar to the results that measured latency to escape, $Pigv^{341E}$ mice had an elevated path length for days 1 to 4 and 12, but not day 5 (Fig. 4*B*). Furthermore, $Pigv^{341E}$ mice spent less time in the target quadrant than wild-type mice at day 12, confirming deficits in long-term spatial memory (*SI Appendix*, Fig. S8*B*, *Right* graph). In the y-maze test, similar spontaneous alternation behavior between genotypes suggested normal short-term spatial working memory in $Pigv^{341E}$ mice (*SI Appendix*, Fig. S8*A*). In the species-specific and hippocampus-dependent tests of marble burying and nest construction (21), $Pigv^{341E}$ mice buried fewer marbles and had lower-quality nests (Fig. 4 *C* and *D*).

$Pigv^{341E}$ mice behaved similarly to wild-type mice in the dark/light box and elevated plus maze (*SI Appendix*, Fig. S9 *A* and *B*). In the open field test, $Pigv^{341E}$ mice spent less time in the center and more time in the periphery than wild-type mice (*SI Appendix*, Fig. S9*C*). Moreover, the path length and number of visits to the center were reduced in $Pigv^{341E}$ mice (*SI Appendix*, Fig. S9 *D* and *E*).

**$Pigv^{341E}$ Mice Exhibit Defects in Synaptic Transmission.** Because $Pigv^{341E}$ mice exhibited cognitive impairments in spatial learning and memory, we hypothesized a hippocampal defect, and this idea was supported by the reduced burrowing and nest building behavior (hippocampus-dependent) in $Pigv^{341E}$ mice. Hence, we decided to analyze the hippocampus in more detail. Nissl staining revealed no morphological abnormalities in the hippocampus of $Pigv^{341E}$ mice (*SI Appendix*, Fig. S10*C*). Because many GPI-linked proteins play crucial roles in synapse formation and plasticity, causing deficits that can be detected in cell culture (22), we performed immunostaining to visualize synaptophysin, a presynaptic marker. We observed a decreased immunoreactivity for synaptophysin in cornu ammonis 1–stratum radiatum
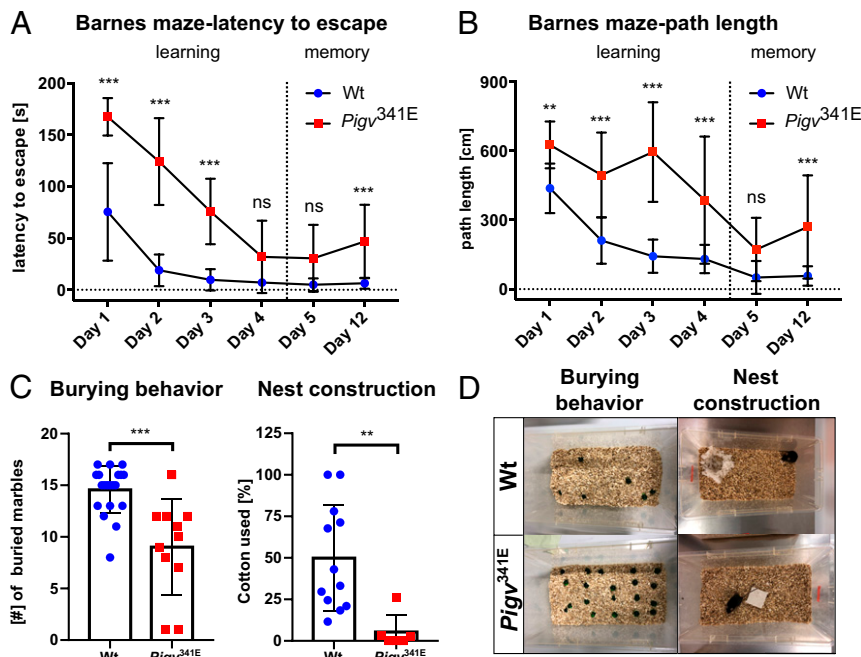
Rodríguez de los Santos et al.
A CRISPR-Cas9–engineered mouse model for GPI-anchor deficiency mirrors human phenotypes and exhibits hippocampal synaptic dysfunctions

PNAS | 5 of 11
https://doi.org/10.1073/pnas.2014481118

31

**Fig. 4.** *Pigv*[341E] mice exhibit cognitive deficits in learning and memory. (*A* and *B*) *Pigv*[341E] mice exhibited cognitive deficits in learning and long-term memory, reflected by increases in latency to escape and path length on days 1 to 3 (learning) and day 12 (long-term memory in the Barnes maze). (*C*) *Pigv*[341E] mice exhibited a decrease in burying and nest construction behavior. (*D*) Representative image of burrowing behavior (*Left*) and nest construction behavior (*Right*) of wild-type and *Pigv*[341E] mice. *Pigv*[341E] = homozygous for Pigv p.Ala341Glu. Animals used in the Barnes maze: WT(female $n = 8$, male $n = 11$), *Pigv*[341E](female $n = 4$, male $n = 6$). Animals used in the marble-burying test: WT(female $n = 9$, male $n = 11$), *Pigv*[341E](female $n = 4$, male $n = 7$). Animals used in the nest construction test were 7 wk old: WT(female $n = 8$, male $n = 4$), *Pigv*[341E](female $n = 4$, male $n = 2$). The data from the nest construction and marble-burying tests were analyzed with a nonparametric *t* test (Mann–Whitney). The data from the Barnes maze (latency to escape, path length) were analyzed by two-way ANOVA followed by Bonferroni's multiple comparisons test. *$P < 0.05$ **$P < 0.01$, ***$P < 0.001$. ns, not significant.

(CA1–SR) of *Pigv*[341E] mice (Fig. 5*A*). By contrast, we observed no significant differences between genotypes in cornu ammonis 3–stratum radiatum (CA3–SR) or cornu ammonis 1–molecular layer of dentate gyrus (CA1–ML) (*SI Appendix,* Fig. S10 *A* and *B*). To determine whether the behavioral abnormalities were accompanied by deficits in synaptic transmission, we conducted electrophysiology recordings in the CA1–SR region, where synaptophysin levels were reduced in *Pigv*[341E] mice. We tested input–output functions and observed lower amplitudes of excitatory postsynaptic potential (EPSPs) at different stimulation intensities in *Pigv*[341E] mice (Fig. 5*B*). In paired pulse facilitation (PPF), *Pigv*[341E] mice exhibited an elevated paired pulse ratio (PPR) (Fig. 5*C*). Moreover, posttetanic potentiation (PTP) exhibited elevated facilitation in *Pigv*[341E] mice (Fig. 5*D*).

**Increased Susceptibility of *Pigv*[341E] Mice to Chemically Induced Acute Seizures.** Considering the altered electrophysiological properties in *Pigv*[341E] mice, we examined for differences in the seizure threshold between *Pigv*[341E] and corresponding littermate wild-type mice in an acute epilepsy model, the pentylenetetrazole (PTZ)-induced kindling model (23). To this end, mice were repetitively exposed to PTZ (10 mg/kg, i.p.) every 10 min until the occurrence of a first focal-to-bilateral tonic–clonic seizure occurred. Intriguingly, *Pigv*[341E] mice exhibited a significantly lower seizure threshold, manifesting as a reduced latency to first seizure than wild-type mice, which exhibited convulsive seizures after PTZ exposure. Wild-type animals manifested generalized seizures after 93.3 min, whereas in *Pigv*[341E] mice, the first seizure manifested already after 63.3 min (Fig. 5*E, Middle* graph). Furthermore, the observation that four wild-type animals did not exhibit any seizure after 10 injections, whereas all *Pigv*[341E] mice did, underlines the higher susceptibility of *Pigv*[341E] mice for seizure induction via PTZ ($\chi^2 = 105.3$, df = 4, $P < 0.0001$)

(Fig. 5*E, Left* graph). In addition, *Pigv*[341E] mice exhibited more severe seizures than wild-type mice ($\chi^2 = 74.21$, df = 1, $P < 0.0001$) (Fig. 5*E, Right* graph).

**Shift in Relative Cell Count of Hippocampal Cellular Subgroups in *Pigv*[341E] Mice.** The synaptic defect in the CA1–SR region of *Pigv*[341E] mice could have been responsible for the observed impairments in spatial learning and memory. To identify the cell types most affected by GPIBD, we performed single-cell RNA sequencing on freshly isolated hippocampal cells after cognitive behavioral tests. The isolation of hippocampal cells was performed as previously described (24). Based on the gene expression profiles of 8,800 single cells from *Pigv*[341E] mice and 7,100 cells from wild-type animals, we defined 17 cellular subgroups (Fig. 6*A*). Cells from both *Pigv*[341E] and wild-type mice were present in all subgroups, but the distributions differed between genotypes ($\chi^2 = 306.49$, df = 16, $P < 2.2 \times 10^{-16}$). While the fractions of granule cells, oligodendrocytes, and a microglia subpopulation (microglia 3) were reduced in pooled samples from *Pigv*[341E] mice, the proportions of subicular neurons (neurons subiculum 1), GABAergic (inhibitory) interneurons, and fibroblast-like cells were higher than in the pooled wild-type samples (Fig. 6*B*).

***Pigv*[341E] Hippocampal Cells Exhibit a Deregulation in Gene Expression Related to Synapse Organization and Signaling Transduction.** Expression analysis of single-cell RNA sequencing data revealed multiple genes that were differentially expressed between *Pigv*[341E] and wild-type cells within each cellular subgroup (Fig. 6*C*). In the mutant mice, nonreceptor tyrosine kinase *Abl1* was down-regulated, whereas histidine decarboxylase *Hdc*, cytochrome P450 member *Cyp4x1*, and predicted lncRNA *Gm14216* were up-regulated, both within and across all cellular subgroups (Fig. 6*D* and
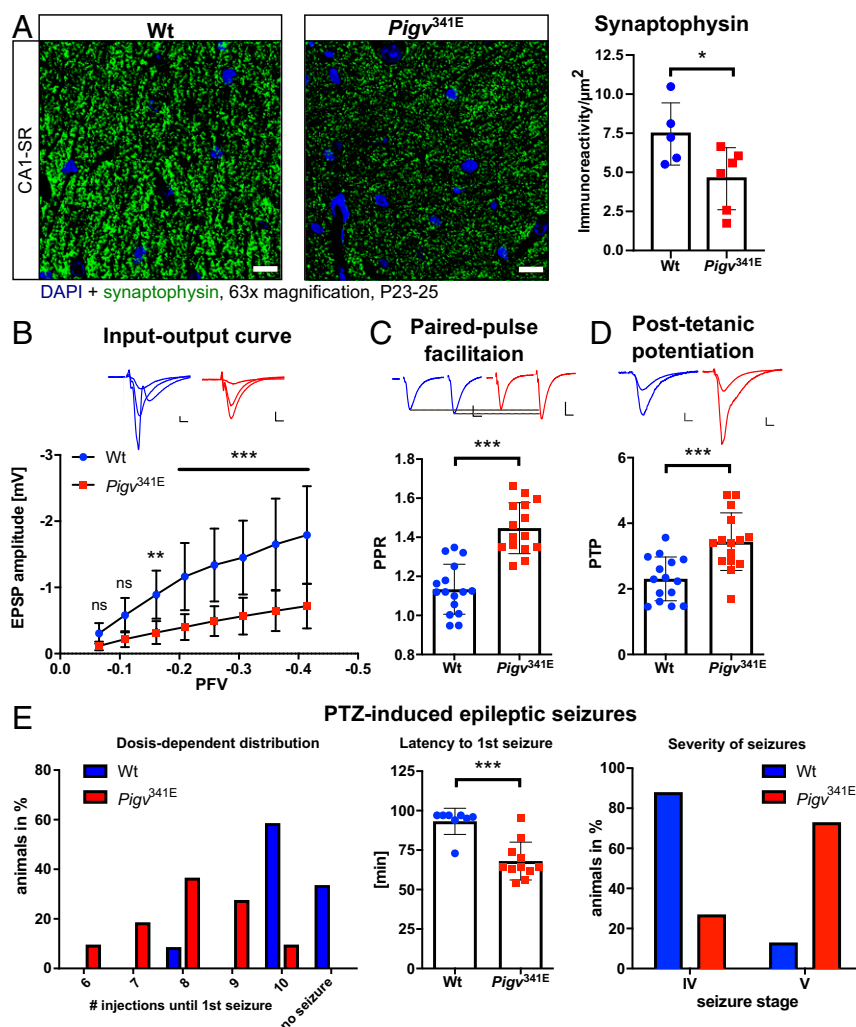
32

**Fig. 5.** $Pigv^{341E}$ exhibit a hippocampal synaptic defect. (*A*) Representative images of immunofluorescence staining show less synaptophysin immunoreactivity (green) in CA1–SR of $Pigv^{341E}$ mice. 4′,6-diamidino-2-phenylindole (DAPI) staining is shown in blue. (Scale bar: 10 μm.) Synaptophysin immunoreactivity per μm², quantified using FIJI ImageJ, was significantly reduced in CA1–SR in $Pigv^{341E}$ mice (*Right*). (*B*) Input–output: EPSP amplitude was reduced in $Pigv^{341E}$ mice at different presynaptic fiber volleys (PFVs). (Scale bar: L indicates 0.2 mV/5 ms.) (*C*) PPF revealed an elevated PPR in $Pigv^{341E}$ mice. (Scale bar: L indicates 0.2 mV/10 ms.) (*D*) PTP was elevated in $Pigv^{341E}$ mice. (Scale bar: L indicates 0.2 mV/5 ms.) (*E*) In the PTZ kindling model $Pigv^{341E}$ mice had a significantly different seizure threshold compared to that of wild-type control littermates (*Left* graph). In $Pigv^{341E}$ mice the latency to the first convulsive seizure was significantly reduced (*Middle* graph). Furthermore, the seizure phenotype appears more severe (*Right* graph). $Pigv^{341E}$ = homozygous for Pigv p.Ala341Glu. Animals used for the synaptophysin-staining were 3 wk old: WT(female $n = 3$, male $n = 2$) $Pigv^{341E}$(female $n = 2$, male $n = 4$). Animals used for the electrophysiology recordings: WT(female $n = 2$, male $n = 2$) $Pigv^{341E}$(female $n = 2$, male $n = 2$). Animals used for the PTZ model: WT(female $n = 3$, male $n = 9$) $Pigv^{341E}$(female $n = 5$, male $n = 6$). The data from the synaptophysin immunofluorescence staining and electrophysiology recordings (PPF, PTP) were analyzed by parametric Student's $t$ test. Furthermore, the data from the input–output curve were analyzed by two-way ANOVA followed by Bonferroni's multiple comparisons test. In the PTZ model, group comparisons (dose-dependent distribution, severity of seizures) were analyzed by $\chi^2$ test and latency to first seizure by unpaired Student's $t$ test with Welch's correction. *$P < 0.05$ **$P < 0.01$, ***$P < 0.001$.

---

*SI Appendix*, Figs. S16–S18). The most extensive change in gene expression within a cellular subgroup was observed in the first subgroup of subicular neurons and the third subgroup of microglia (Fig. 6*C* and *SI Appendix*, Figs. S16 and S17). We also performed Gene Ontology (GO) analysis of differentially expressed genes between genotypes, including terms in three categories: biological process, cellular component, and molecular function (Fig. 6 *E–G*). Among the differentially expressed genes in subicular neurons, the biological process term "regulation of synapse organization" was enriched in genes up-regulated in $Pigv^{341E}$ cells, whereas the biological process terms "cell morphogenesis" and "commissural neuron axon guidance" were enriched in down-regulated genes (Fig. 6*E*). Furthermore, the biological process term "cell–cell

adhesion via plasma-membrane adhesion molecules" was enriched in genes with elevated and reduced expression (Fig. 6*E*).

Single-cell RNA sequencing revealed three hippocampal microglia populations in both genotypes (Fig. 6 *A* and *B*, microglia 1 to 3). All three subpopulations expressed the marker genes *Csf1r* and *C1qa* (*SI Appendix*, Fig. S15). Among the most significant differentially expressed genes between the three microglia subgroups and all remaining cells in both genotypes, "cell activation," "migration," "phagocytosis," and "immune responses" were among the top 10 GO biological process terms in microglia 1 and 2 (Dataset S2). By contrast, the top 10 GO biological process terms in microglia 3 cells were "ribosome," "ribonucleoprotein complex biogenesis," and "cytoplasmic translation" (Dataset S2). Hence, we considered microglia 1 and
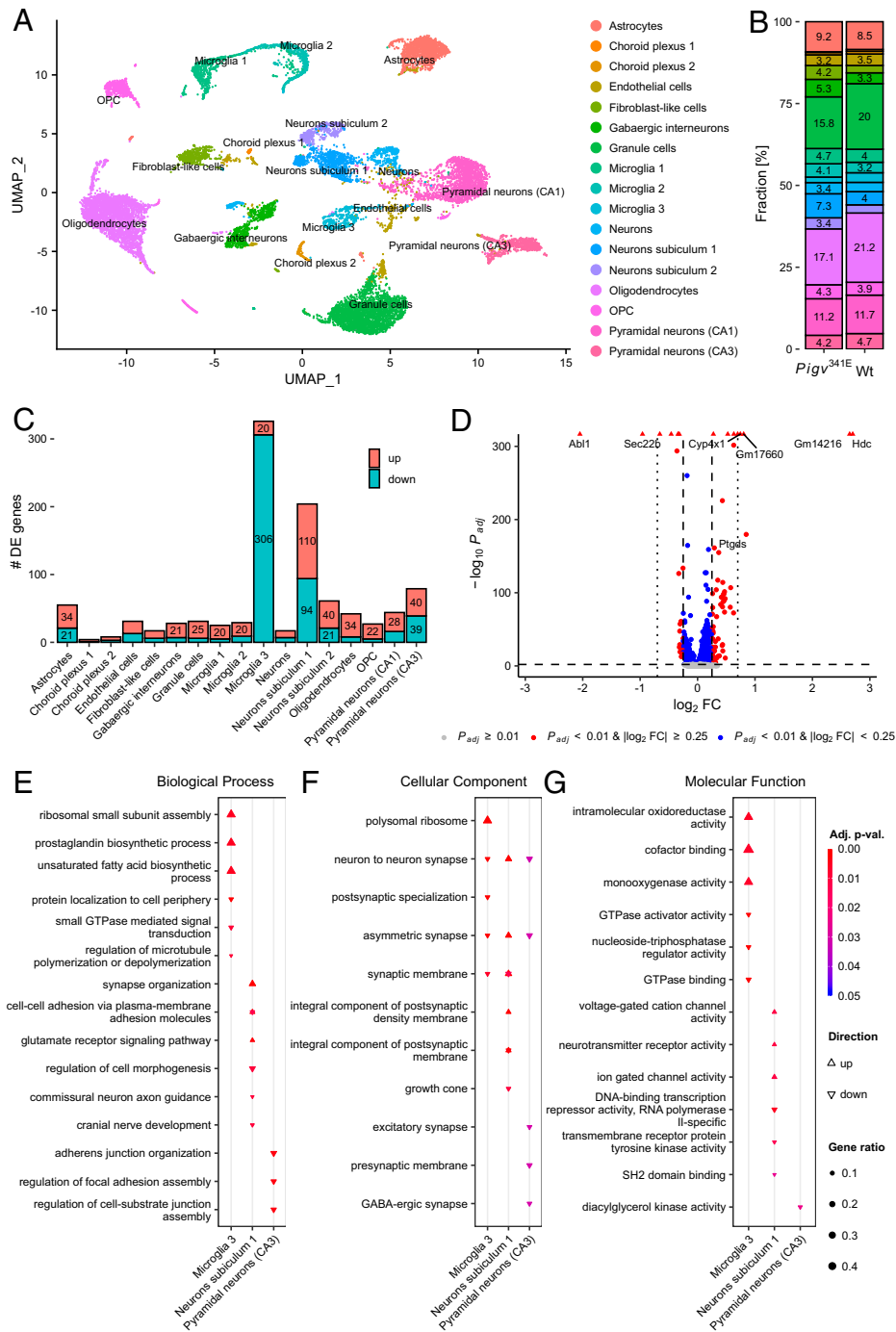
Rodríguez de los Santos et al.
A CRISPR-Cas9–engineered mouse model for GPI-anchor deficiency mirrors human phenotypes and exhibits hippocampal synaptic dysfunctions

PNAS | 7 of 11
https://doi.org/10.1073/pnas.2014481118

33

**Fig. 6.** Differences between *Pigv*[341E] and wild-type mice in the transcriptional landscape of single hippocampus cells. (*A*) Hippocampal cells from both *Pigv*[341E] and wild-type mice clustered into 17 cellular subgroups (*B*), with a skewed distribution of cells across subgroups in the *Pigv*[341E] sample relative to wild-type. Percentages below 3% are not shown for clarity. (*C*) Differential expression testing between *Pigv*[341E] and wild-type cells within each cellular subgroup yielded differentially expressed genes with absolute $\log_2$(fold change) $\geq$0.25 and adjusted *P* value $\leq$0.01. The most extensive changes in gene expression were observed for the third subgroup of microglia cells and the first subgroup of subicular neurons. Gene counts are not shown for sets with <20 differentially expressed genes. (*D*) Global comparison between all *Pigv*[341E] and wild-type cells highlights the hippocampus-wide effect on the genes *Abl1*, *Hdc*, *Cyp4x1*, and *Gm14216*, for which significant changes in expression were detected within each cellular subgroup. The dashed horizontal line is located at an adjusted *P* value of 0.01, the dashed vertical lines at an absolute $\log_2$(fold change) of 0.25, and the dotted vertical lines at an absolute $\log_2$(fold change) of 0.7. For genes with an absolute $\log_2$(fold change) >0.7, gene symbols are shown. Within the subgroups of microglia 3, neurons subiculum 1 and pyramidal neurons (CA3), GO enrichment analysis revealed a number of overrepresented biological process (*E*), cellular component (*F*), and molecular function (*G*) terms in the sets of genes differentially expressed between *Pigv*[341E] and wild-type cells within the cellular subgroups. For each set of genes that were up-regulated or down-regulated between genotypes, up to three terms with the lowest adjusted *P* value after removal of redundant GO terms are shown. The gene ratio, i.e., the number of genes annotated with a term divided by the respective number of differentially expressed genes, is encoded by point size. Cellular subgroups with no significantly enriched terms were omitted. GO terms enriched in differentially expressed genes with elevated or reduced expression within a subgroup are contracted into a single star-shaped symbol. OPC, oligodendrocyte precursor cells; DE genes, differentially expressed genes; FC, fold change; $P_{adj}$, adjusted *P* value. Pooled samples [WT(male = 4), *Pigv*[341E](male = 4)]. *n* = 1 per genotype.

34

2 cells as potentially more phagocytic and migratory than microglia 3 cells. We identified 326 genes that were differentially expressed between genotypes in microglia 3 cells. Remarkably, 306 of these 326 genes were down-regulated in microglia 3 cells of $Pigv^{341E}$ mutants (Fig. 6C). GO analysis revealed that the down-regulated genes were enriched for the biological process terms "small GTPase-mediated signal transduction" and "regulation of microtubule cytoskeleton polymerization and depolymerization" (Fig. 6E). In addition, we identified 20 genes differentially expressed between genotypes that were up-regulated in $Pigv^{341E}$ microglia 3 cells. Among these were *Rpl38*, *Rps21*, and *Rps28*, which encode ribosomal proteins.

CA3 pyramidal neurons project their axons to the CA1 region, where we observed dysfunction in synaptic transmission in $Pigv^{341E}$ mice. Therefore, we were particularly interested in the cellular subgroup of CA3 pyramidal neurons, in which we identified 79 genes that were differentially expressed between genotypes (Fig. 6C). GO analysis revealed that down-regulated genes were enriched for the terms "adherens junction organization," "regulation of cell-substrate junction assembly," and "focal adhesion assembly" in $Pigv^{341E}$ CA3 pyramidal neurons (Fig. 6E). Interestingly, we also observed enrichment of genes with reduced expression related to "neuron–neuron synaptic transmission," "regulation of synaptic vesicle exocytosis," and "synaptic vesicle transport" (Dataset S3).

## Discussion

$Pigv^{341E}$ is a mouse model for GPI-anchor deficiency with a hypomorphic mutation that is viable after weaning. The mice exhibited significant alterations in behavior that reflect key aspects of patients with IGD.

In these mice, we observed a severe motor phenotype that included deficits in motor coordination, grip or muscle strength, climbing, and hanging behavior (in HCS); alterations in walking pattern; and hindlimb clasping. Behavioral traits such as altered walking pattern, hindlimb clasping, and motor coordination deficits are usually observed in mouse models with ataxia-like behavior and cerebellar dysfunction (25, 26). In agreement with these findings, ataxia has been reported in some IGD patients, and an ataxia-like behavior was observed in a conditional *Piga* knockout mouse model (10, 19). Lukacs et al. analyzed the microscopic anatomy of cerebellum sections from their conditional *Piga* knockout mouse model and observed mild deficits in Purkinje cell arborization (10). However, in histologic analysis with various stainings, the cerebellum of our $Pigv^{341E}$ mutants did not exhibit any abnormalities (*SI Appendix*, Fig. S11 *A–F*), and the overall folial pattern appeared to be unchanged. In particular, calbindin staining exhibited no differences in Purkinje cell dendritic arborization between genotypes (*SI Appendix*, Fig. S11 *E and F*). Therefore, we hypothesize that deficits in dendritic arborization in this neuronal cell type, as reported by Lukacs et al. (10) require a more severe GPIBD than that induced by the hypomorphic mutation c.1022C > A in *Pigv*. This is consistent with the longer lifespan of our mouse model, which allowed us to analyze the associated cognitive deficits. In addition to the cerebellum, we focused on the hippocampus, where we performed histology and electrophysiology to achieve a deeper understanding of the memory and species-specific deficits. Although we did not observe significant morphological changes in the hippocampus, the input–output curve, PPR, and PTP were significantly altered in $Pigv^{341E}$ mice, indicating that electrophysiology is a sensitive functional assay for mouse models with mild GPIBD.

Because $Pigv^{341E}$ mice exhibited increased self-grooming, which is a repetitive, highly stereotyped pattern that is associated with autistic-like behavior in rodents (27), we suspected abnormalities in social behavior as well. Autistic features have been reported in a subgroup of patients with IGD due to pathogenic

mutations in *PGAP3* (7). By contrast, patients with *PIGV* deficiency are keen to interact socially despite their severe speech impairments. Interestingly, in $Pigv^{341E}$ mice we observed enhanced social approach behavior, reflected by an elevated number of nose-to-anogenital contacts and reduced "rear up" behavior in the social proximity test. The reduction in "rear up" behavior in $Pigv^{341E}$ mice suggested reduced social avoidance. The enhanced social approach behavior was confirmed in the three-chamber test: relative to wild-type controls, $Pigv^{341E}$ mice spent more time with the stranger mouse than in the vicinity of the empty cage. Comparable performance between genotypes in the buried food test ruled out compromised olfaction, a potential confounder in social behavior tests (*SI Appendix*, Fig. S7C). Taking into account the enhanced social approach behavior in $Pigv^{341E}$ mice, the positive social abilities of patients with *PIGV* deficiency seem to be characteristic of these individuals and should be considered during diagnosis. However, it remains unknown to what extent IGD patients who are affected in genes other than *PIGV* exhibit positive social abilities. In addition, because we did not observe social behavior characteristic of autism (28) in $Pigv^{341E}$ mice, and autistic features are seen only in a subgroup of patients with IGD, autism should not be considered as a specific feature of IGD.

$Pigv^{341E}$ mice exhibited a deficit in spatial long-term memory in the Barnes maze, correct short-term spatial memory, and short-term working memory (y-maze test). Furthermore, $Pigv^{341E}$ mice exhibited a delay in spatial learning relative to wild-type mice in the Barnes maze (days 1 to 3). In the Barnes maze, both latency to escape and path length were elevated in $Pigv^{341E}$ mice; therefore, we excluded the motor phenotype as a confounder. However, even though path length and latency to escape were elevated in $Pigv^{341E}$ mice, the number of visits to the wrong holes was not significantly altered on days 2 through 12 (*SI Appendix*, Fig. S8C). Analysis of the search strategy revealed that $Pigv^{341E}$ mice were targeting the correct hole without any errors (number of wrong holes) less often than wild-type mice (*SI Appendix*, Fig. S8D, direct strategy) (WT: 15.8%, $Pigv^{341E}$: 3.3%). Moreover, we quantified two further search strategies: random choice of a hole without any order and a serial strategy that tests holes one after another in close proximity. $Pigv^{341E}$ mice used more often the random strategy (WT: 9.7%, $Pigv^{341E}$: 56.7%), whereas wild-type mice used more often the serial strategy to find the correct hole (WT: 25.4%, $Pigv^{341E}$: 20.0%) (*SI Appendix*, Fig. S8D). In contrast to random guessing, the serial strategy has the advantage that it minimizes the path length and by that means will result in a quicker escape. However, the serial strategy results also in a higher number of errors. This potentially explains why the latency to escape was significantly elevated in $Pigv^{341E}$ mice, whereas the number of wrong holes did not significantly differ between genotypes.

Furthermore, we observed no difference between genotypes in affective-related behavior (dark/light box, elevated plus maze) except in the open field test, in which $Pigv^{341E}$ mice spent more time in the periphery than in the center. However, this observation could also represent a confounder due to the motor phenotype, as the number of entries to the center and the path length were also reduced in $Pigv^{341E}$ mice.

Interestingly, electrophysiology recordings revealed reduced synaptic transmission at CA1–SR in $Pigv^{341E}$ mice, consistent with the observed impairment in long-term spatial memory and hippocampus-dependent species-specific behaviors (marble-burying and nest construction test). While PTP and PPR were elevated in $Pigv^{341E}$ mice, the input–output curve was reduced, indicating a decrease in synaptic release probability. Due to the increase in PTP and PPR, and the reduced immunoreactivity of synaptophysin, a presynaptic vesicle protein, we hypothesize that the pool of readily releasable vesicles in the presynapse is reduced, resulting in a damped input–output curve in the postsynapse. Notably in this

Rodríguez de los Santos et al.
A CRISPR-Cas9–engineered mouse model for GPI-anchor deficiency mirrors human phenotypes and exhibits hippocampal synaptic dysfunctions

PNAS | 9 of 11
https://doi.org/10.1073/pnas.2014481118

35

regard, GO analysis of single-cell RNA sequencing data revealed that genes which were significantly down-regulated in $Pigv^{341E}$-CA3 pyramidal neurons were enriched for GO biological process terms associated with "synaptic transmission" and "vesicle transport." The impaired synaptic transmission in the hippocampi of $Pigv^{341E}$ mice was reflected in their lower threshold to the excitotoxin-induced epileptic events and aggravated seizures than wild-type mice.

Single-cell RNA sequencing data revealed the most prominent differences in gene expression in a subgroup of subicular neurons and microglia. In subicular neurons 1, up-regulated genes were associated with biological process terms such as "synapse organization." Because we observed a synaptic defect in CA1–SR, as revealed by immunohistochemistry and as further supported by electrophysiological recordings, we hypothesized a synaptic defect in the subiculum as well. The subiculum, an area of the hippocampus that is important for memory retrieval, is linked through microcircuits with the CA1 (29). Ledergerber and Moser (29) described two distinct circuits for memory acquisition and retrieval: memory acquisition involves the CA1 and medial-entorhinal cortex, whereas memory retrieval involves the CA1, the medial-entorhinal cortex, and the subiculum. Future studies should seek to determine whether memory acquisition, memory retrieval, or even both conditions are affected in $Pigv^{341E}$ mice.

Strikingly, 306 genes were down-regulated in $Pigv^{341E}$ microglia 3 cells. Therefore, microglia might play more important roles in GPI-anchor deficiency than previously thought. These genes were enriched in GO biological process terms "protein localization to cell periphery," "small GTPase-mediated signal transduction," and "regulation of microtubule polymerization or depolymerization." Small GTPases are important mediators of the cytoskeleton (30). Hence, we hypothesized that a GPI-anchor defect leads to down-regulation of small GTPase-mediated pathways, which has further consequences for cytoskeleton organization in this microglia subtype. In this regard, GPI-anchored ephrin A proteins could play an important role, as EphrinA1 regulates small GTPase (Rho)-dependent cytoskeleton rearrangement through Src/focal adhesion kinases (31).

Up to 0.5% of the eukaryotic proteins are GPI linked, with a broad range of functions including cell–cell adhesion, signal transduction, and antigen presentation (32). Therefore, it is surprising that the pathophysiology of acquired GPI-anchor deficiency PNH can be explained by the reduced expression of only two substrates, CD55 and CD59, which reduces the protection of cells against membrane attack complex (MAC), and can also be effectively treated by eculizumab, which inhibits complement activation (33). Likewise, analysis of mouse models of congenital forms of GPI-anchor deficiencies has aimed at identifying other lead targets. McKean and Niswander suggested a pivotal role of Cripto/TGFβ signaling in the development of holoprosencephaly (14), whereas Lukacs et al. discussed the role of GPI-anchored Folr1 in neural crest cells and the cranial neuroepithelium, and argued that compromise of Folr1 could be linked to the facial gestalt (13).

Interestingly, a considerable number of GPI-linked proteins are involved specifically in synapse formation and plasticity (1). Because $Pigv^{341E}$ mice exhibit a hippocampal synaptic defect, this subset of GPI-linked proteins, including GPI-linked EphrinA, may play pivotal roles in the development of the disease as well. Single-cell RNA sequencing analysis revealed that *Abl1*, which interacts on the protein level with several EphrinA receptors (*SI Appendix*, Fig. S6F) (34), was not only down-regulated in $Pigv^{341E}$ mice across all cellular subgroups, but also within each cellular subgroup. Our hypothesis is that the GPI-anchor defect in the hippocampus is especially critical for EphrinA signaling, and that defective GPI anchoring of EphrinA in turn reduces hippocampal EphrinA receptor and Abl1 activity. Notably in this regard, axon repulsion is EphrinA dependent and mediated through the Abl kinase family (35).

Along with *Abl1*, *Hdc* and *Ptgds* were also dysregulated in $Pigv^{341E}$ mice, with elevated expression across all cellular subgroups. *Hdc* encodes a histidine decarboxylase that catalyzes the conversion from histidine to histamine, an important neurotransmitter regulating circadian rhythm (36). In rodents, histamine levels are elevated during the dark phase to induce wakefulness and are reduced during the light phase to induce sleep (37). Furthermore, intracerebroventricular application of histamine triggers characteristic signs of wakefulness, such as elevated grooming and exploration behavior, which were also observed in $Pigv^{341E}$ mice (HCS and SAM) (37). In addition, during home-cage activity monitoring (group housed) and the HCS (individually housed), $Pigv^{341E}$ mice were more active during the light cycle and slept for shorter durations. Consequently, higher expression of *Hdc* may lead to higher production of histamine, thereby disturbing circadian rhythm and causing classical signs of wakefulness in $Pigv^{341E}$ mice during the light phase. However, it remains unknown how misregulation of *Hdc* is associated with GPI-anchor deficiency. Interestingly, in the conditional *Piga* knockout mouse model, bulk RNA sequencing of the cerebellum revealed an enrichment of deregulated genes associated with the circadian rhythm (10). Moreover, *Ptgds* encodes prostaglandin D2 synthase, which converts prostaglandin H2 (PGH2) into prostaglandin D2 (PGD2), which in turn induces sleep (38). PGD2 levels fluctuate with the circadian rhythm and are elevated in the cerebrospinal fluid when rats are sleep deprived (39). Therefore, up-regulation of *Ptgds* expression could be an indicator of sleep deprivation in $Pigv^{341E}$ mice. Because $Pigv^{341E}$ mice exhibit fewer resting phases during their classical inactive (light) phase, a careful analysis of sleep pattern in IGD patients is indicated. To date, sleep disturbances have mainly been reported in patients with *PGAP3* deficiency (19).

In summary, we have performed a deep phenotypic characterization of a mouse model that mirrors the symptoms of human patients with IGD. In addition, we detected a hippocampal synaptic defect that may impair spatial long-term memory and important species-specific behaviors for the survival of the animal. We hope that our model, as well as our phenotyping approach, will be useful in future studies aimed at a detailed elucidation of the pathomechanism of IGD and the response to therapeutic interventions.

## Materials and Methods

For full methods, see *SI Appendix, Supplementary Material and Methods*.

**Animals.** $Pigv^{341E}$ mice were generated by diploid or tetraploid aggregation (40) (*SI Appendix*, Fig. S1A) and maintained by crossing with C57BL.6/J mice. Mice were genotyped by PCR using the primers m*Pigv*Ex4_fw and m*Pigv*Ex4_rv. PCR amplicons were digested with *Bcu*I (Thermo Fisher Scientific) and subjected to agarose gel electrophoresis (*SI Appendix*, Fig. S1D). All animals were handled according to government regulations as approved by local authorities (LaGeSo Berlin and LANUV Recklinghausen). In addition, all experiments were carried out following the 3R (Replacement, Reduction and Refinement) guidelines for animal welfare. Mice were housed in groups with mixed genotypes in single ventilated cages with an enriched environment. The mice were housed in a pathogen-free animal facility with a 12 h dark/light cycle and had food and water ad libitum unless otherwise indicated. Mice used for experiments were 8 wk to 6 mo old unless otherwise indicated. $Pigv^{341E}$ and wild-type mice used in a given experiment were the same age. To avoid bias effects, littermates were assigned equally to both experimental groups, according to their genotype and sex. The experimenter was blinded except during behavioral testing, as $Pigv^{341E}$ mice were physically smaller. Moreover, experiments were randomized with respect to mouse genotype.

**Statistical Analysis.** For all experiments, at least four animals per genotype were used, except for the weight curve, for which at least three animals per genotype were used. One animal was defined as one biological replicate and represented one data point, except for electrophysiology recordings (see *SI Appendix, Schaffer collateral recordings*). Means and SDs were calculated for

36

each genotype group unless otherwise indicated. Data were statistically analyzed with GraphPad Prism (version 7) or R (version 3.6.3) (41), and results are expressed as means ± SDs. Statistical tests were performed for each experiment as indicated in Dataset S1. Results with $P$ value <0.05 were considered significant unless otherwise indicated.
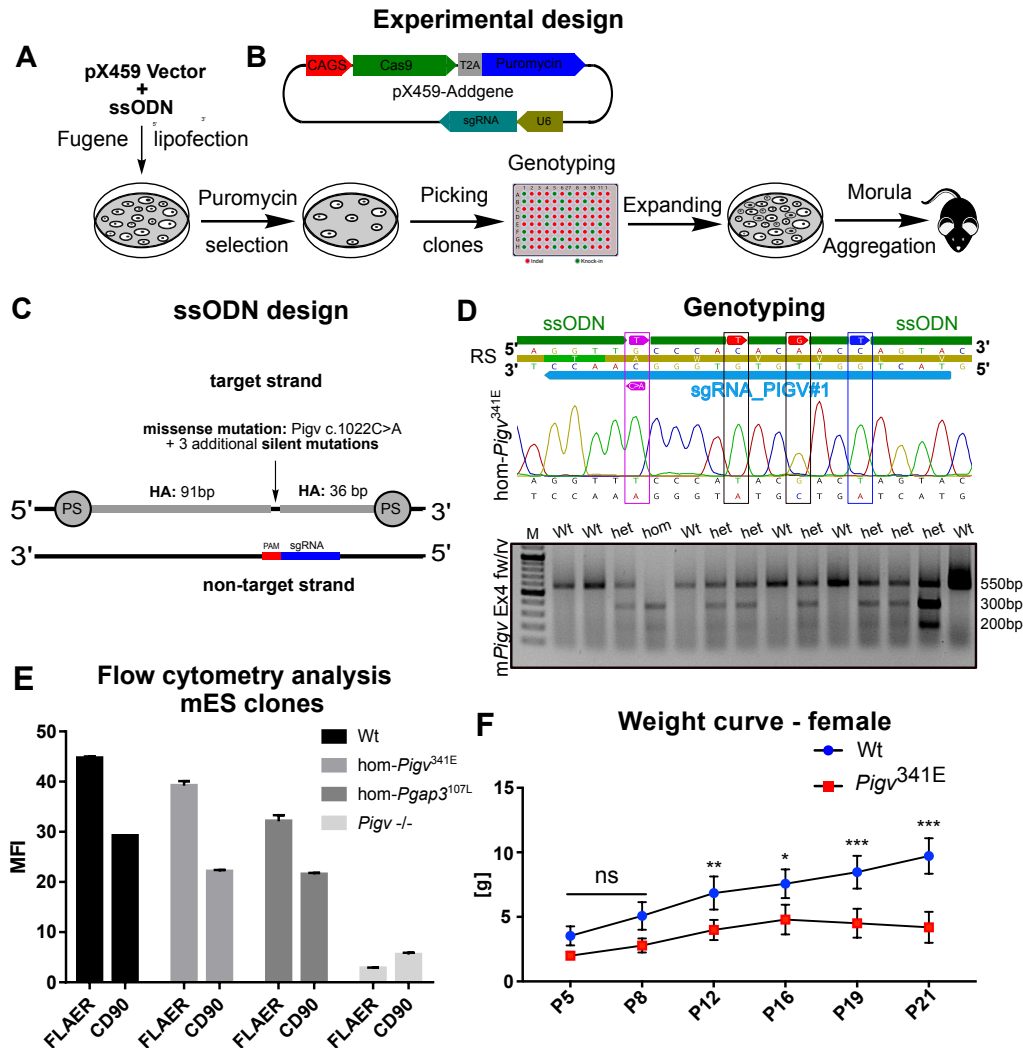
**Data Availability.** The single-cell RNA sequencing data are freely available from the Gene Expression Omnibus repository under accession number GSE147722.

1. J. W. Um, J. Ko, Neural glycosylphosphatidylinositol-anchored proteins in synaptic specification. *Trends Cell Biol.* **27**, 931–945 (2017).
2. M. G. Paulick, C. R. Bertozzi, The glycosylphosphatidylinositol anchor: A complex membrane-anchoring structure for proteins. *Biochemistry* **47**, 6991–7000 (2008).
3. J. Takeda et al., Deficiency of the GPI anchor caused by a somatic mutation of the PIG-A gene in paroxysmal nocturnal hemoglobinuria. *Cell* **73**, 703–711 (1993).
4. K. Bellai-Dussault, T. T. M. Nguyen, N. V. Baratang, D. A. Jimenez-Cruz, P. M. Campeau, Clinical variability in inherited glycosylphosphatidylinositol deficiency disorders. *Clin. Genet.* **95**, 112–121 (2019).
5. Y. Murakami et al., Mutations in PIGB cause an inherited GPI biosynthesis defect with an axonal neuropathy and metabolic abnormality in severe cases. *Am. J. Hum. Genet.* **105**, 384–394 (2019).
6. A. Knaus et al., Mutations in PIGU impair the function of the GPI transamidase complex, causing severe intellectual disability, epilepsy, and brain anomalies. *Am. J. Hum. Genet.* **105**, 395–402 (2019).
7. A. Knaus et al., Rare noncoding mutations extend the mutational spectrum in the PGAP3 subtype of hyperphosphatasia with mental retardation syndrome. *Hum. Mutat.* **37**, 737–744 (2016).
8. M. Tarutani et al., Tissue-specific knockout of the mouse Pig-a gene reveals important roles for GPI-anchored proteins in skin development. *Proc. Natl. Acad. Sci. U.S.A.* **94**, 7400–7405 (1997).
9. K. Kawagoe et al., Glycosylphosphatidylinositol-anchor-deficient mice: Implications for clonal dominance of mutant cells in paroxysmal nocturnal hemoglobinuria. *Blood* **87**, 3600–3606 (1996).
10. M. Lukacs, L. E. Blizzard, R. W. Stottmann, CNS glycosylphosphatidylinositol deficiency results in delayed white matter development, ataxia and premature death in a novel mouse model. *Hum. Mol. Genet.* **29**, 1205–1217 (2020).
11. M. J. Ahrens, Y. Li, H. Jiang, A. T. Dudley, Convergent extension movements in growth plate chondrocytes require gpi-anchored cell surface proteins. *Development* **136**, 3463–3474 (2009).
12. V. Visconte et al., Phenotypic and functional characterization of a mouse model of targeted Pig-a deletion in hematopoietic cells. *Haematologica* **95**, 214–223 (2010).
13. M. Lukacs, T. Roberts, P. Chatuverdi, R. W. Stottmann, Glycosylphosphatidylinositol biosynthesis and remodeling are required for neural tube closure, heart development, and cranial neural crest cell survival. *eLife* **8**, 1–30 (2019).
14. D. M. McKean, L. Niswander, Defects in GPI biosynthesis perturb Cripto signaling during forebrain development in two new mouse models of holoprosencephaly. *Biol. Open* **1**, 874–883 (2012).
15. P. M. Krawitz et al., Identity-by-descent filtering of exome sequence data identifies PIGV mutations in hyperphosphatasia mental retardation syndrome. *Nat. Genet.* **42**, 827–829 (2010).
16. J. Y. Kang et al., PIG-V involved in transferring the second mannose in glycosylphosphatidylinositol. *J. Biol. Chem.* **280**, 9489–9497 (2005).
17. D. Horn, P. Krawitz, A. Mannhardt, G. C. Korenke, P. Meinecke, Hyperphosphatasia-mental retardation syndrome due to PIGV mutations: Expanded clinical spectrum. *Am. J. Med. Genet. A* **155A**, 1917–1922 (2011).
18. D. Horn et al., Delineation of PIGV mutation spectrum and associated phenotypes in hyperphosphatasia with mental retardation syndrome. *Eur. J. Hum. Genet.* **22**, 762–767 (2014).
19. A. Knaus et al., Characterization of glycosylphosphatidylinositol biosynthesis defects by clinical features, flow cytometry, and automated image analysis. *Genome Med.* **10**, 3 (2018).
20. T. Sakaguchi et al., A novel PGAP3 mutation in a Croatian boy with brachytelephalangy and a thin corpus callosum. *Hum. Genome Var.* **2018**, 18005 (2017).
21. P. Jirkof, Burrowing and nest building behavior as indicators of well-being in mice. *J. Neurosci. Methods* **234**, 139–146 (2014).
22. X. Yuan et al., A hypomorphic PIGA gene mutation causes severe defects in neuron development and susceptibility to complement-mediated toxicity in a human iPSC model. *PLoS One* **12**, e0174074 (2017).
23. K. M. J. van Loo et al., Calcium channel subunit α2δ4 is regulated by early growth response 1 and facilitates epileptogenesis. *J. Neurosci.* **39**, 3175–3187 (2019).
24. Daniele Matteiet al, Enzymatic Dissociation Induces Transcriptional and Proteotype Bias in Brain Cell Populations. *Int J Mol Sci* **21** (21), 10.3390/ijms21217944 (2020).
25. J. Y. Wang et al., Sun1 deficiency leads to cerebellar ataxia in mice. *Dis. Model. Mech.* **8**, 957–967 (2015).
26. M. Kojic et al., Elongator mutation in mice induces neurodegeneration and ataxia-like behavior. *Nat. Commun.* **9**, 3195 (2018).
27. A. V. Kalueff et al., Neurobiology of rodent self-grooming and its value for translational neuroscience. *Nat. Rev. Neurosci.* **17**, 45–59 (2016).
28. J. L. Silverman, M. Yang, C. Lord, J. N. Crawley, Behavioural phenotyping assays for mouse models of autism. *Nat. Rev. Neurosci.* **11**, 490–502 (2010).
29. D. Ledergerber, E. I. Moser, Memory retrieval: Taking the route via subiculum. *Curr. Biol.* **27**, R1225–R1227 (2017).
30. J. C. Hervé, N. Bourmeyster, Rho GTPases at the crossroad of signaling networks in mammals. *Small GTPases* **6**, 43–48 (2015).
31. M. Parri et al., EphrinA1 activates a Src/focal adhesion kinase-mediated motility response leading to rho-dependent actino/myosin contractility. *J. Biol. Chem.* **282**, 19619–19628 (2007).
32. B. Eisenhaber, P. Bork, F. Eisenhaber, Post-translational GPI lipid anchor modification of proteins in kingdoms of life: Analysis of protein sequence data from complete genomes. *Protein Eng.* **14**, 17–25 (2001).
33. R. J. Kelly et al., Long-term treatment with eculizumab in paroxysmal nocturnal hemoglobinuria: Sustained efficacy and improved survival. *Blood* **117**, 6786–6792 (2011).
34. D. Szklarczyk et al., STRING v10: Protein-protein interaction networks, integrated over the tree of life. *Nucleic Acids Res.* **43**, D447–D452 (2015).
35. L. K. Harbott, C. D. Nobes, A key role for Abl family kinases in EphA receptor-mediated growth cone collapse. *Mol. Cell. Neurosci.* **30**, 1–11 (2005).
36. L. Tuomisto, V. Lozeva, A. Valjakka, A. Lecklin, Modifying effects of histamine on circadian rhythms and neuronal excitability. *Behav. Brain Res.* **124**, 129–135 (2001).
37. M. M. Thakkar, Histamine in the regulation of wakefulness. *Sleep Med. Rev.* **15**, 65–74 (2011).
38. Y. Urade, O. Hayaishi, Prostaglandin D2 and sleep/wake regulation. *Sleep Med. Rev.* **15**, 411–418 (2011).
39. A. Ram et al., CSF levels of prostaglandins, especially the level of prostaglandin D2, are correlated with increasing propensity towards sleep in rats. *Brain Res.* **751**, 81–89 (1997).
40. G. S. Eakin, A. Hadjantonakis, Production of chimeras by aggregation of embryonic stem cells with diploid or tetraploid mouse embryos. *Nat. Protoc.* **1**, 1145–1153 (2006).
41. R Core Team, R: A Language and Environment for Statistical Computing (R Foundation for Statistical Computing, Vienna, Austria, 2019). https://www.R-project.org/.

Rodríguez de los Santos et al.
A CRISPR-Cas9–engineered mouse model for GPI-anchor deficiency mirrors human phenotypes and exhibits hippocampal synaptic dysfunctions

PNAS | 11 of 11
https://doi.org/10.1073/pnas.2014481118

37

NEUROSCIENCE

## Supplementary Figure 1



**Experimental design**

**A** pX459 Vector + ssODN
Fugene | lipofection

**B** pX459-Addgene

**C** ssODN design

**D** Genotyping

**E** Flow cytometry analysis mES clones

**F** Weight curve - female

**Generation of the mouse model, analysis of mES clones and weight curve.** (A) Schematic overview of the experimental design from generating the mouse embryonic stem (mES) cell clone to establishment of the mouse model. (B) Schematic overview of the pX459 vector from Addgene. (C) single-stranded oligode-oxynucleotides (ssODNs) were designed with asymmetrical homology arms (HA), highlighted in grey and with phosphorothioate (PS) bonds according to Renaud et al. (2016), Richardson et al. (2016). ssODNs were identical to the target strand. Single-guide RNA (sgRNA) is highlighted in blue. Protospacer adjacent motif (PAM) is marked in red (D) ssODNs contained the nucleotide T (marked in pink) causing the missense mutation c.1022 C>A on the complementary strand and three additional silent mutations (marked in red and blue) that avoid a second cut by Cas9 after homology-directed repair (HDR) has happened. The silent mutation marked in blue generated a restriction site for *BcuI* that was used for genotyping purposes. Sanger sequencing of homozygous *Pigv*[341E] knock-in clone revealed the stable integration of missense mutation (on the (-) strand C>A, on the (+) strand G>T, causing PIGV p.Ala341Glu) and silent mutations (on the (+) strand C>T, A>G, C>T) at CRISPR-Cas9-induced DSB by HDR. Gel electrophoresis identified genotypes in mice by *BcuI* digest of PCR-amplified products using the primers m*Pigv*_Ex4_fw and m*Pigv*_Ex4_rv. RS: Reference sequence of *Pigv* (E) Flow cytometry analysis of CRISPR-engineered mouse embryonic stem cell (mES) clones: homozygous *Pigv*[341E] (hom-*Pigv*[341E]), homozygous *Pgap3*[107L] (hom-*Pgap3*[107L]) +/+, homozygous *Pigv* knock-out (*Pigv* -/-) revealed decreased expression in FLAER and GPI-linked CD90 as compared to wildtype (wt), MFI: Mean fluorescence intensity. (F) Female *Pigv*[341E] mice reveal a reduced weight from postnatal day (P) 1 to 21. Animals used for the weight curve: Wt(female n=4) *Pigv*[341E](female n= 3). The data from the weight curve was analyzed by two-way of variance (ANOVA) followed by a Bonferroni's multiple comparisons test. *P<0.05, **P<0.01, ***P<0.001.

# Supplementary Figure 2

## A  HCS - total occurrences of behavior ⊞ Wt ⊞ *Pigv*[341E]



## B  HCS - total duration of behavior ⊞ Wt ⊞ *Pigv*[341E]



## C  SAM - Mean distance traveled per day - mixed ⊞ Wt ⊞ *Pigv*[341E]



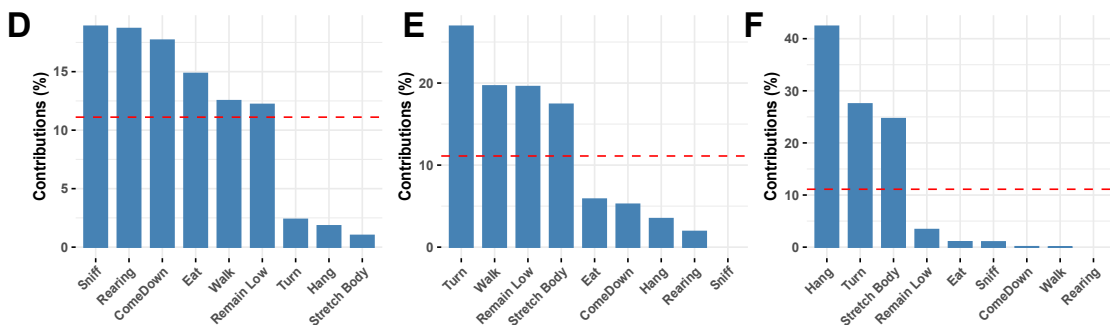## D  SAM - mean distance traveled per hour - mixed ── Wt ── *Pigv*[341E]
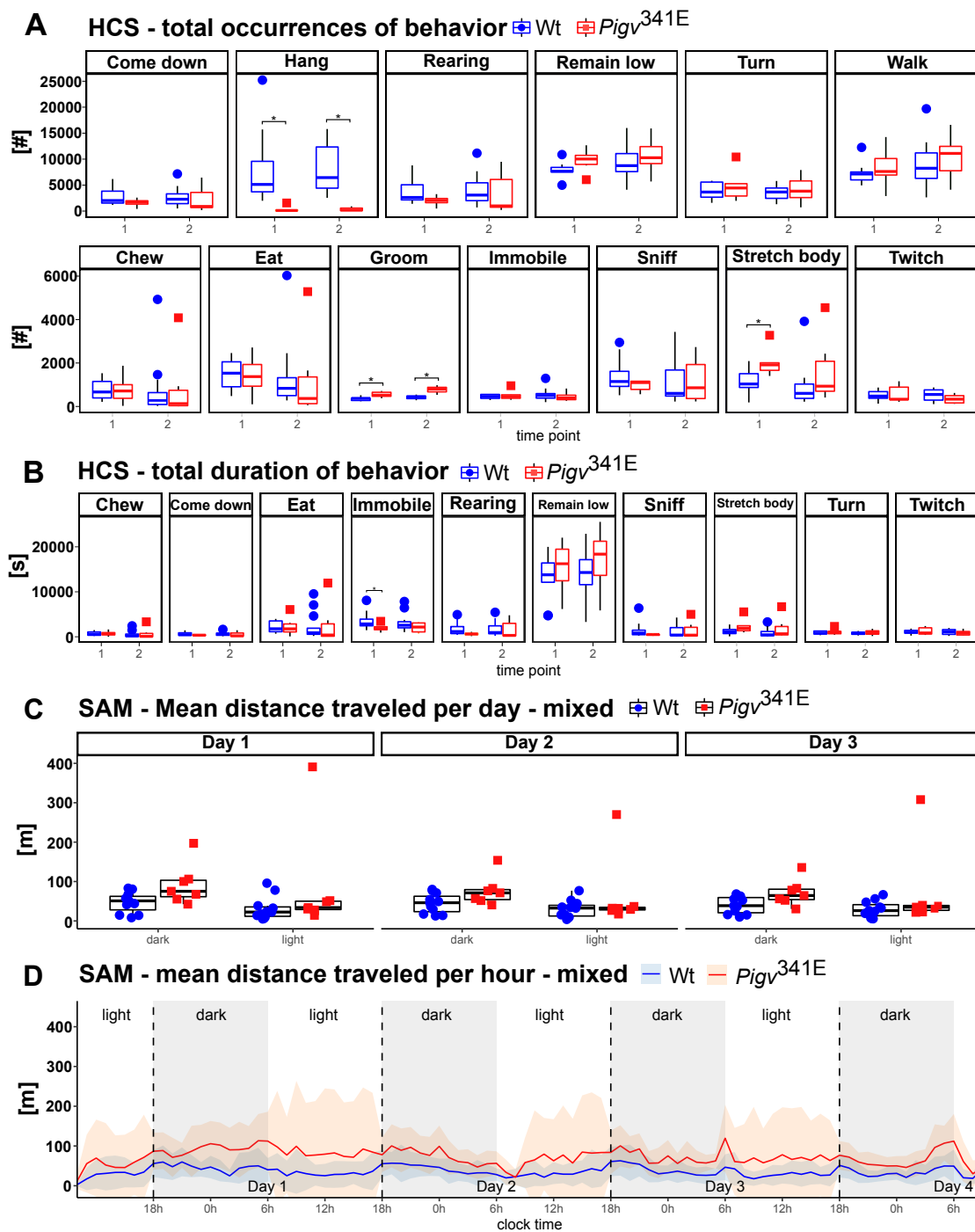


**HCS and SAM (second approach)** (A) Total occurrences of behaviors from the home cage scan (HCS). *Pigv*[341E] mice revealed a decreased number of hanging and an increased number of grooming at both time points. *Pigv*[341E] mice showed an increased number of "stretch body" at time point 1. (B) Total duration of behavior of behaviors from the HCS. *Pigv*[341E] mice showed a decreased "immobile" behavior at time point 1. (C, D) In the social activity monitor (SAM), no significant differences in mean distance traveled per day and per hour were observed between genotypes when held in mixed genotypes. *Pigv*[341E]=homozygous for Pigv p.Ala341Glu, wt=wild-type. Animals used for the HCS were at time point 1 (tp1) 8 weeks old, at time point 2 (tp2) 16 weeks old: Wt(female n=8, male n=4) *Pigv*[341E](female n= 4, male n=2). Animals used for SAM: Wt(female n=4, male n=6) *Pigv*[341E](female n= 2, male n=5). The data from the HCS (total occurrences, total duration) was analyzed with Wilcoxon rank sum test (non parametric). The data from the SAM (distance traveled per hour) was analyzed with generalized linear mixed-effects models (glmm) using a Markov chain Monte Carlo (MCMC).*P<0.05.

**Supplementary Figure 3**



**HCS (Home cage scan) – principal component analysis (PCA).** (A-F) contribution of original variables (occurrences of behavior) to the first three components of the PCA for each time point. (G-L) 2D Representation of the coefficient of all variables along PC1 and PC2 (left), PC1 and PC3 (middle) and PC2 and PC3 (right) for each time point.

**Supplementary Figure 4**
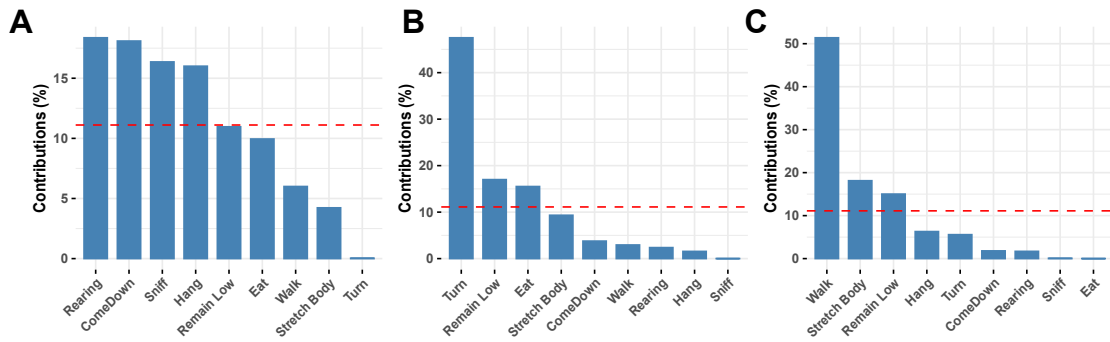


**Home cage scan - PCA - time point 1**

**Home cage scan - PCA - time point 2**
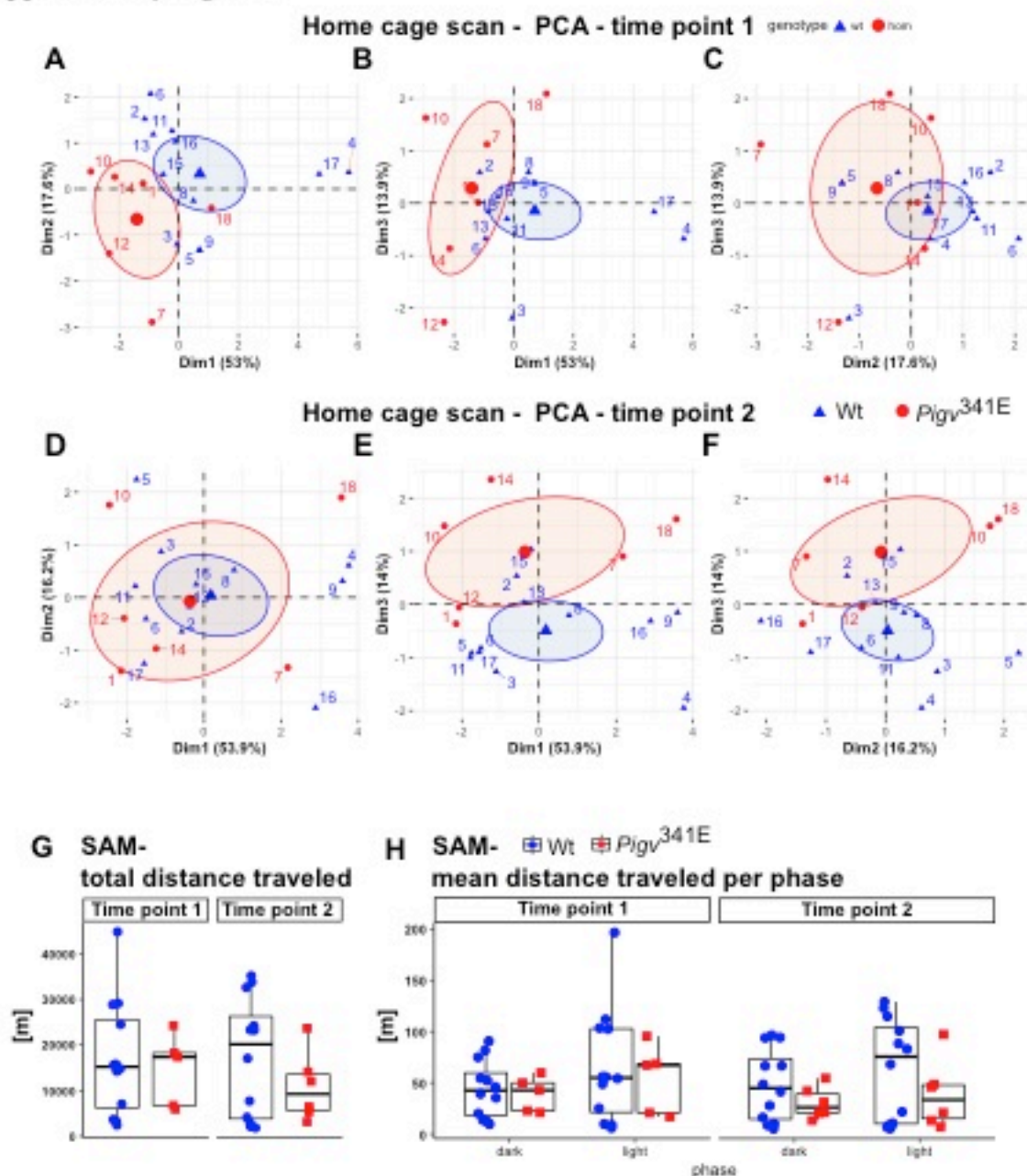
**HCS (Home cage scan) – principal component analysis (PCA), SAM (first approach).** (A-F) Group separation and individual contribution to PC1 and PC2 (left), PC1 and PC3 (middle) and PC2 and PC3 (right). Mean (bigger symbol) and confidence interval (ellipse) of each group are shown. Genotypes differ significantly in dimension 1 at time point 1 and in dimension 3 in time point 2 (G-H) Social activity monitor (SAM) showed no significant differences in total distance traveled and distance traveled per phase between genotypes when held in mixed genotypes.

$Pigv^{341E}$=homozygous for Pigv p.Ala341Glu, wt=wild-type. Animals used for the HCS were at time point 1 (tp1) 8 weeks old, at time point 2 (tp2) 16 weeks old: Wt(female n=8, male n=4) $Pigv^{341E}$(female n= 4, male n=2).Animals used for the SAM were at time point 1 (tp1) 9 weeks old: Wt(female n=8, male n=4), $Pigv^{341E}$(female n= 3, male n=2). Animals were at time point 2 (tp2) 17 weeks old: Wt(female n=8, male n=4), $Pigv^{341E}$(female n= 4, male n=2). Data from PCA and SAM (total distance traveled, mean distance traveled per phase) was analyzed with a Wilcoxon rank sum test. *P<0.05, **P<0.01, ***<P0.001.

**Supplementary Figure 5**



**A** SAM - mean distance traveled per hour - mixed - tp 1 — Wt — *Pigv*[341E]

**B** SAM - mean distance traveled per phase - mixed - tp 1 — Wt — *Pigv*[341E]

**C** SAM - mean distance traveled per hour - mixed - tp 2 — Wt — *Pigv*[341E]

**D** SAM - mean distance traveled per phase - mixed - tp 2 — Wt — *Pigv*[341E]
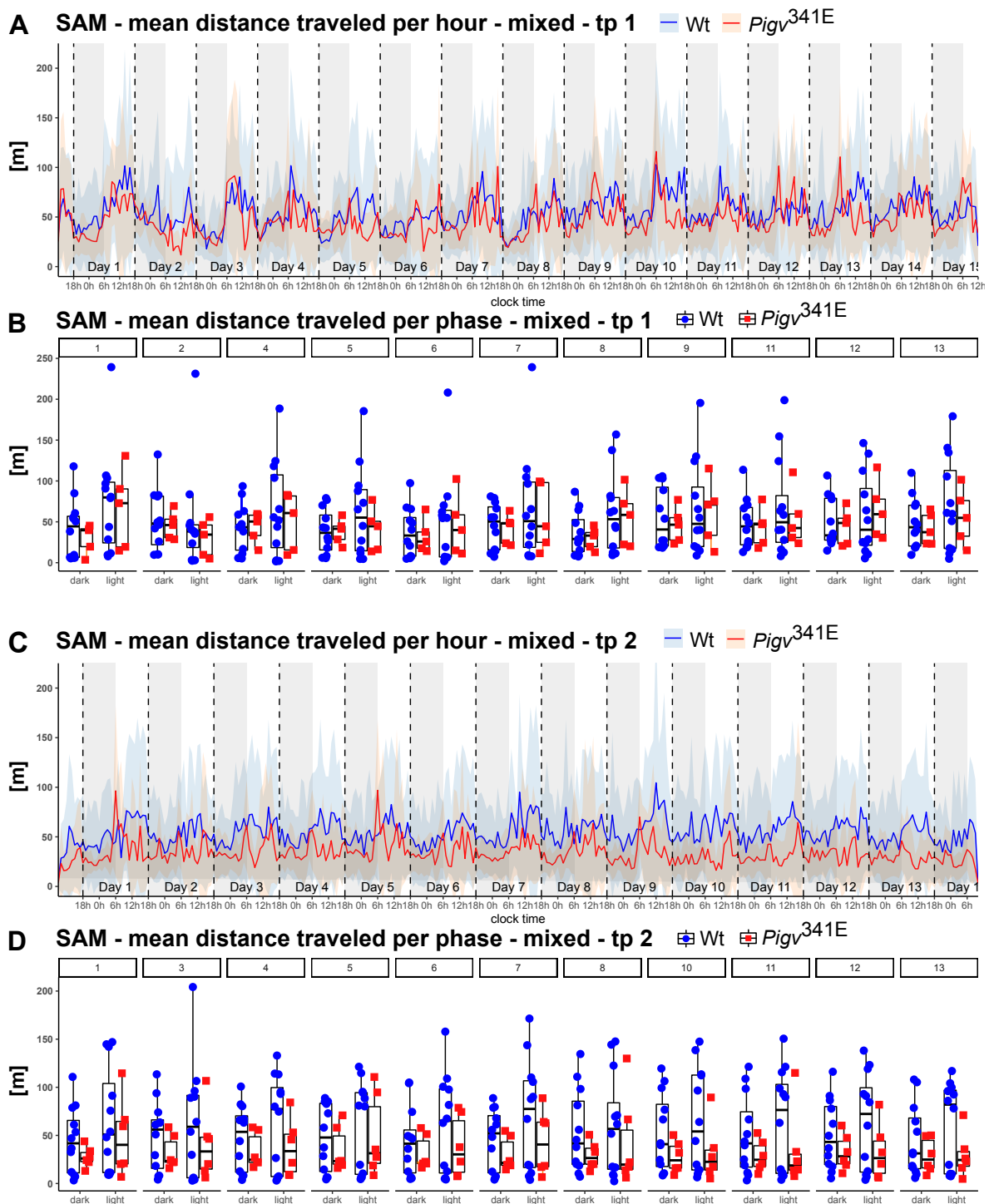
**SAM (first approach).** (A, C) In the social activity monitor (SAM), no significant differences were observed in distance traveled per hour at both time points between genotypes when animals were held in mixed genotypes. Both genotypes were significantly more active during the light cycle than during the dark cycle at both time points. (B, D) No significant differences were observed in distance traveled per phase at both time points between genotypes when animals were held in mixed genotypes. *Pigv*[341E]=homozygous for Pigv p.Ala341Glu, wt=wild-type. Animals used for the SAM were at time point 1 (tp1) 9 weeks old: Wt(female n=8, male n=4), *Pigv*[341E](female n= 3, male n=2). At time point 2 (tp2) animals were 17 weeks old: Wt(female n=8, male n=4), *Pigv*[341E](female n= 4, male n=2). Data from the SAM (mean distance per hour) was analyzed with a generalized linear mixed-effects models (glmm) using a Markov chain Monte Carlo (MCMC). *P<0.05, **P<0.01, ***P<0.001.

# Supplementary Figure 6
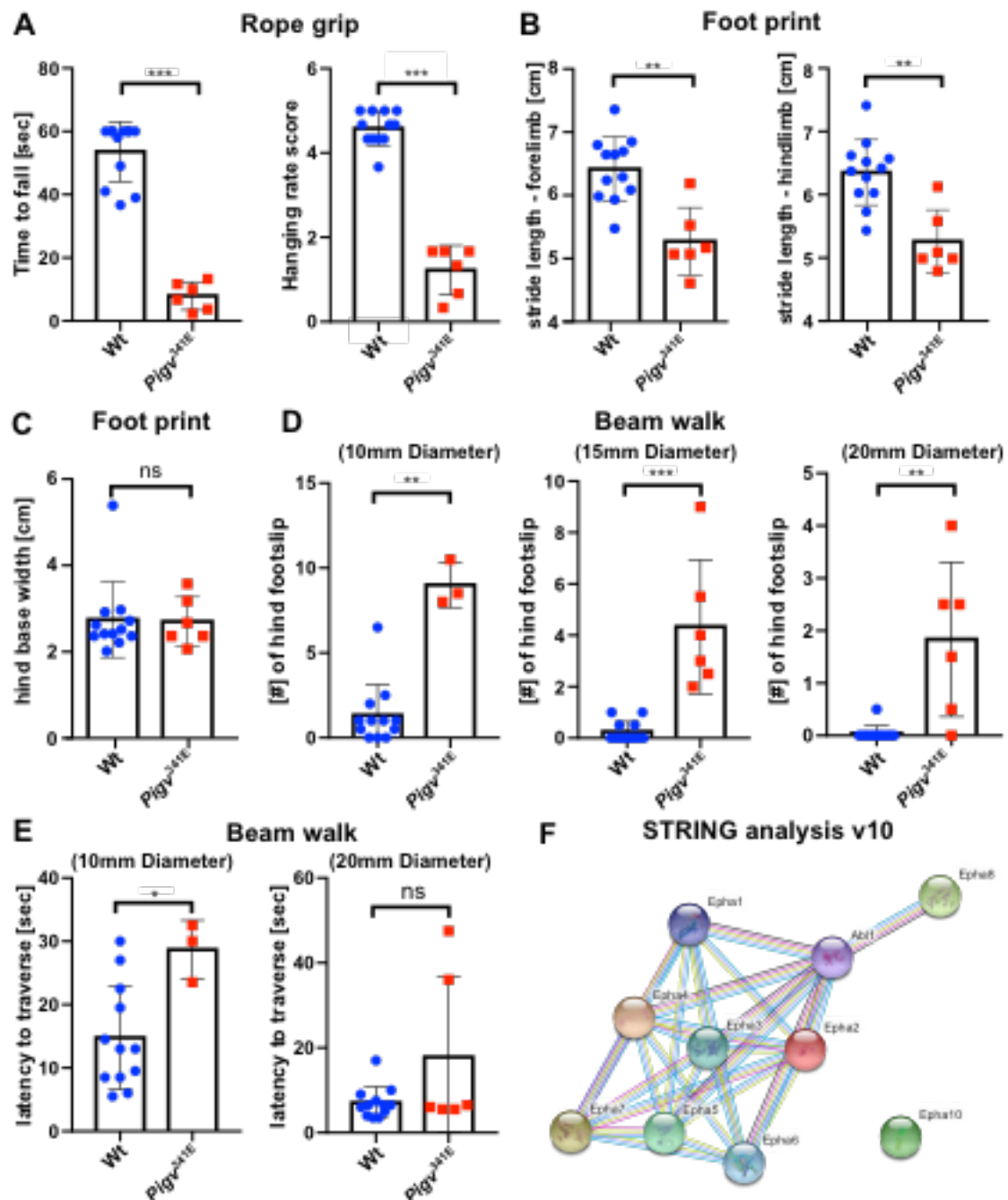


***Pigv***[341E] **mice show a motoric phenotype and STRING analysis** (A) In the rope grip test, *Pigv*[341E] mice showed a decreased climbing performance displayed by a decreased time to fall off the rope (left graph) and a decreased hanging score (right graph). (B,C) In the foot print test, *Pigv*[341E] mice exhibited no significant differences to wild-type in hind base width but showed a decreased forelimb and hindlimb stride length (FL-SL, HL-SL). (D) *Pigv*[341E] mice had deficits in motor coordination displayed by an increased number of hind footslip when walking on beams with different diameters (10-20 mm diameter). (E) *Pigv*[341E] mice showed an increased latency to traverse a beam with a diameter of 10 mm (left graph) but revealed no significant difference to wild-type mice traversing a beam of 20 mm (right graph). (F) STRING analysis v10 confirmed protein-protein interaction between EphA-receptors and Abl1. Turquoise string: from curated databases, pink string: experimentally determined, yellow string: textmining, black string: co-expression, lila string: protein homology.
*Pigv*[341E]=homozygous for Pigv p.Ala341Glu, wt=wild-type. Wt(female n=8, male n=4), *Pigv*[341E] (female n= 4, male n=2). Animals were 7 weeks old. The data was analyzed with a non-parametric t-test (Mann-Whitney). *$P<0.05$, **$P<0.01$, ***$P<0.001$

# Supplementary Figure 7
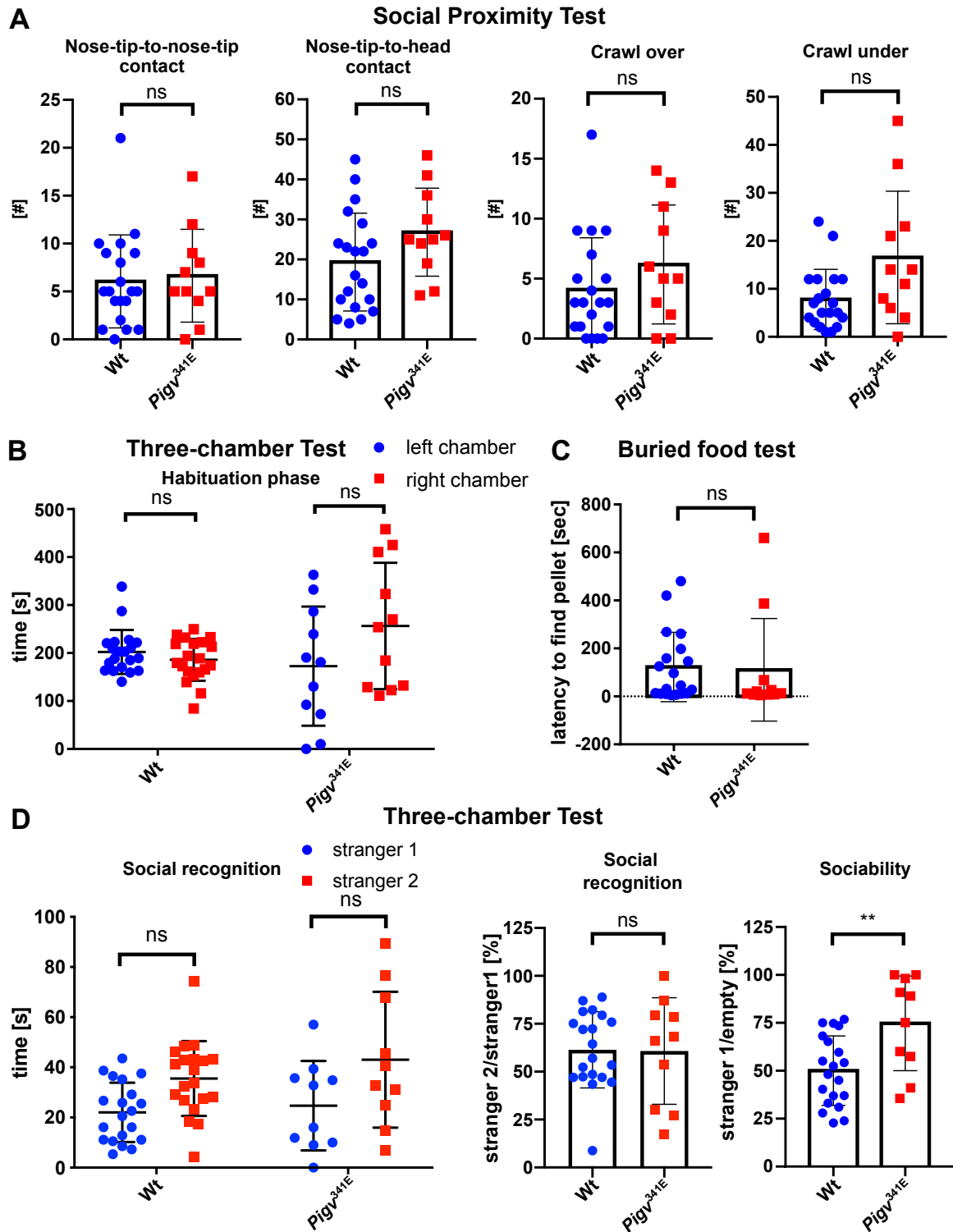


**Pigv^{341E} mice exhibit a social phenotype and no defects in olfaction** (A) In the social proximity test, *Pigv*^341E mice revealed no significant differences to wild-type in numbers of nose-tip-to-nose-tip, nose-tip-to-head contact, "crawl over" and "crawl under" behavior when interacting with the stranger mouse. (B) During the habituation phase *Pigv*^341E and wild-type mice did not show any preferences for the left and right chamber. (C) In the buried food test, no differences were observed in olfaction between genotypes. (D) *Pigv*^341E mice showed no significant difference in spending time with stranger 1 and 2 in the three-chamber test (first 5 minutes) (left graph) as wild-type mice. Furthermore, ratio between stranger 2 and 1 (middle graph) did not show any differences between genotypes in the three-chamber test (first 5 minutes). The ratio between stranger 1 and empty cage was increased (right

graph) in $Pigv^{341E}$ mice indicating an enhanced social approach behavior in the three-chamber test (first 5 minutes). $Pigv^{341E}$=homozygous for Pigv p.Ala341Glu, wt=wild-type. Animals used for the three-chamber test: Wt(female n=9, male n=11), $Pigv^{341E}$(female n=4, male n=6). Animals used for the social proximity test and buried food test: Wt(female n=9, male n=11), $Pigv^{341E}$(female n=4, male n=7). Stranger mice had the same age and sex as testing mice. The data from the social proximity test, three-chamber test (ratio strainger2/1, stranger1/empty) and buried food test was analyzed by a non-parametric t-test (Mann-Whitney). The data from the three-chamber test (habituation phase, social recognition) was analyzed by two-way of variance (ANOVA) followed by a Bonferroni's multiple comparisons test. *P<0.05, **P<0.01, ***P<0.001.
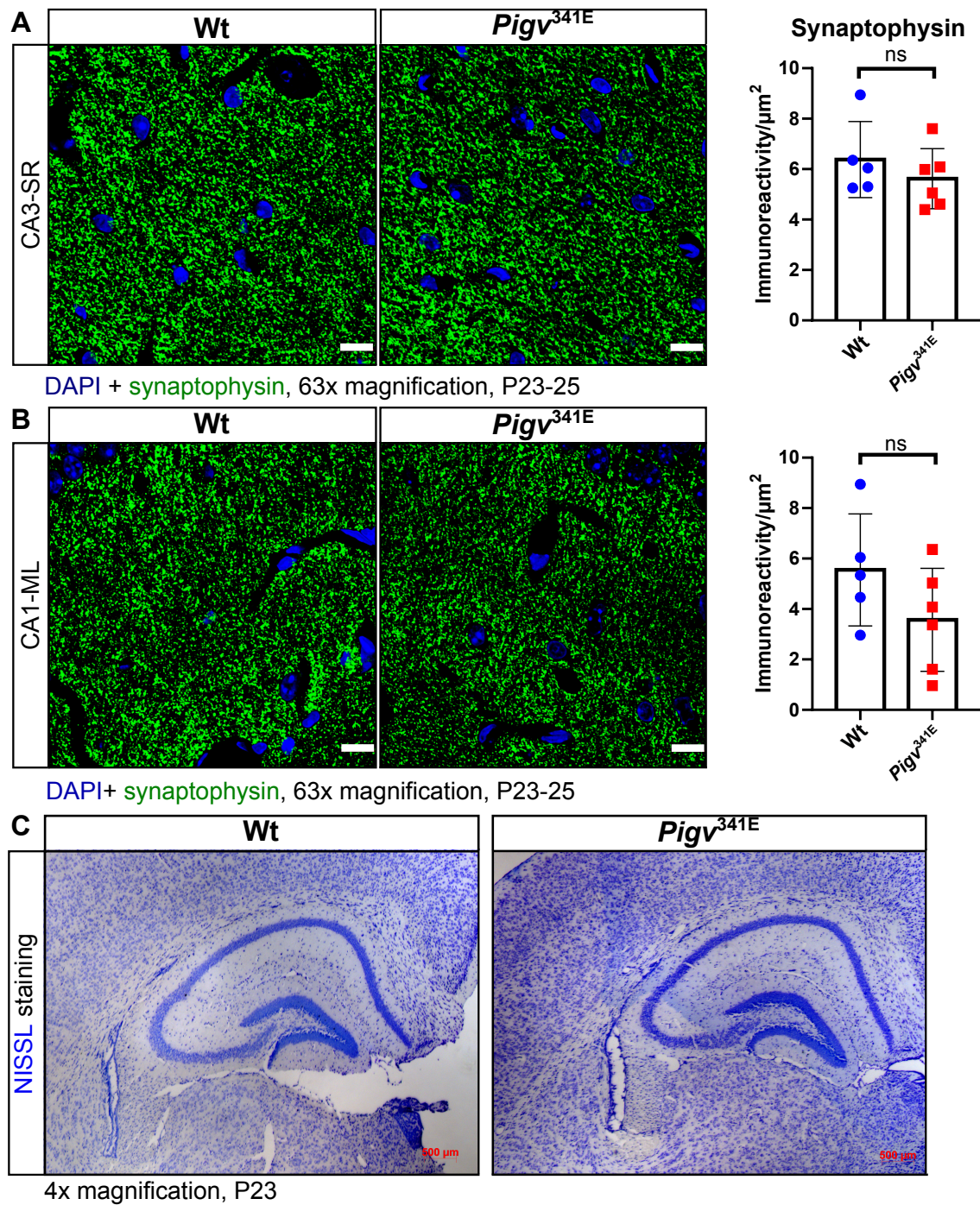
**Supplementary Figure 8**



**A**  Y-Maze

**B**  Barnes maze
Target area-day 5   Target area-day 12

**C**  Barnes maze-wrong holes

**D**  Barnes maze-search strategy
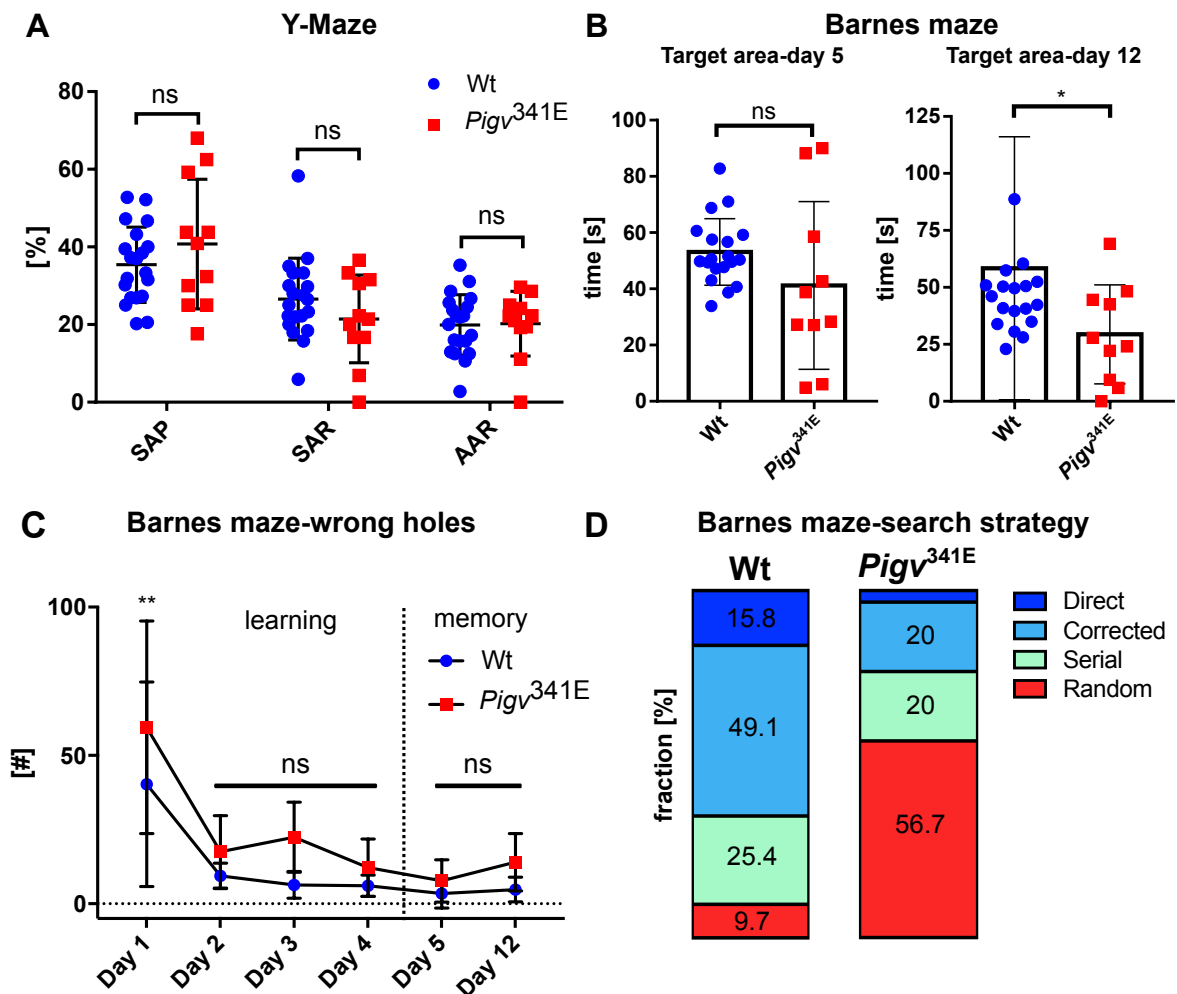
$Pigv^{341E}$ **mice show cognitive deficits in spatial memory.** (A) In the y-maze, $Pigv^{341E}$ mice showed no alterations in spontaneous alternation performance (SAP), same arm returns (SAR) and alternate arm returns (AAR) and thus are not impaired in short-term working memory. (B) $Pigv^{341E}$ mice spent less time in the target quadrant of the Barnes maze at day 12 (long-term memory). At day 5 (short-term memory) there was no significant difference between genotypes. (C) In the Barnes maze, $Pigv^{341E}$ mice showed no significant differences in the number of wrong holes to wild-type during day 2-12. (D) Fractions of search strategies during the Barnes maze test that $Pigv^{341E}$ mice and wild-type used in order to find the correct exit hole were shifted in $Pigv^{341E}$ mice. Direct=direct way to the correct exit hole, corrected=mice targeted first 1-3 wrong holes and went afterwards directly to the correct hole, serial=mice checked all holes in series, random=mice targeted random holes without any order.
$Pigv^{341E}$=homozygous for Pigv p.Ala341Glu, wt=wild-type. Animals used for the y-maze: Wt(female n=9, male n=11), $Pigv^{341E}$(female n=4, male n=7). Animals used for the Barnes maze: Wt(female n=8, male n=11) $Pigv^{341E}$(female n=4, male n=6). The data from the y-maze and the barnes maze (target area day 5 and 12) was analyzed with a non-parametric t-test (Mann-Whitney). The data from the Barnes maze (number of wrong holes) was analyzed by two-way of variance (ANOVA) followed by a Bonferroni's multiple comparisons test. *P<0.05 **P<0.01, ***P<0.001.

**Supplementary Figure 9**
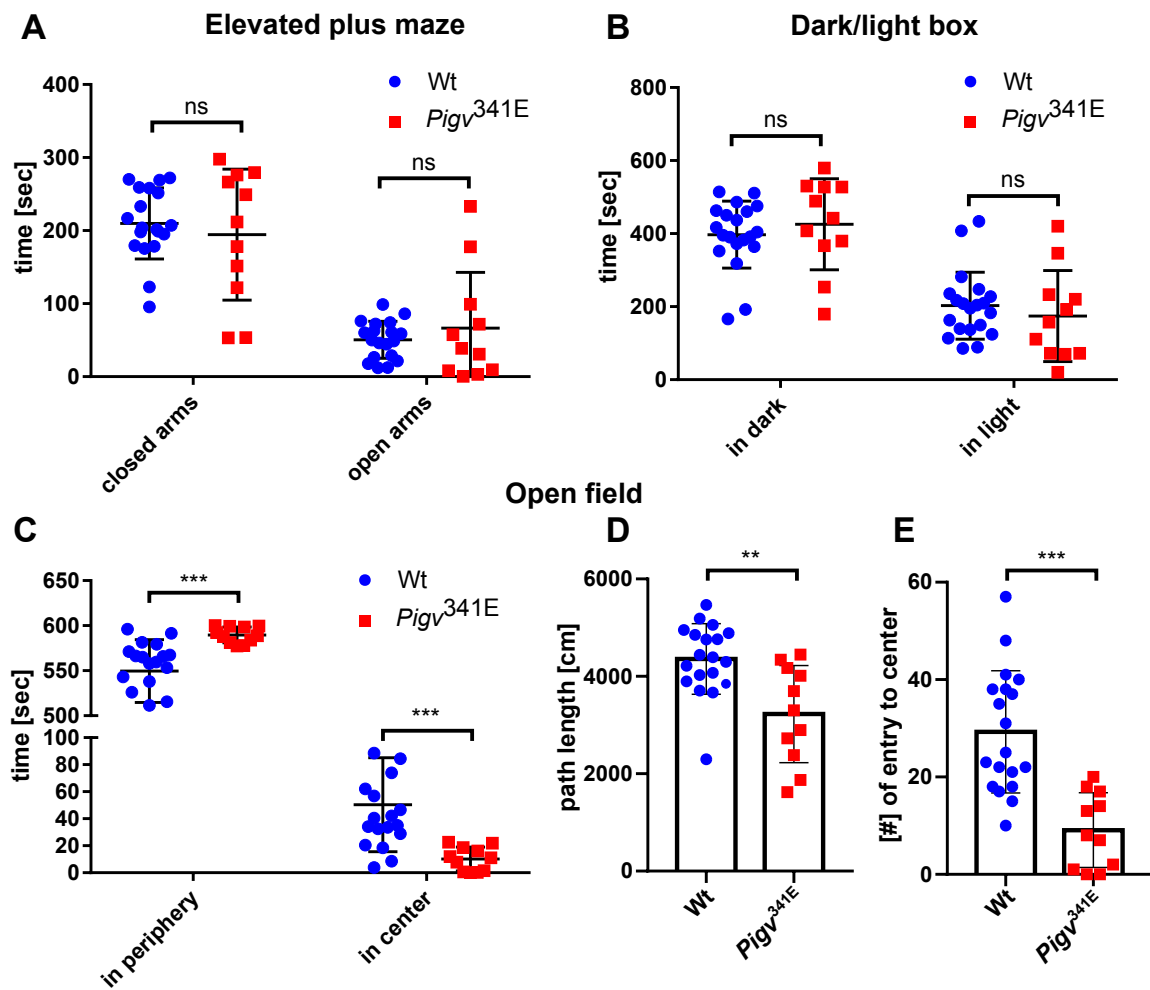


**Affective behavior of *Pigv*[341E] mice.** (A) In the elevated plus maze, *Pigv*[341E] mice showed no significant difference to wild-type in exploration behavior displayed by spending the same time in the open and closed arms. (B) In the dark/light box, *Pigv*[341E] mice exhibited no significant difference to wild-type in exploring the dark and light compartment. (C) In the open field test, *Pigv*[341E] mice spent more time in the periphery than in the center. (D) *Pigv*[341E] mice showed a reduced distance traveled in the open field displayed by a reduced path length. (E) *Pigv*[341E] mice visited less time the center of the open field.
*Pigv*[341E]=homozygous for Pigv p.Ala341Glu, wt=wild-type. Animals used for the open field, elevated plus maze, dark/light box: Wt(female n=9, male n=11) *Pigv*[341E] (female n=4, male n=7). The data from the open field, elevated plus maze, dark/light box was analyzed with a non-parametric t-test (Mann-Whitney). *P<0.05 **P<0.01, ***P<0.001.

**Supplementary Figure 10**



DAPI + synaptophysin, 63x magnification, P23-25



DAPI+ synaptophysin, 63x magnification, P23-25



4x magnification, P23

*Pigv*[341E] **mice show no morphological abnormalities in the hippocampus** (A-B) Representative image of immunoflourenscence staining showed no difference in synaptophysin immunoreactivity (green) in *Cornu Ammonis* 3 - *Stratum Radiatum* (CA3-SR) and *Cornu Ammonis* 1 – molecular layer of dentate gyrus (CA1-ML) between genotypes (left). 4′,6-Diamidin-2-phenylindol (DAPI) (blue). Images were taken at 63x magnification, scale=10 μm. Synaptophysin immunoreactivity were quantified with Fiji ImageJ and revealed no significantly reduced immunoreactivity/μm$^2$ in CA3-SR and CA1-ML between genotypes (right). Animals were 3 weeks old: Wt(female n=3, male n=2) *Pigv*[341E](female n=2, male n=4). (C) Representative images of a Nissl staining revealed no morphological abnormalities in the hippocampus between genotypes. 4x magnification, scale=500 μm. The data from the synaptophysin immunofluorescence staining was analyzed with a parametric student t-test. *P<0.05 **P<0.01, ***P<0.001.

48

**Supplementary Figure 11**
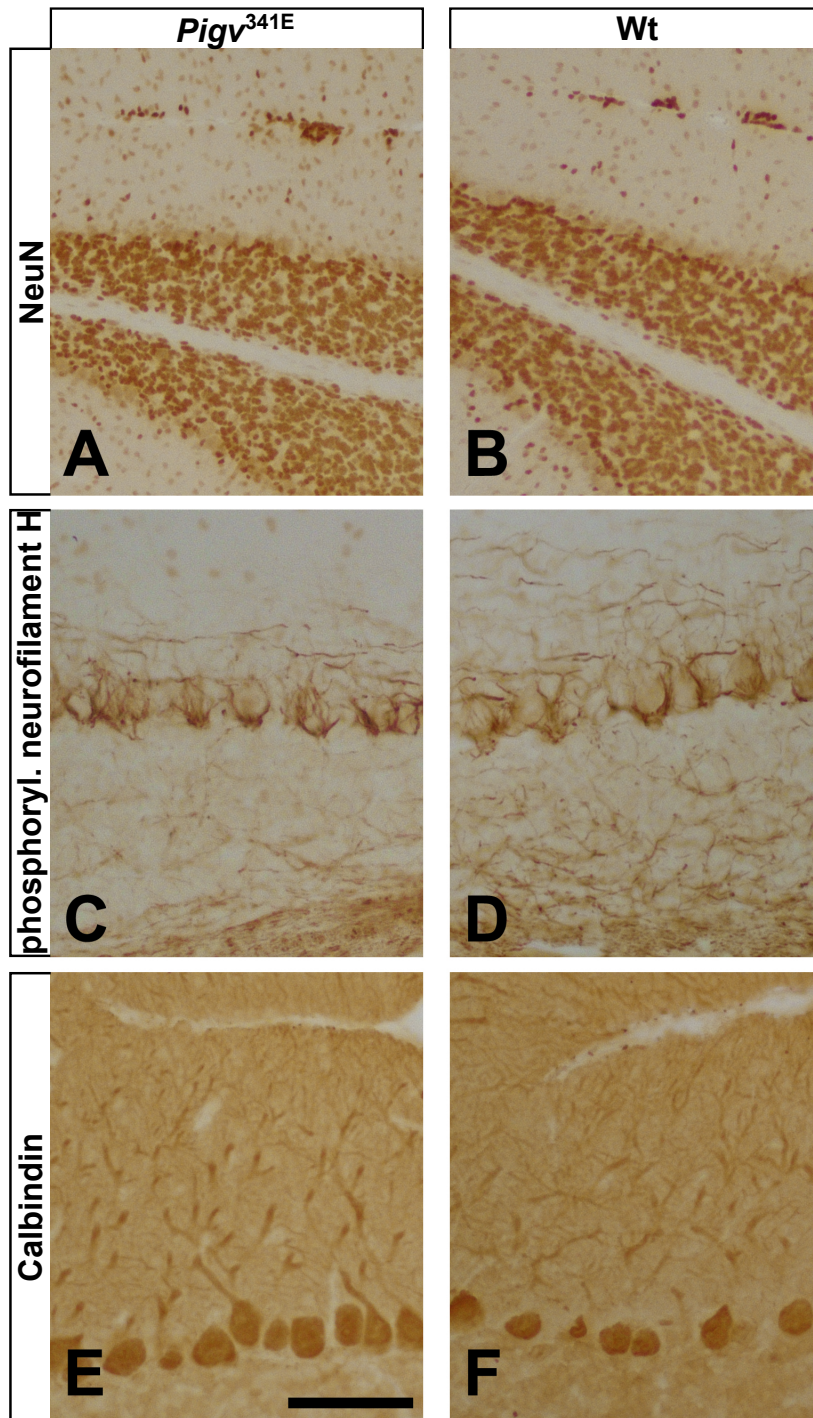


***Pigv*<sup>341E</sup> mice show no morphological abnormalities in the cerebellum** (A-B) Representative image of immuno-3,3′-Diaminobenzidin (DAB) staining showed no changes of labels granule cells in the granule cell layer (shown are the granule cell layers from lobule 8) between genotypes. A few scattered cells were observed in the molecular layer, and small granule cell ectopias in the meninges separating lobules 8 and 7 (at the top of the panels). Such ectopias are common in C57bl mice, as used here, and no differences in the position or extent of these ectopias could be detected for wild type and Pigv[341E] mice. (C-D) Phosphorylated neurofilament H outlines axons of basket and stellate cells that converge from the molecular layer (top of the panels) to form the name-giving axonal basket around Purkinje cell perikarya. No differences were observed between genotypes. (E-F) Staining for calbindin D28k reveals regularly arranged. Bar (in panel E) = 80 μm for panels A and B, and 40 μm for panels C-F. Animals were 3 weeks old.

**Supplementary Figure 12**
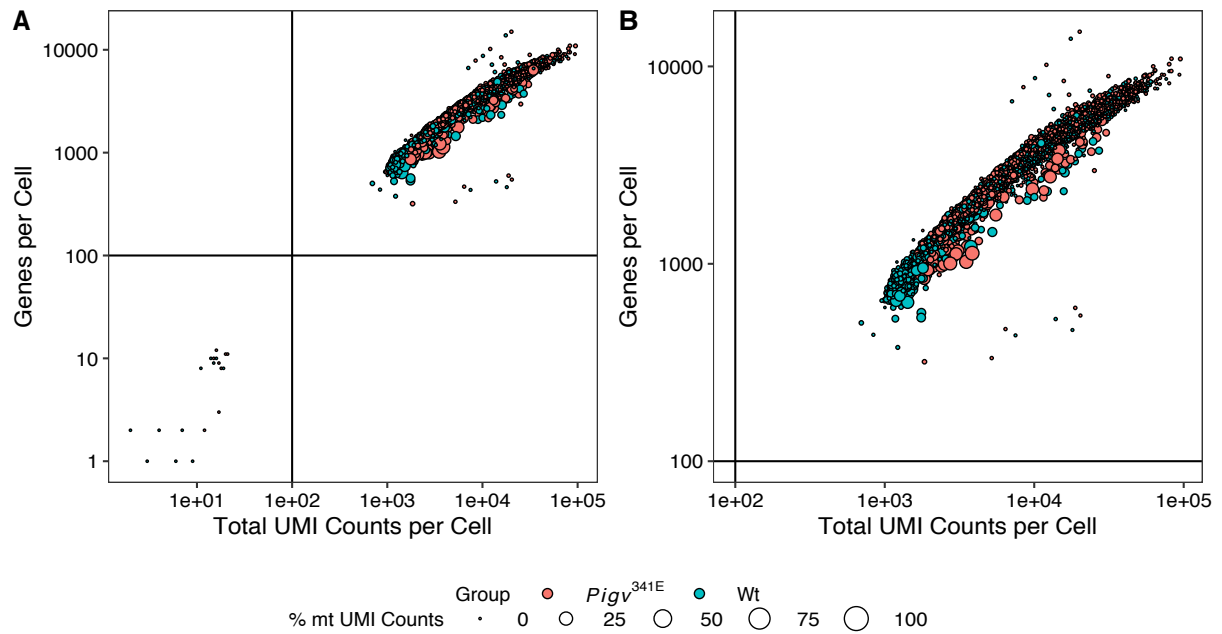


**Filtering removes outlying barcodes.** Keeping only cellular barcodes with more than 100 genes per cell, more than 100 UMI counts per cell and less than 30 % UMI counts mapping to mitochondrial genes from the full preprocessed data set comprising 15,949 barcodes (A) removes 19 outlying barcodes, resulting in the filtered data set comprising 15,930 barcodes (B).

## Supplementary Figure 13
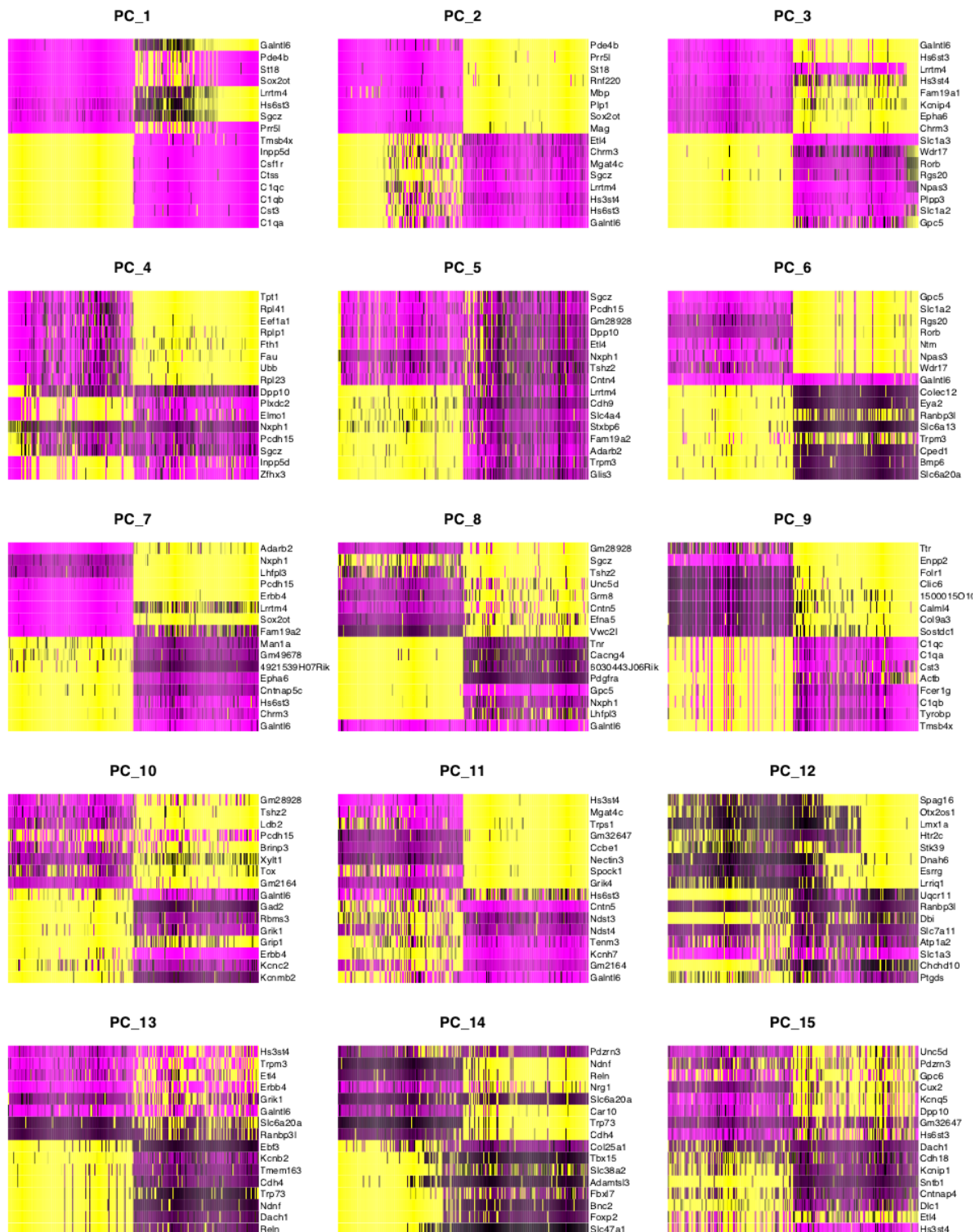


**Dimensional reduction heat maps.** Heat maps on the 15 most influential genes and 250 cells sorted by principal component score for each of the first 15 principal components support the selection of the top 11 principal components for further non-parametric dimensionality reduction and downstream analysis.

**Supplementary Figure 14**
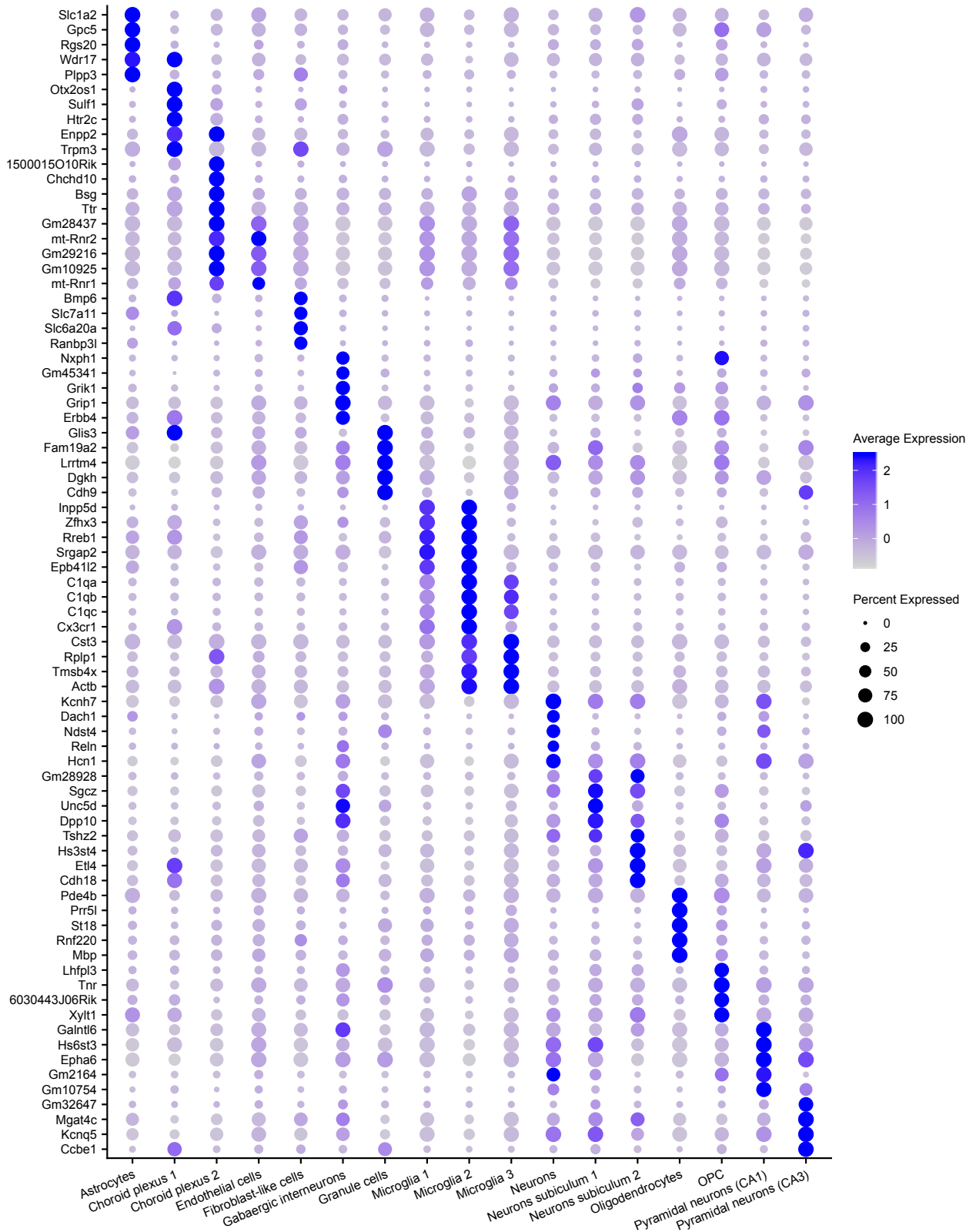


**Expression of marker genes in cellular subgroups.** For each of the 17 cellular subgroups, the 5 differentially expressed genes with highest average fold change in comparison to all remaining cells are depicted. The dot size represents the percentage of cells within a cluster with non-zero expression of the respective gene.

**Supplementary Figure 15**
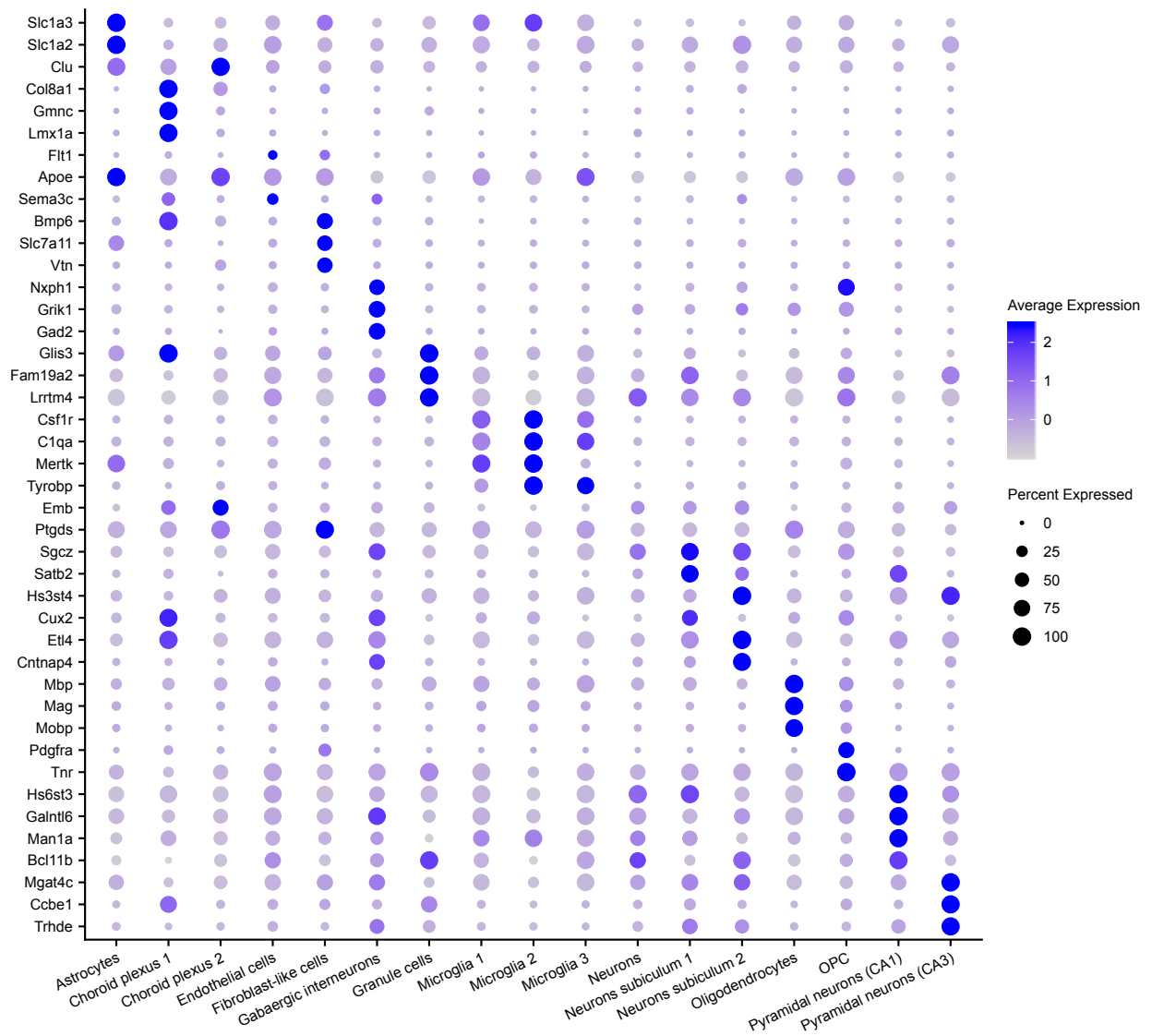


**Expression of selected genes in cellular subgroups.** For each of the 17 cellular subgroups, the average expression of selected genes that supported assignment of cellular subgroup identities are depicted. The dot size represents the percentage of cells within a cluster with non-zero expression of the respective gene.

**Supplementary Figure 16**
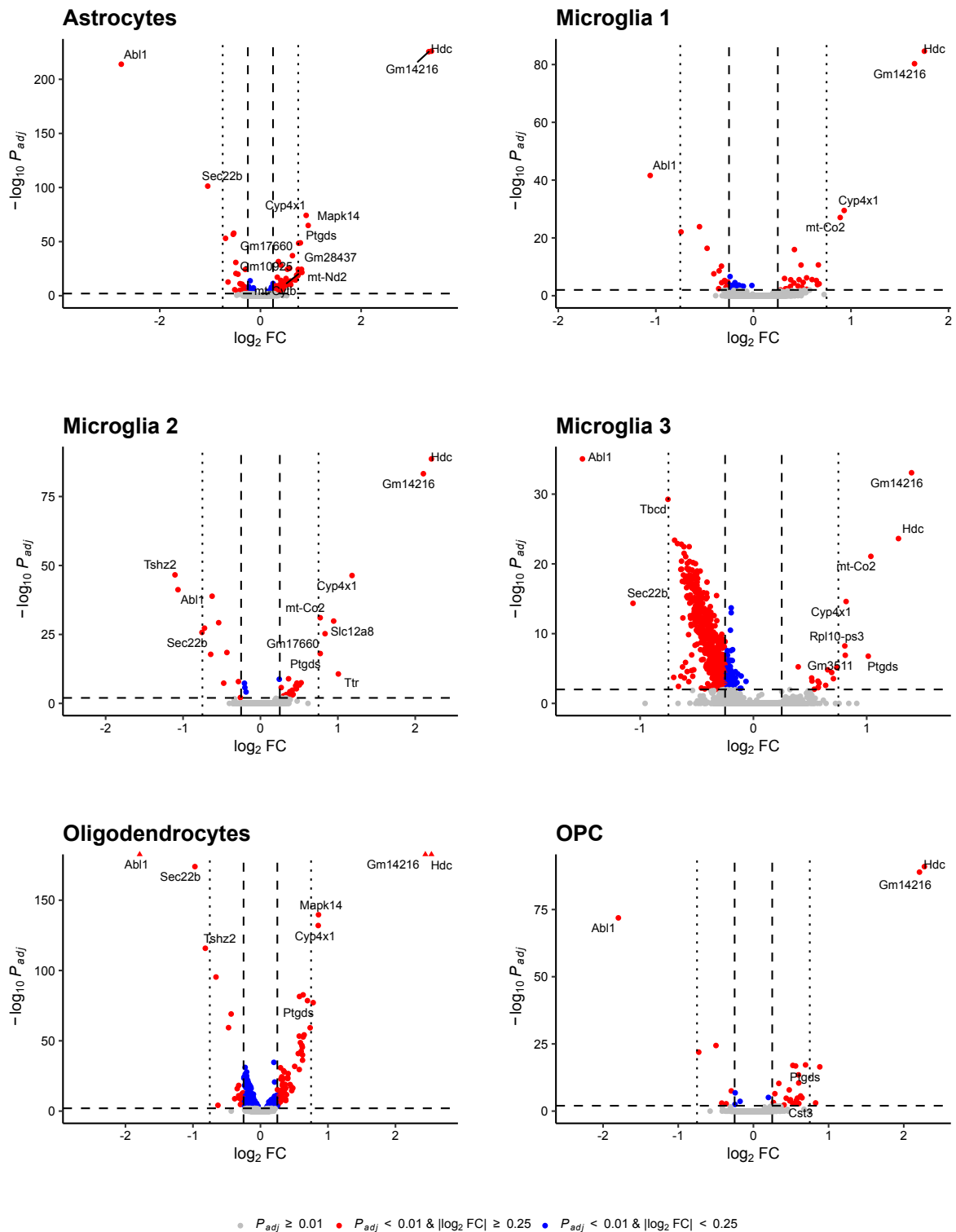


**Volcano plots resulting from comparison of *Pigv*[341E] cells and wild-type cells within glial cellular subgroups.** Dashed horizontal lines are located at an adjusted p-value of 0.01, dashed vertical lines at an absolute $\log_2$ fold change of 0.25 and dotted vertical lines at an absolute $\log_2$ fold change of 0.75. For genes with an adjusted p-value below 0.01 and a minimum absolute $\log_2$ fold change of 0.75, gene symbols are depicted.

54

**Supplementary Figure 17**
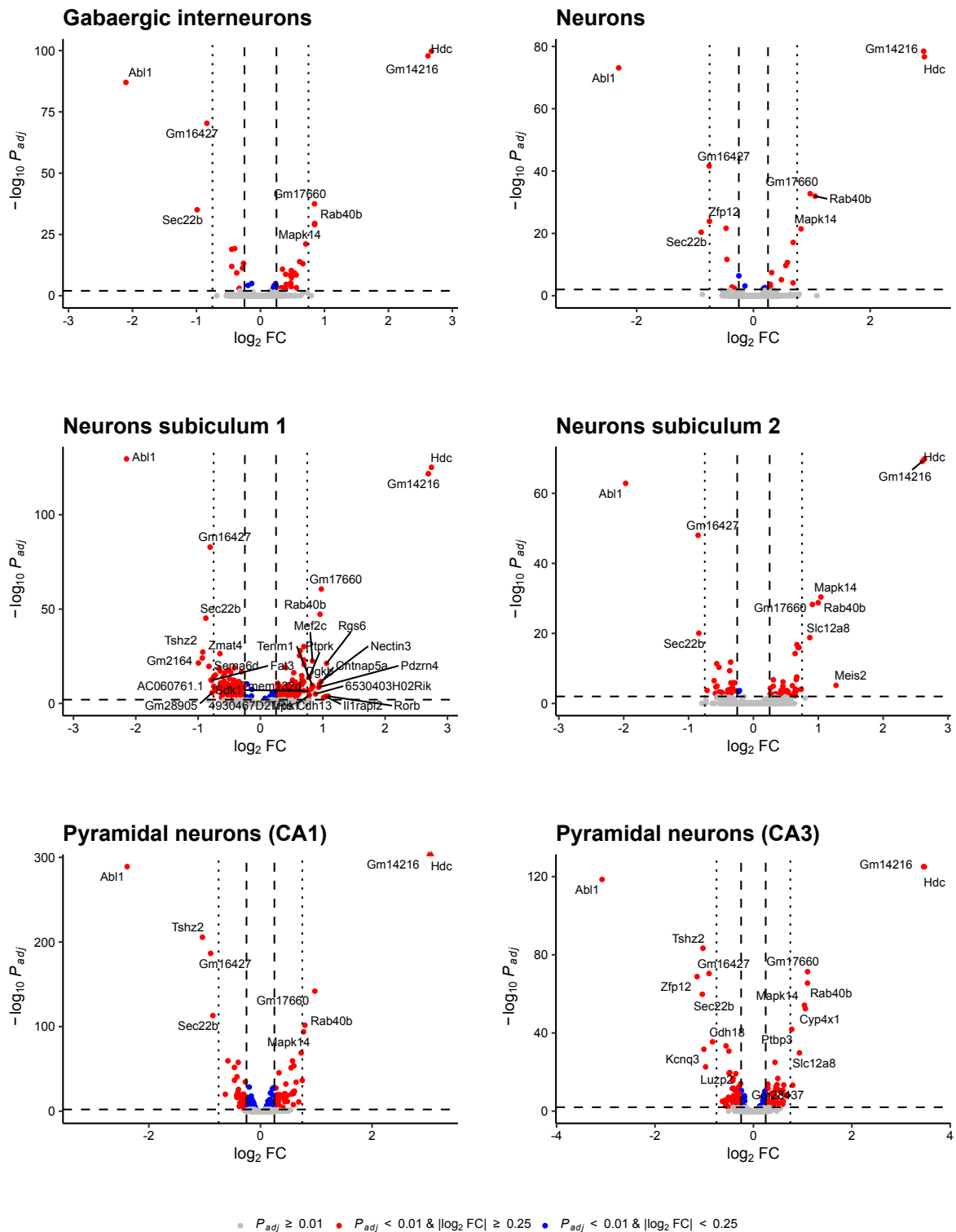


Volcano plots resulting from comparison of *Pigv*[341E] cells and wild-type cells within neuronal
cellular subgroups. Dashed horizontal lines are located at an adjusted p-value of 0.01, dashed vertical
lines at an absolute $\log_2$ fold change of 0.25 and dotted vertical lines at an absolute $\log_2$ fold change of
0.75. For genes with an adjusted p-value below 0.01 and a minimum absolute $\log_2$ fold change of 0.75,
gene symbols are depicted.

**Supplementary Figure 18**
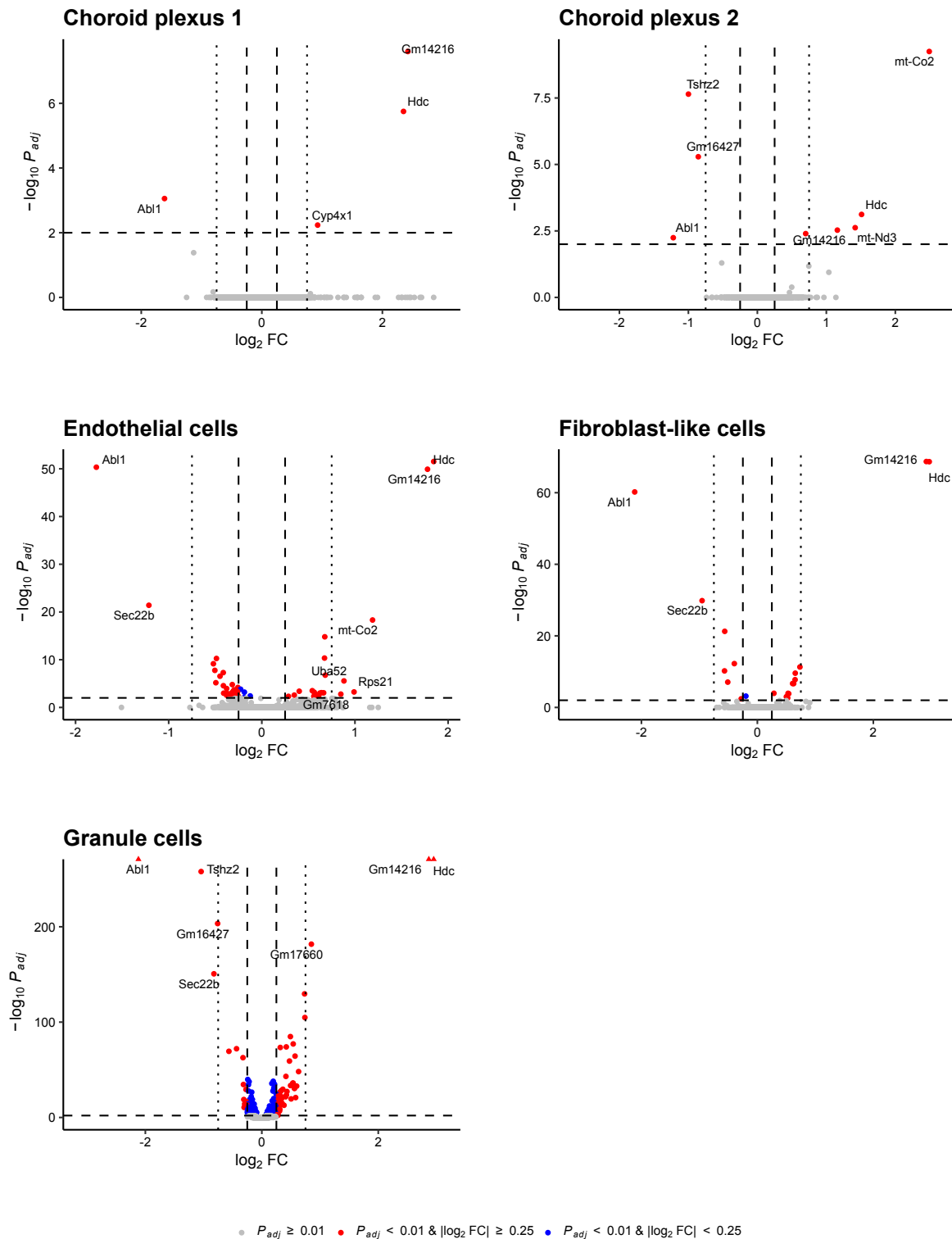


**Volcano plots resulting from comparison of *Pigv*[341E] cells and wild-type cells within other cellular subgroups.** Dashed horizontal lines are located at an adjusted p-value of 0.01, dashed vertical lines at an absolute $\log_2$ fold change of 0.25 and dotted vertical lines at an absolute $\log_2$ fold change of 0.75. For genes with an adjusted p-value below 0.01 and a minimum absolute $\log_2$ fold change of 0.75, gene symbols are depicted.

## Supplementary Material and Methods

**Flow cytometry of mouse embryonic fibroblasts and mouse embryonic stem cells**

Isolation of mouse embryonic fibroblasts (MEFs) from E13.5 embryos [Wt (n=4), het-*Pigv*[341E] (n=4), hom-*Pigv* (n=5)] is described elsewhere (McKean et al., 2012). MEFs were maintained in Dulbecco's modified eagle's medium (DMEM) supplemented with 10% fetal calf serum (FCS), 1% ultra-glutamine and 1% penicillin/streptomycin. mES cells were maintained as previously described (Franke et al., 2016) . For flow cytometry, cells were detached with cold ethylenediaminetetraacetic acid (EDTA) diluted in 1x phosphate buffered saline (PBS) and a cell scraper. Afterwards, cell suspension was pipetted several times to get a single cell suspension. Cells were stained with fluor-proaerolysin (FLAER) [Af-488] and Anti-mCD90/Thy1-PE (only used in mES cells) (R&D Systems, FAB7335P) in 1x PBS supplemented with 2% FCS for 30 min. Cells were then centrifuged at 400g for 5 min and washed in 1x PBS supplemented with 2% FCS two times. The stained cells were subsequently analyzed using the MACSQuant® VYB flow cytometer and the FlowJo[TM] v. 9.8.2 software. For mouse embryonic stem (mES) cells the average and standard deviation was calculated including two technical replicates.

References:

McKean DM, Niswander L. Defects in GPI biosynthesis perturb Cripto signaling during forebrain development in two new mouse models of holoprosencephaly. Biol Open. 2012;1(9):874–83.

Franke M, Ibrahim DM, Andrey G, Schwarzer W, Heinrich V, Schöpflin R, et al. Formation of new chromatin domains determines pathogenicity of genomic duplications. Nature [Internet]. 2016;538(7624):265–9. Available at: http://dx.doi.org/10.1038/nature19800

**CRISPR-Cas9 gene-editing in mouse embryonic stem cells**

mES cells were maintained as previously described (Franke et al. 2016). For knock-in of pathogenic mutations (e.g. Pigv c.1022C>A) in mES cells, single-stranded oligo-deoxynucleotides (ssODN) (60 pMol) were co-transfected with pX459 vector from Addgene containing the single-guided RNA (sgRNA) for e.g Pigv#1. Cloning of sgRNA in pX459 vector was performed according to Ran et al. (Ran et al., 2013). ssODNs were designed with

asymmetrical homology arms (HA) and with phosphorothioate (PS) bonds as previously described (Richardson et al., 2016, Renaud et al., 2016) (SI *Appendix*, Fig. S1C). Transfection of mES cells and further processing was performed as previously described (Kraft et al., 2015). Genotyping of the cells were conducted as already explained (see Material and Methods, section: animals). Positive knock-in clones were confirmed by Sanger sequencing and used for diploid or tetraploid aggregation (SI *Appendix*, Fig. S1A, Fig. S1D, top graph).

References:

Franke M, Ibrahim DM, Andrey G, Schwarzer W, Heinrich V, Schöpflin R, et al. Formation of new chromatin domains determines pathogenicity of genomic duplications. Nature. 2016;538(7624):265–9.

Ran FA, Hsu PD, Wright J, Agarwala V, Scott DA, Zhang F. Genome engineering using the CRISPR-Cas9 system. Nat Protoc. November 2013;8(11):2281–308.

Richardson CD, Ray GJ, DeWitt MA, Curie GL, Corn JE. Enhancing homology-directed genome editing by catalytically active and inactive CRISPR-Cas9 using asymmetric donor DNA. Nat Biotechnol. March 2016;34(3):339–44.

Renaud J-B, Boix C, Charpentier M, De Cian A, Cochennec J, Duvernois-Berthet E, et al. Improved Genome Editing Efficiency and Flexibility Using Modified Oligonucleotides with TALEN and CRISPR-Cas9 Nucleases. Cell Rep. March 2016;14(9):2263–72

Kraft K, Geuer S, Will AJ, Chan WL, Paliou C, Borschiwer M, et al. Deletions, inversions, duplications: Engineering of structural variants using CRISPR/Cas in mice. Cell Rep. 2015;10(5):833–9.

**Behavior testing**

Mice were habituated to the room adjacent to the testing room 30 min before starting behavior experiments. The equipment was cleaned with 70% ethanol before the experiments. In between animals and trials, the equipment was cleaned with 5% ethanol. Behavior experiments were conducted during the light phase (approx. 4 hours after the dark cycle ended). For the motor tests (rope grip, grip strength, beam walking, rotarod, foot print) nest construction test, home cage scan (HCS, CleverSys) recording and the social activity monitor (SAM, PhenoSys) (first approach) one cohort, Wt (female n=8, male n=4) $Pigv^{341E}$ (female n= 4, male n=2), was phenotyped at two consecutive time points (motor and nest construction

test: 7 and 15 weeks, HCS: 8 and 16 weeks, SAM: 9 and 17 weeks). For cognitive tests (Barnes maze, y-maze), affective tests (open field, dark-light-box, elevated plus maze), social tests (three-chamber, social proximity), the marble burying tests and the buried food test two cohorts of the same age were used [first cohort: Wt (female n=4, male n=5) $Pigv^{341E}$ (female n=2, male n=2), second cohort: Wt (female n=5 male n=6) $Pigv^{341E}$ (female n= 2, male n=5)]. For the SAM (second approach) only the second cohort was used. The behavioral experiments were conducted in the same order in both cohorts. For the hindlimb clasping test a separate cohort was used [age: 6 weeks, Wt (female n=3, male n=5), het-$Pigv^{341E}$ (female n=4, male n=4), hom-$Pigv^{341E}$ (female n=4, male= n=6)].

**Hindlimb clasping test**

For each trial, mice were gently griped by the tale close to the body and held for 10 sec (3 trials in total). After each trial there was an (inter-trial interval) ITI of 5 min. During tail suspension, hindlimb clasping behavior was manually evaluated with following criterias: 0 - hindlimb were spread widely. 1 – one hindlimb pointed inwards for more than 50% of the time. 2 - both hindlimbs pointed inwards for more than 50% of the time in a repetitive manner. 3 - both hindlimbs were permanently pointing inwards for more than 50% of the time

**Rope grip test**

A 40 cm rope was tautly attached to a blue crate (40 x 30 x 26 cm). The blue crate was supplemented with padding on the bottom. Mice were gently griped by the tail close to the body and were allowed to grab the rope in the middle with both forepaws. Mice were then released and the time to reach one of the ends of the rope as well as the time to fall off the rope was measured. Mice were allowed to hang a maximum of 60 sec. The motoric behaviors were scored as followed: Score 0-Animal felt off. Score 1-Animal hang onto the string by one or both forepaws. Score 2-Animal hang onto the string by one or both forepaws and attempted to climb onto the string. Score 3-Animal hang onto the string by one or both forepaws plus one or both hindpaws. Score 4-Hang onto the string by forepaws and hindpaws plus tail was wrapped around string. Score-5-Animal escaped to the supports. Raw data acquisition was done manually by the experimenter.

## Grip strength test

Each mouse was weighed before the test. Mice were gently griped by the tail close to the body and were gently lowered over the top of the bar that was connected to the TSE Grip Strength Meter apparatus. As soon as the mice attached the bar with both fore paws they were gently pulled away until they released the bar. Grip strength of only the forelimbs were recorded automatically and transferred to the computer by a (TSE) Grip Strength Meter. For each animal and type of measure, three values [g] were taken and averaged. Each animal of a batch was tested consecutively in the same order the grip strength mean value in [g] that was then normalized to the weight of the mice.

## Beam walking test

Wooden beams (100 cm) were placed horizontally, 50 cm above the bench surface, with one end mounted on a narrow support and the other end attached to an enclosed box into which the mouse could escape. The ground under the beam was supplemented with padding. Mice were put on the bright lit start position and trained for two days to traverse a 20-mm diameter beam and enter an escape box on the other side of the beam. For training, 4 trials per animal were performed. On the test day, mice had to traverse the beam in two consecutive trials on each beam (20 mm, 15 mm, 10 mm) progressing from the widest to the narrowest beam. Mice were allowed up to 60 sec to traverse each beam. The time that mice needed to traverse the beam and to enter the escape box was measured. In addition, the number of hind foot slips were count. Raw data acquisition was done manually by the experimenter.

## Rotarod test

Mice were put in the TSE Systems Rotarod apparatus. This apparatus 3 cm diameter rod that had ~1 mm horizontal grooves on the surface, which are designed to provide the mouse with better grip whilst running the task. The rod length was 30 cm, sub-divided with four partitions to create separate compartments such that five mice could be run simultaneously. Each mouse completed 3 trials with an ITI of 15 minutes. After the start of the test the rotarod accelerated then from 4-40 rpm for 300 sec. The latency to fall of the rotarod was measured by the TSE Rotarod software.

## Foot print test

For this test mice were held in a scruffed position in order to apply color paints to their feet (red-forelimbs, blue-hindlimbs) (Dr. Oetker, Food colors). After the color was applied, for both training and testing, mice traverse the horizontal lane (67 cm long, 5 cm wide) of a T-maze covered with a white sheet, for two consecutive trials each. After the test, different parameters on the sheet were measured: stride length-forelimbs/hindlimb (SL-FL, SL-HL) (distance for forward movement for hindlimb and forelimb), hind base/fore base width (HBF, FBW) (distance between left and right footprints for hindlimb and forelimb), S-(distance between hindlimb and forelimb or overlap between forepaw and hindpaw placement). Raw data acquisition was done manually by the experimenter.

## Nest Construction Test

Each Mouse was singly housed in a new home cage with fresh bedding that included a nestlet (5x5 cm pressed white cotton square). After 16 hours the nest built out of the cotton was scored manually with following criterias: Score 1-The nestlet was largely untouched (>90% intact). Score 2-The nestlet was partially torn up (50-90% remaining intact). Score 3-The nestlet was mostly shredded but often there was no identifiable nest site: < 50% of the nestlet remained intact but < 90% was within a quarter of the cage floor area, i.e. the cotton was not gathered into a nest but spread around the cage. Score 4- > 90% of the nestlet was torn up, the material was gathered into a nest within a quarter of the cage floor area, but the nest was flat with walls higher than mouse body height on less than 50% of its circumference. Score 5- > 90% of the nestlet was torn up, the nest was a crater, with walls higher than mouse body height on more than 50% of its circumference. Furthermore, the nestlet was weighed before the test and afterwards. The difference between both time points was calculated in [%].

## Home cage scan and computational analysis

Mice were put in a home cage separated from each other and monitored for 23h. For the quantification of natural animal behavior in the familiar environment of its home cage, we used the HCS video and analytic software (CleverSys) which detects automatically different behaviors of freely moving mouse in its home cage ($35 \times 20 \times 15$ cm). Nineteen different behavior patterns of the mice were detected during a 23 h period (11 h of light phase and 12 h

of dark phase/mouse). Number of occurrences and duration of each behavior were analyzed over time and on average per hour using custom-made R scripts.

**Social activity monitoring and computational analysis**

Mice were monitored for 14 days (first approach) with mixed genotypes in their home cage. For the second approach we monitored mice for 4 days with mixed and separated (non-mixed) genotypes. During this time the animal cages were placed on the SAM system (Phenosys. Germany). Each cage is placed on an ID-Grid sensor plate that detects the individual animals and tracks them as they move throughout the cage. Each ID-Grid sensor plate contains eight RFID sensors that records data on the location of the animals at every time point. The data is collected using Phenosoft Control software, preprocessed by Phenosoft analytics software and analyzed in R (R Core Team, 2017).

References:

R Core Team (2017). R: A language and environment for statistical computing. R Foundation for Statistical Computing, Vienna, Austria. URL https://www.R-project.org/.

**Barnes maze test**

During the training phase animals were given 4 trials a day for 4 days with an ITI of 15 minutes. For each trial the animals were placed on a table with a 92 cm diameter, containing 20 holes along the periphery in which one of the holes contained a nest that the animal could go into. The animal was allowed 3 minutes to find the nest. To encourage the animal to search for the nest a light white noise was played. Once the animal found the nest the white noise was stopped and the animal was allowed to stay in the nest for 1 minute. If the animal did not find the nest in the allotted 3 minutes it was shown the nest and the white noise was stopped. The animal was then allowed to stay in the nest for 1 minute. During the probe trials on day 5 and day 12 animals were returned to the table containing the 20 holes with the nest removed. During the probe trials the animal's behavior was observed for 90 s. For the evaluation of the search strategies 33.3% of the trials were analyzed for each animal. All parameters were recorded by the video-tracking system Viewer (Biobserve). Two animals had to be excluded from the analysis, since they were not able to learn the location of the exit hole during day 1-4.

**Buried food test**

For 3 consecutive days before testing, the mice were given sweet pellets (purified rodent tablets, 45 mg, TestDiet®, at least 3 times). All mice had to consume the pellets before the test or had to be excluded from the test. Four hours before testing, mice were deprived of food with water ad libitum. Before testing, each mouse was given 5 min of habituation in the testing cage (regular home cage; 35 × 20 × 15 cm) that contained 4 cm of fresh bedding. After this habituation, the mouse was temporarily removed from the testing cage, while a sweet pellet was hidden 1 cm deep and 5 cm away from the cage rear. For testing, the mouse was positioned in the center of the opposite end of the cage and the latency to find the food, i.e. the time from the moment the mouse was placed into the cage to the time it located the sweet pellet and initiated digging was recorded. Whether the pellet was eaten or not and other spontaneous behavior (rearing, climbing on the lid, grooming and extensive digging) were also scored. The mouse was then removed from the cage. A new cage and fresh bedding were used for each mouse. Raw data acquisition was done manually by the experimenter.

**Three-chamber Test**

The social testing arena was a rectangular, three-chamber box (60 x 40 x 22 cm, Stoelting apparatus) with white non transparent external walls. Each chamber was (20 x 40 x 22 cm) in size. Dividing walls were made from clear plexiglas, with rectangular openings (50 cm x 80 mm) allowing access into each chamber. The light condition was kept dim and uniform over the 3 chambers. In the experimental room, the test mouse was first placed in the middle chamber of the arena and allowed to explore for 10 min. To test sociability, after this habituation the mouse was trapped in the center chamber and an stranger mouse, that had no prior contact with the subject mouse, was placed in one of the side chambers. The location of the stranger mouse in the left vs. right side chamber was systematically alternated between testing animals. The stranger mouse was enclosed in a round wire cage with grey plexiglas covers (7 x 7 x 15 cm), which allowed nose contact through the bars but prevented fighting. The animals serving as stranger mice had previously been habituated to the small cage (at least 3 times before test, 5 min each time). An identical empty wire cage was placed in the opposite chamber. Both openings to the side chambers were then unblocked and the test mouse was allowed to explore the entire social arena for a 10 min session. The amount of time spent in each chamber and in close proximity to the grid were recorded by the video-tracking system Viewer (Biobserve). Number of sniffs at the wire cage was recorded

manually as an index of close investigation. At the end of the first 10 min, each mouse was tested in a second 10 min session to quantify social recognition for a new stranger mouse after an ITI of 5 min (similar condition as the habituation phase). A second stranger mouse was placed into the previously empty wire cage. The testing mouse had a choice between the first, already-investigated mouse (familiar mouse=stranger 1), and the novel stranger mouse (stranger 2). As described above, measures were taken of the amount of time spent in each chamber and in close proximity with the grid during the second 10 min session. The position of stranger 1 and 2 was for each mouse changed in order to avoid side bias. Stranger mice had the same age and sex as the testing animal. One animal was excluded from the analysis since during habituation it only explored one side (chamber) of the maze.

**Y-maze**

Mice were placed in a y-maze that had 3 identical arms (34 x 6 x 17 cm), placed at 120° from each. The animals were placed facing the end of one arm of the maze. The starting arm was alternated between mice. Mice were allowed to explore the y-maze for 5 minutes. The percentage of spontaneous alternation (SAP), same arm returns (SAR), and alternate arm returns (AAR) as well as the distance traveled and time spent in each arm were recorded and measured using the video-tracking system Viewer (Biobserve).

**Marble burying test**

In a mouse cage (35 × 20 × 15 cm) twenty clean and identical glass marbles (green) were placed equally spaced in five rows of four marbles on a 4 cm layer bedding. For each animal a different cage with fresh bedding was used but illumination was kept homogeneous. The animal was placed in the testing cage close to a wall and allowed to explore the cage for 30 min. The latency for the first marble to be buried was manually scored. At the end of the test the mouse was rapidly removed from the cage and the total number of marbles buried was counted manually. A marble was considered "buried" when two thirds of its volume was covered by bedding. The marbles were cleaned with 5 % alcohol and dried for approximately 10 min before being used again.

**Social proximity test**

Mice were put in a transparent testing cage (size: 4x17 cm, 98cm$^2$) together with a stranger mouse with same age and sex. The behavior of the mice were recorded for 20 minutes. The video was manually evaluated after all experiments were finished. Number of different social traits were count: nose tip-to-nose-tip contact: The scored animal nose-tip and/or vibrissae contact with the nose-tip and/or vibrissae of the other animal. Nose-to-head contact: The scored animal nose-tip and/or vibrissae contact the dorsal, lateral, or ventral surface of the other animals head. Nose-to-anogenital contact: The scored animal nose-tip or vibrissae contact with the base of the tail and/or anus of the other animal. Crawl over: The scored animal forelimbs cross the midline of the dorsal surface of the other animal. Crawl under: The scored animal head goes under the ventral surface of the other animal. Rear up: Mice stretch their body vertically towards the cage. jump escape: the scored animal makes a vertical jump with all four feet leaving the ground.

**Dark/light Box**

Within the TSE multi-conditioning system mice were placed in the light chamber of a two compartment box that consisted of a light chamber and a dark chamber (30 x 22 cm for each chamber). Mice were then allowed to explore both chambers for a total of 10 minutes. The time that mice explored each the light and dark chambers was measured and recorded by the TSE software.

**Elevated Plus Maze**

The mice were placed into a white PVC (50x50x53) elevated plus maze with two open arms and two closed arms and allowed to explore for 5 minutes.). The total distance, average velocity and the number of visits to each arm were recorded using the Viewer software (Biobserve).

**Open field test**

Mice were allowed to explore to the open field (50 x 50 cm) for 10 min. The time spent in the center and the periphery was recorded and measured by the Viewer software (Biobserve).

## Preparation of paraffin-embedded sections

Animals were deeply anesthetized with Ketamin/Rompun and subsequently transcardially perfused with 20 ml 1x DPBS and with 20 ml paraformaldehyde (PFA) (4%) in 1x PBS with a 23G needle. The brain was removed and fixated in 4% PFA at room temperature over night. Thereafter, the brain was washed in 1x PBS twice for 30 min and finally in 50% and 70% Ethanol at room temperature for 30 min in each solution. The brain was stored in 70% ethanol at 4°C or further processed. Paraffin infiltration was performed with the tissue processor (Leica). Afterwards, paraffin-infiltrated brains were embedded in paraffin and sectioned (coronal) with a thickness of 5 microns using the paraffin microtome (Leica). Paraffin-embedded sections were deparaffinized in Xylene twice for 5 min. Afterwards, sections were rehydrated by washing them in 100% (twice), 90%, 70%, and 50% Ethanol for 5 min in each solution. Sections were then immediately processed for Nissl staining or synaptophysin-staining.

## Synaptophysin-staining

Paraffin-embedded sections were rehydrated as described and then washed twice in 1× PBS for 3 min. Afterwards, antigen retrieval of sections was performed in 10 mM citrate buffer for 5 min at 60 °C, and the sections were washed twice in 1× PBS for 3 min. Sections were permeabilized and blocked for 30 min at room temperature in 0.2% Triton X-100 and 3% bovine serum albumin (BSA). Sections were washed twice for 3 min in 1× PBS and stained overnight at 4°C with anti-synaptophysin antibody (1:800, Abcam, ab32127), diluted in 1× PBS supplemented with 3% BSA. Afterwards, sections were washed for 1 h in 1× PBS, and secondary antibody (anti-rabbit-488Af, 1:1000) was applied in 1× PBS supplemented with 3% BSA. Sections were washed with 1× PBS for 3 min and stained with 4′,6-diamidino-2-phenylindole (DAPI) (1:1000) for 10 min. Finally, sections were washed three times for 3 min and embedded in Fluoromount.

For each biological replicate [Wt(female n=3, male n=2) Pigv341E(female n=2, male n=4), age: P23-25], three sections were analyzed. Three images were taken for each section per area [*Cornu Ammonis* 1 − *Stratum Radiatum* (CA1–SR), *Cornu Ammonis* 3 − *Stratum Radiatum* CA3–SR, *Cornu Ammonis* 1 − molecular layer of dentate gyrus (CA1–ML)] at 63× magnification on a ZEISS LSM 700 confocal microscope. 6 Z-stacks were recorded and

transformed to one image with the ZEISS Zen Blue Software. Images were analyzed with FIJI ImageJ for quantification of synaptophysin immunoreactivity/$\mu m2$.

## Nissl staining

Paraffin-embedded sections were deparaffinized and rehydrated as described above. Sections were then washed twice in ddH$_2$O for 5 min. Afterwards, sections were maintained in Cresyl Violet buffered in Acetate Buffer (Nissl-staining solution) (pH 3,8-4) for 10 min. After Nissl-staining sections were washed twice for 3 sec in 100% Ethanol. Finally, the sections were embedded in Entellan. Images of sections were taken at 4x magnification.

## Acute slice preparation

Acute hippocampal brain slices were prepared as described by Stempel et al. 2016. Adult mice were sacrificed by cervical dislocation. The brain was quickly removed and chilled in ice-cold sucrose - based artificial cerebrospinal fluid (sACSF) containing (in mM): NaCl 87, NaHCO3 26, sucrose 50, glucose 10, KCl 2.5, NaH2PO4 1.25, MgCl2 3, CaCl2 0.5, continuously oxygenated. Horizontal slices (300 $\mu m$) were cut and stored submerged in sACSF for 30 min at 35 °C and subsequently stored in ACSF containing (in mM): NaCl 119, NaHCO3 26, glucose 10, KCl 2.5, NaH2PO4 1, CaCl2 2.5 and MgCl2 1.3 saturated with 95% (vol/vol) O2/5% (vol/vol) CO2, pH 7.4, at room temperature. Experiments were started 1 to 6 h after the preparation.

References:

Stempel AV, Stumpf A, Zhang HY, Özdoğan T, Pannasch U, Theis AK, et al. Cannabinoid Type 2 Receptors Mediate a Cell Type-Specific Plasticity in the Hippocampus. Neuron. 2016;90(4):795–809

## Schaffer collateral recordings

Acute hippocampal brain slices were prepared as described above. Recordings were performed at room temperature (22–24°C) in a submerged recording chamber (Warner Instruments, RC-27L) ACSF, with solution exchange speed set to 2.5 ml/min. Low-resistance stimulation electrodes were placed in CA3–SR to stimulate Schaffer collaterals, and the

recording electrode was placed in the CA1–SR field. Basal stimulation was applied every 10 sec. To analyze the input–output relationship, stimulation intensities were adjusted to different fiber volley (FV) amplitudes (0.05 mV increments) and correlated with the corresponding field excitatory post-synaptic potential (fEPSP) amplitudes. Paired pulse ratios (PPRs) were determined by dividing the amplitude of the second fEPSP (50 ms inter-stimulus interval) by the amplitude of the first (average of ten repetitions). Four high-frequency trains (100 pulses, 100 Hz) were applied every 10 sec, and the amplitude of the following fEPSP was normalized to the baseline [post-tetanic potentiation (PTP)]. Several measurements were conducted for each animal. The mean was calculated from all measurements from all animals [Wt(female n=2, male n=2) Pigv341E(female n=2, male n=2)].

**Pentylenetetrazol (PTZ) kindling model.**

Convulsive seizures were induced by repetitive intraperitoneal injections of PTZ every 10 min as described before (Van Loo et al., 2019) in Wt (female n=3, male n=9) and $Pigv^{341E}$ mice (female n=5, male n=6). Each injection consisted of 10 mg/kg PTZ (Sigma-Aldrich) and was given until a convulsive seizure occurred. The total dose of PTZ per animal did not exceed 100 mg/kg.

References:

Van Loo KMJ, Rummel CK, Pitsch J, Müller JA, Bikbaev AF, Martinez-Chavez E, et al. Calcium channel subunit α2σ4 is regulated by early growth response 1 and facilitates epileptogenesis. J Neurosci. 2019;39(17):3175–87.

**Isolation of hippocampal cells**

The animals were deeply anesthetized with Ketamin/Rompun and transcardially perfused with 20 ml 1x DPBS (pH 7,4) via a 20 ml syringe and a 23 G needle. The brains were removed and the hippocampi (2 hippocampi, each animal) were surgically taken out.
All procedures conducted for hippocampal cell isolation were performed on ice or at 4°C and all solutions were pre-cooled to 4°C. We pooled in total 8 hippocampi of 4 male animals per genotype (Wt and $Pigv^{341E}$). Hippocampi were dissociated in 1,5 ml Hibernate A (BrainBits) with a Dounce homogenizer (Active Motif) using the loose mortal. Single-cell suspension was

transferred through a 70 μm strainer into a falcon. Afterwards, the Dounce homogenizer was washed twice with 1 ml Hibernate A. Remaining cells were collected from the washing step, passed through the 70 μm strainer and transferred into the falcon. Single-cell suspension was centrifuged at 500g for 10 min. Thereafter, pellet was resuspended in 1,55 ml DPBS (pH 7,4). Afterwards, 450 μl isotonic Percoll (10x DPBS diluted 1:10 in Percoll, pH 7,4) was added and single-cell suspension was pipetted up and down. 2 ml of 1x DPBS was very gently transferred on the single-cell suspension. The layered solution was then centrifuged for 10 min at 3250g. The supernatant with the myelin disk was removed immediately and the remaining pellet was washed in 4 ml 1x DPBS (pH 7,4) and centrifuged for 10 min at 400g. Finally, the pellet was resuspended in 1x DPBS (pH 7.4) and the volume was adjusted to get a final concentration of 10000 cells per 10 μl. Single-cell suspension was then further processed for single-cell RNA sequencing-library preparation.

**Single-cell RNA sequencing, preprocessing, and analysis**

Sequencing libraries were generated using the Chromium Single-cell Gene Expression Solution v3 (10X Genomics, Inc.) and sequenced on an Illumina NovaSeq 6000. Both pooled $Pigv^{341E}$ and wild-type samples were sequenced on the same lane. Demultiplexed sequencing data were provided by the core facility. Quality assurance of raw sequencing reads was performed with FastQC. For alignment to reference genome GRCm38.96 and quantification of single-cell gene expression, the zUMI pipeline with internal usage of the STAR aligner was employed. Both exonic and intronic reads were considered for downstream analysis.

Further processing and analysis of the generated gene expression count table were conducted in R, mainly using the single-cell genomics toolkit Seurat. Based on the distribution of cells, 19 out of 15,949 cells with ≤ 100 genes, ≤ 100 unique molecular identifiers (UMIs), or ≥ 30% of UMIs mapping to mitochondrial genes were removed by filtering (SI *Appendix*, Fig. S12). Gene expression values of the remaining 8,836 Pigv341E mutant cells and 7,094 wild-type cells were normalized using the "sctransform" procedure developed by Hafemeister and Satija (2019), including the percentage of UMIs mapping to mitochondrial genes as a regression variable (Hafemeister and Satija, 2019). After principal component analysis (PCA), the first 11 principal components were selected for dimensionality reduction based on the amount of captured variance (SI *Appendix*, Fig. S13). These components were used as input for clustering of cells, as well as for two-dimensional visualization with UMAP. For cluster definitions, we employed the unsupervised graph-based approach implemented in Seurat with

k = 10 nearest neighbors. The resolution parameter was set to 0.2 based on visual concordance with the 2D representation in UMAP space. We then assigned cellular identities by analyzing the genes differentially expressed between the clusters. Candidate genes were compared with the adult mouse brain atlas (http://dropviz.org/) and in situ hybridization data from the Allen brain atlas (https://mouse.brain-map.org/search/index) (Saunders et al., 2018) (SI *Appendix*, Fig. S15). Distributions of cells across defined cellular subgroups were compared between genotypes by Pearson's Chi-squared test. For differential expression testing between groups of cells, the default settings in Seurat were used. Genes with an absolute average log2(fold change) $\geq$ 0.25 and Bonferroni-adjusted p value $\leq$ 0.01 were considered significantly differentially expressed. Genes with significant differential expression between groups of interest were examined for overrepresentation of gene ontology (GO) terms relative to the background of all genes expressed in our data set using the clusterProfiler package; terms with an FDR adjusted p-value < 0.05 were considered significantly enriched.

References:

Hafemeister C, Satija R. Normalization and variance stabilization of single-cell RNA-seq data using regularized negative binomial regression. Genome Biol. 2019;20(1):1–15.

Saunders A, Macosko EZ, Wysoker A, Goldman M, Krienen FM, de Rivera H, et al. Molecular Diversity and Specializations among the Cells of the Adult Mouse Brain. Cell [Internet].2018;174(4):1015-1030.e16.Available at: https://doi.org/10.1016/j.cell.2018.07.028

**Dataset S1. Statistical Analysis**

The dataset includes the statistical tests, which were used for each experiment, the corresponding p-values, and effect size.

**Dataset S2. Gene ontology (GO) analysis – 1, single-cell RNA sequencing**

Gene ontology analysis of differentially expressed genes between each cellular subgroup and all remaining cellular subgroups.

**Dataset S3.  Gene Ontology (GO) analysis – 2, single-cell RNA sequencing**

Gene ontology analysis of differentially expressed genes between all cellular subgroups by genotype, and between each cellular subgroup by genotype.

**Dataset S4.  Differentially expressed genes -1, single-cell RNA sequencing**

Differentially expressed genes between each cellular subgroup and all remaining cellular subgroups.

**Dataset S5.  Differentially expressed genes -2, single-cell RNA sequencing**

Differentially expressed genes between all cellular subgroups by genotype, and between each cellular subgroup by genotype.

**Dataset S6. Motor behavior tests**

Includes the raw data from the rotarod performance, beam walk, rope grip, grip strength, and foot print test.

**Dataset S7. Social behavior tests**

Includes the raw data from the three-chamber test (sociability, social recognition, habituation phase) and social proximity test.

**Dataset S8. Barnes maze test**

Includes the raw data from the Barnes maze test: latency to escape, path length, # wrong holes, target area, search strategy.

**Dataset S9. Cognitive and species-specific behavior tests**

Includes the raw data from the y maze, nest construction, marble burying, and buried food test.

**Dataset S10. FACS, weight curve, hindlimb test**

Includes the raw data from the main figure 1.

**Dataset S11. Synaptophysin-immunoreactivity**

Includes the raw data from the synaptophysin immuno-fluorescence staining (Figure 5A).

**Dataset S12. Electrophysiology and PTZ experiments**

Includes the raw data from the electrophysiology (Figure 5B-D) and from the PTZ experiments (Figure 5E).

**Dataset S13. Social activity monitor – first approach**

Includes the raw data from the first approach of the social activity monitor with two different time points.

**Dataset S14. Social activity monitor – second approach**

Includes the raw data from the second approach of the social activity monitor, in which animals were housed in groups with mixed genotypes and separated from each other with respect to their genotype (non-mixed).

**Dataset S15. Home cage scan**

Includes the raw data from the home cage scan: Total occurrences of behavior, total duration of behavior, and mean duration per hour of behavior.

**Dataset S16. Affective behavior**

Includes the raw data from the elevated plus maze, dark-light box, and open field test.

## 12.) Curriculum Vitae

My curriculum vitae does not appear in the electronic version of my dissertation for reasons of data protection.

My curriculum vitae does not appear in the electronic version of my dissertation for reasons of data protection.

# 13.) Publication List

**de los Santos MR**, Rivalan M, David FS, Stumpf A, Pitsch J, Tsortouktzidis D, Moreno Velasquez L, Voigt A, Schilling K, Mattei D, Long M, Vogt G, Knaus A, Fischer-Zirnsak B, Wittler L, Timmermann B, Robinson PN, Horn D, Mundlos S, Kornak U, Becker AJ, Schmitz D, Winter Y, Krawitz PM. A CRISPR-Cas9 – engineered mouse model for GPI-anchor deficiency mirrors human phenotypes and exhibits hippocampal synaptic dysfunctions. Proc Natl Acad Sci U S A. 2021;118(2).

Holtgrewe M, Knaus A, Hildebrand G, Pantel JT, **de los Santos MR**, Neveling K, Goldmann J, Schubach M, Jäger M, Coutelier M, Mundlos S, Beule D, Sperling K, Krawitz PM. Multisite de novo mutations in human offspring after paternal exposure to ionizing radiation. Sci Rep. 2018;8(1):1–5.

# 14.) Acknowledgement / Danksagung

meinem Onkel Fernando, meinen Nichten Laura und Daniela, meinen Neffen Alberto und Fernando und vielen mehr. Ihr seid zwar weit weg aber trotzdem habt auch ihr einen wichtigen Teil dieser Arbeit ausgemacht.

Auch bin ich zu großem Dank meiner Berliner-Stuttgarter Familie verpflichtet: Khaled, Danilo, Michael und Saša, ich danke euch dafür, dass ihr immer für mich da gewesen seid und für die tolle Zeit in Berlin und in Stuttgart während des PhDs, die mir immer wieder Kraft gegeben hat mit Motivation und Enthusiasmus weiterzumachen.

Also, a big thanks goes to Ilaria Caserta and Daniele Mattei. I wish we could meet more often, but the times we meet it feels like our unforgettable gatherings, when we were living together in Berlin. Your friendship was a huge support for this work.